UNIVERSIDADE FEDERAL DO AMAZONAS
PRÓ-REITORIA DE PESQUISA E PÓS-GRADUAÇÃO
PROGRAMA DE PÓS-GRADUAÇÃO EM FÍSICA

HENRIQUE PECINATTO

Determination of the mechanical, thermal, transport, magnetic, electronic, and optoelectronic properties of AMoO$_4$ (A = Ca, Sr, Ba, Pb), with and without oxygen vacancy, by *ab initio* calculations

Support:

Manaus - AM
2023

HENRIQUE PECINATTO

Determination of the mechanical, thermal, transport, magnetic, electronic, and optoelectronic properties of AMoO$_4$ (A = Ca, Sr, Ba, Pb), with and without oxygen vacancy, by *ab initio* calculations

Thesis presented to the Graduate Program in Physics at the Federal University of Amazonas as partial fulfillment of the requirements to obtain the title of Doctor in Physics

Area of concentration: Condensed Matter Physics

Advisor: Hidembergue Ordozgoith da Frota

Manaus - AM
2023

Ficha Catalográfica

Ficha catalográfica elaborada automaticamente de acordo com os dados fornecidos pelo(a) autor(a).

ACKNOWLEDGMENTS

ABSTRACT

Molybdates of the form $AMoO_4$ (A = Ca, Sr, Ba, Pb) are widely studied materials due to their photo-luminescence properties. In the present doctoral thesis, we analyze the effect of oxygen vacancies through density functional density (DFT) in these scheelite-type materials, aiming primarily at the possible ferromagnetism induced due to this kind of defect. The spin-polarized band structure spectrum shows the appearance of narrow bands within the band gap for the spin-up channel. In $BaMoO_4$-$V_O^\times$, $SrMoO_4$-$V_O^\times$, and $PbMoO_4$-$V_O^\times$ a resultant magnetic moment of $2\mu_B$ per cell is observed due to, the electrons once bonded with O being trapped by the $4d$ states in trigonal cluster MoO_3, while in $CaMoO_4$-$V_O^\times$, the oxygen vacancy distort the lattice, so that crystal field splitting results in a low spin case with the resultant magnetic moment of $0.15\mu_B$ per cell. This study also provides a valuable tool for lowering the band gap in these materials, since the wide band gap has been recognized as a challenging factor for infrared and visible light photocatalysis performance. We calculated the mechanical properties from elastic constants such as bulk, shear, and Young modulus. In addition, Vicker's hardness indicates that oxygen vacancy increases the hardness of these materials. For thermoelectric properties, the electrical conductivity is addressed to the n-type carrier and, allied with the low thermal conductivity (lattice + electronic) provided by phonon scattering, results in a high figure of merit for all defective scheelites.

Keywords: **Molybdates. Oxygen vacancy. Ferromagnetism. Thermoelectric effect. First-principles calculations**

Resumo

Molibdatos da forma $AMoO_4$ (A = Ca, Sr, Ba, Pb) são materiais amplamente estudados devido a suas propriedades de fotoluminescência. Na presente tese de doutorado, pretendemos analisar o efeito de vacâncias de oxigênio através da teoria do funcional densidade (DFT) nestes materiais do tipo scheelita, visando principalmente o possível ferromagnetismo induzido devido a este tipo de defeito. O espectro da estrutura de bandas spin-polarizada mostra o aparecimento de bandas estreitas dentro do gap do material para o canal spin-up. Foi observado no $BaMoO_4$-$V_O^{\times}$, $SrMoO_4$-$V_O^{\times}$, e $PbMoO_4$-$V_O^{\times}$ um momento magnético resultante de $2\mu_B$ por célula, devido aos elétrons uma vez ligados ao O sendo presos pelos estados $4d$ no aglomerado trigonal MoO_3, enquanto no $CaMoO_4$-$V_O^{\times}$, a vacância de oxigênio distorce a rede, de modo que o desdobramento do campo cristalino resulta em um caso de baixo spin com o campo magnético resultante de momento magnético igual a $0,15\mu_B$ por célula. Este estudo também fornece uma ferramenta valiosa para diminuir o gap de energia nestes materiais, uma vez que o gap largo tem sido reconhecido como um fator desafiador para o desempenho de fotocatálise em luz infravermelha e visível. Calculamos as propriedades mecânicas, tais como o módulo de bulk, de cisalhamento e de Young, por meio das constantes elásticas. Além disso, a dureza de Vicker indica que a vacância de oxigênio aumenta a dureza desses materiais. Para as propriedades termoelétricas, a condutividade elétrica é endereçada ao portador do tipo n e, aliada a baixa condutividade térmica (rede + eletrônica) fornecida pelo espalhamento de fônons, resulta em um valor alto da figura de mérito para todas as scheelitas defeituosas.

Keywords: **Molibdatos. Vacância de oxigênio. Ferromagnetismo. Efeito Termoelétrico. Cálculos de primeiro princípios**

LIST OF FIGURES

LIST OF ABREVIATIONS AND ACRONYMS

DFT   Density Functional Theory

CFT   Crystal Field Theory

CF   Crystal Field

MO   Molecular Theory

VBT   Valence Bond Theory

QE   Quantum-Espresso

LDA   Local Density Approximation

GGA   Gradient-Generalized Approximation

PBE   Perdew-Burke-Ernzerhof

PAW   Projector Augmented-Wave

CIF   Crystallographic Information File

BFGS   Broyden-Fletcher-Goldfarb-Shanno

DFPT   Density Function Perturbation Theory

BZ   Brillouin zone

VRH   Voigt-Reuss-Hill

SCF   Self-Consistent Functions

PDOS   Projected Density of State

TE Thermoelectric

PF Power Factor

ZT Figure of Merit

CONTENTS

INTRODUCTION

The materials belonging to the Scheelite family, which possess a crystallographic system in space group I4$_{1/a}$ (n°88), have attracted significant scientific and technological interest due to their well-established optical properties [1–4]. Among these materials, molybdates of the form $AMoO_4$ (A = Ca, Sr, Ba, Pb) have found extensive applications in solid-state scintillators, lasers, optical devices, cryogenic detectors, and luminescent devices, primarily due to their high photoluminescent emission in the visible spectra regions [5–12]. Additionally, these materials are known for their suitability in microwave devices due to their small dielectric constant and low dielectric loss [13, 14]. Recent research has shown promising results in utilizing alkali earth metal scheelite-type compounds for photocatalytic performance in phenol for water treatment [15]. However, limitations in the wide band gap of these materials have hindered their application for ultraviolet radiation and fast recombination of photogenerated electron-hole pairs, thereby reducing their efficiency [16]. To address this, alternative methods such as doping and introducing point defects like oxygen vacancies have been explored to tune the band gap and enhance photocatalytic activity [17]. Notably, visible light photocatalysis for hydrogen production via water splitting has shown reasonable efficiency, low cost, and environmental friendliness [18].

Engineering defects in materials offer a way to enhance or generate new properties. Doped and host scheelite compounds have demonstrated novel properties, including high discoloration ratio of methylene blue, photodegradation of organic pollutants, weather sensing, UV-Visible energy conversion, white lighting diodes, photovoltaic cells, and solid oxide fuel cells [19–26]. The introduction of oxygen vacancies in the monoclinic phase of $BiVO_4$ significantly improves its photocatalytic properties by reducing the band gap [27]. Oxygen vacancy-induced magnetism has also been observed in Cr-doped $SrMoO_4$ [28]. First-principle calculations have supported the presence of magnetism resulting from a small oxygen vacancy concentration in $SrMoO_4$ [29]. Ferromagnetism has been reported in scheelites, such as $BaMoO_4$, attributed to induced oxygen vacancies during the synthesis process [30]. Consequently, a detailed analysis is needed to understand the mechanisms that induce magnetism in scheelite-type compounds and explore their potential technological applications. Despite the increasing interest in oxygen vacancies, the number of papers on this subject, particularly among molybdates in the scheelite phase, remains relatively low. Therefore, further theoretical and experimental stud-

ies are necessary to comprehend the mechanisms leading to ferromagnetism in non-magnetic oxides.

Regarding thermoelectric materials, the figure of merit $ZT = S^2 \sigma T / (\kappa_l + \kappa_e)$ is commonly used to measure the efficiency of thermoelectric compounds, where S represents the Seebeck coefficient, σ is the electrical conductivity, T denotes the absolute temperature, and κ_l (κ_e) represents the lattice (electronic) thermal conductivity. Thus, materials with low thermal conductivity can enhance the figure of merit. Cation-deficient scheelite materials, such as $La_2Mo_3O_{12}$, have shown ultra-low thermal conductivities ranging from 0.59-0.62 $Wm^{-1}K^{-1}$ [31]. Liu *et al.* [32] conducted extensive calculations using density functional theory to identify promising materials with ultra-low thermal conductivity, including $BaMoO_4$. It has been suggested that oxygen vacancies can reduce thermal conductivity [33]. However, there is currently no reported research on the thermoelectric properties of scheelite-type materials due to the presence of oxygen vacancies. Therefore, studies in this area could lead to the development of novel thermoelectric materials.

In summary, this work aims to investigate the influence of a single oxygen vacancy in $BaMoO_4$, $SrMoO_4$, $CaMoO_4$, and $PbMoO_4$ through first-principle calculations to fully characterize these defective compounds. The analysis will encompass the band structure, magnetism, density of states, charge density, optical properties, elastic constants, mechanical properties, thermal properties, and thermoelectric properties to uncover their significance in various technological applications.

This thesis consists of seven chapters. Chapter 2 provides a review of group theory, crystallography, and molecular orbital theory, as these concepts are fundamental to understanding the physical properties dependent on crystallographic symmetry. Chapter 3 covers the theoretical background of the software used and the calculated properties. Chapter 4 presents the workflow of the study and the obtained crystallographic data from atomic optimization. Chapter 5 focuses on the electronic and optical properties. Chapter 6 examines the elastic constants, mechanical properties, and thermoelectric properties of oxygen vacancy scheelite-type materials. Finally, Chapter 7 concludes the work and outlines future perspectives.

BONDING IN TRANSITION METAL COMPLEXES

This chapter will review some fundamental aspects of the possible mechanism involved in molecule bonding and their importance to understand metal complex properties as spectroscopic selection rules.

Before addressing the metal complexes, an introductory analysis of general symmetry allowed operations and group theory is presented. After that, two direct applications of these concepts are shown: the vibrational modes calculation and the allowed states for electric dipole transition. The explanation of the obtained absorption spectrum is provided either by the crystal field theory (CFT) or molecular orbital theory (MO), and is briefly commented in the following subsection.

2.1 Molecular symmetry

The concept of symmetry pops up in our sights every day, to demonstrate that something is beautiful and useful. The idea behind this topic is to find the symmetry operations that, upon certain conditions, lead to the set being unchanged. The allowed operations are: identity (E), rotation (C_n), reflection (σ), inversion (i) and improper rotation (S_n), as shown in Fig.2.1. When symmetry operations are applied to molecules, it is possible to classify them into groups, improving the analysis of obtained measurements.
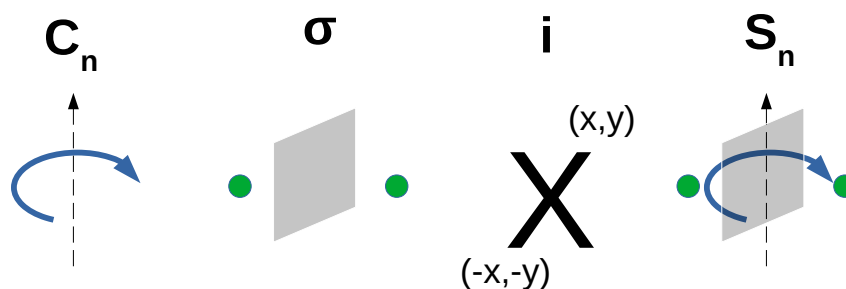
Figure 2.1 - Allowed symmetry operations.

The first symmetry operation is rotation (C_n), and is depicted in Fig.2.2 a). Four full circles are located at the same plane are differentiated by colors. The n number in C_n represents

the integer resulting from the division of 360° and the allowed angle that keeps the system indistinguishable. In case of a), $n = 360°/120° = 3$. The primary idea of symmetry operations is to "move" the objects under some rule so that they are kept unaltered compared to their original formation. In this scenario, it is possible to rotate the circles around one axis, which passes through their center, and is perpendicular to the plane of the particles, as depicted in the upper image in Fig. 2.2 a). In this case, the only allowed rotation is 120°. Although the colors have changed (lower left image), except the central one, they are indistinguishable from the position point of view. A second rotation also leads to a similar configuration. A third rotation, mathematically represented as $C_3 C_3 C_3 = C_3^3 = E$, yields the concept of identity, defined by the character E, and represents an operation that leads to a totally identical configuration.

Nevertheless, considering the same circles, one more rotation axes is found to be important for symmetry operation, and is shown in Fig. 2.2 b). A rotation of 180° around the axis that pass through the top and central atoms can produce the same structure, in which, in this case, two elements are kept fixed. However, C_2, allows fewer rotations than C_3. For this reason, C_3 is considered the main rotation axes.
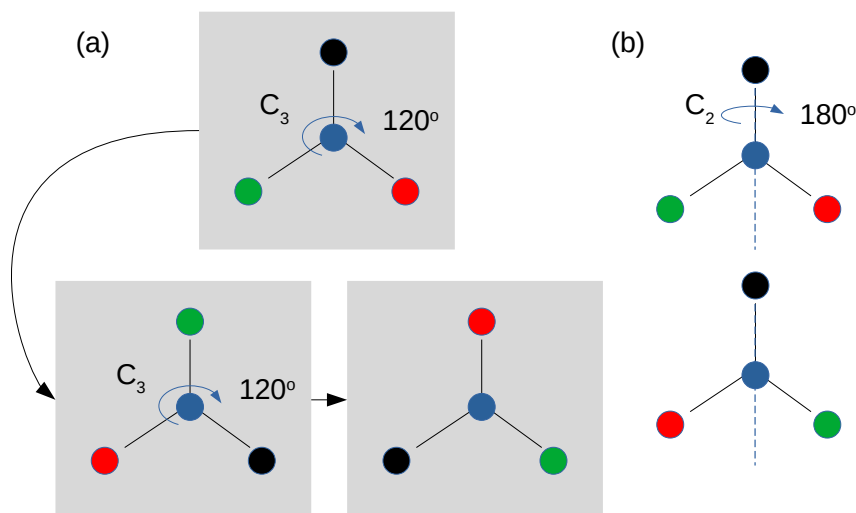
Figure 2.2 - Available C_n rotations for this particle arrangement.

The second symmetry operation is reflection, σ, around different planes and labeled as shown in Fig. 2.3 a). σ_h occur in a plane perpendicular to main rotational axes C_4. In this case, all circles are reflected, leading to an unchanged particle positioning. In Fig. 2.3 b) the σ_v plane is parallel to C_4 and crosses the fixed black and blue circles. The red circle is reflected on the other side of the plane, resulting in the original configuration. An identical σ_v plane is identified as one that is parallel to axes that pass through the black and blue circles while the red circles are reflected. The last reflection plane is σ_d, where d stands for dihedral and means a plane parallel to the main axes but passes through between two particles. In this example, the lower red and right black circles are reflected by σ_d resulting in the upper black and left red ones.

Inversion center, i, is a property related to a point whose all components in the vector
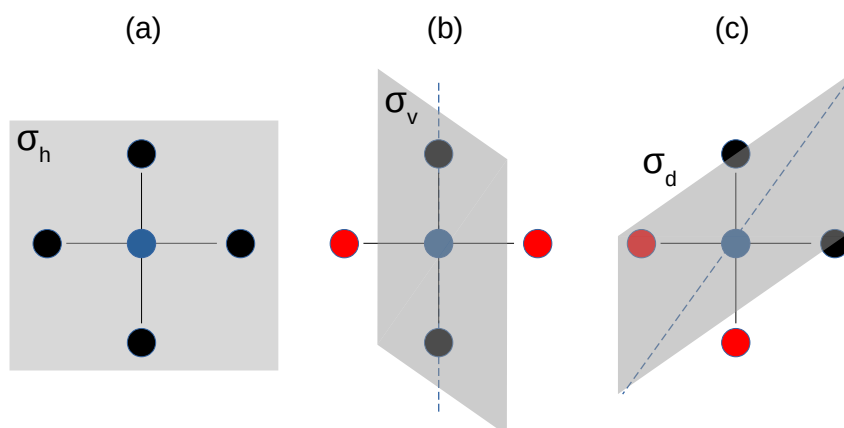
Figure 2.3 - Available σ planes for this particle arrangement. In a) is shown σ_h, in b) σ_v, and in c) σ_d.

location suffer an transformation, as shown in Fig. 2.4. The blue circle is the position of the inversion center, while the green and red ones are the inverses of each other.
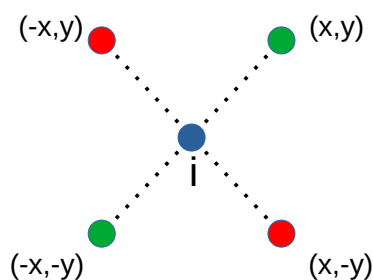
Figure 2.4 - Available i inverse center (blue circle) for this particle arrangement.

A combination of one rotation and one reflection leads to the symmetry operation called improper rotation S_n. This coupled movement is exemplified in Fig. 2.5. In a), a rotation of $90°$ has been performed and, subsequently, (b) a σ_h reflection to obtain the same form (c), as shown a).
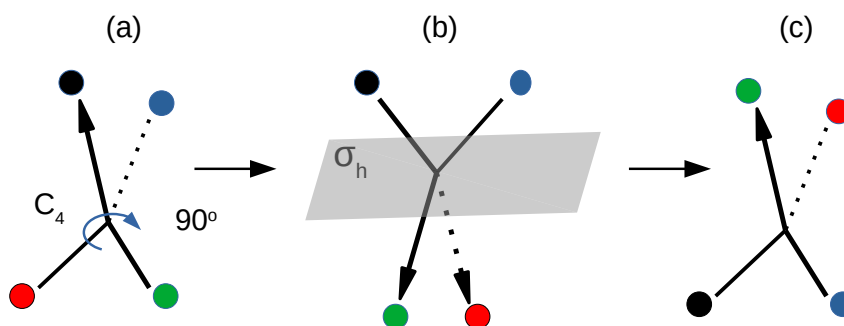
Figure 2.5 - Mechanism of S_n operation. In a) a rotation, then in b) a σ, resulting in S_n in c).

The concepts about symmetry operations can be extended to molecules, where it is possible to classify each of them within a collection of 32 groups, nominated as point groups, making use of Schönflies notation [34]. The Point group of any molecule can be determined by

following an algorithm-like procedure containing all individual symmetry allowed possibilities
that each group must have, as shown in details in Fig. A.1.

A general classification of point groups can be adopted to identify the molecular point
group. This classification can be non-rotational groups (represented by molecules with low sym-
metry, where C_1 is the lowest); single-axis rotational group; dihedral group and cubic groups
(molded by high symmetric molecules).

One interesting property based on symmetry is the optical activity or chirality. This
phenomenon means that an incident polarized light changes its direction when passing through
the molecule if the medium is optically active. This occurs only in molecules that do not possess
one axis of improper rotation, S_n, as the case of C_n, D_n, C_1, T, and O point group. Polarity of the
molecules is another consequence of molecular geometry since the resultant of dipole moments
must be nonzero. These condition can be achieved only when a molecule does not have an
inversion center and horizontal mirror plane as these operations make individual bond dipoles
equal. Therefore we can conclude that only molecules belonging to groups C_1, C_n, C_{nv}, and C_s
possess permanent electric dipole moment [35].

2.2   Group

An object, a set of circles, particles, and atoms in a molecule, sharing same symmetry
elements described above, can be understood as being part of a group. Generally speaking,
they are characterized by their mutual point group. Each group has its specific set of symmetry
operations and, mathematically, must follow four rules: closure rule; identity; associativity; and
inverse rule.

The closure rule states that two or more consecutive operations of elements within a
group result in an element that is also a group member, as exemplified in Fig. 2.6. In this
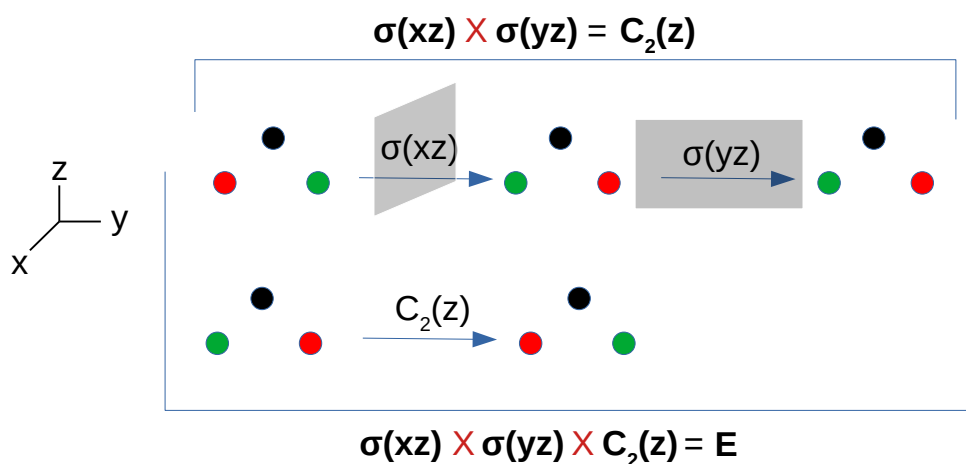
Figure 2.6 - Closure rule. Here, the $\sigma(xz)$ ($\sigma(yz)$) operation reflects the circles through the *xz* (*yz*) plane, and C_2 is
the principal axes of rotation passing through the *z* axes.

arrangement, the point group of the circles is C_{2v}. The position of the circles after $\sigma(xz)$ and $\sigma(yz)$ operation is identical to that of $C_2(z)$. Carrying on the operations, when $C_2(z)$ is applied to the last configuration, it results in the initial arrangement, which concludes that $\sigma(xz)$, $\sigma(yz)$, $C_2(z)$ results in E, also an element of the group.

Every group has an identity element (E), whose application in another group element keeps them unchanged, as shown in Fig. 2.7.

Figure 2.7 - Identity rule.

Another group rule is the inverse, which is the prediction of the existence of a member whose it is reciprocal, and the resultant of this element by its reciprocal gives identity. As shown in Fig. 2.8, the inverse of $C_2(z)$ is $C_2(z)$ and leads to E.
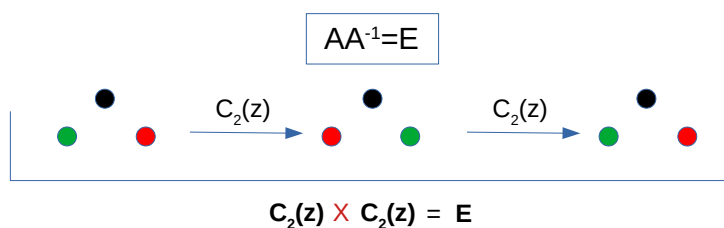
Figure 2.8 - Inverse rule.

The last group properties are associative. In this case, the resultant of the operations are independent of the association of the elements, as shown in Fig. 2.9. The final circle set remains unaltered independently of the order of the operations.
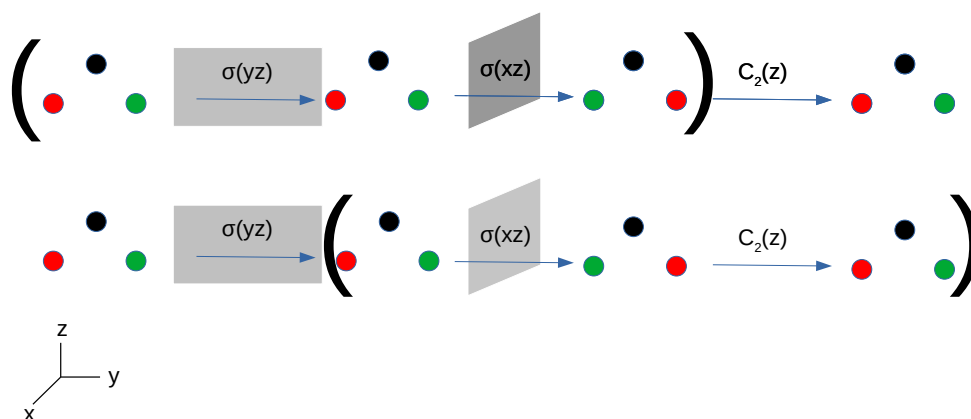
Figure 2.9 - Associative rule.

Information on symmetry operations and group properties allow us to build a way to represent them in the form of characters, which, in essential, identify the behavior of a molecule

of a particular symmetry under a specific symmetry operation [34]. The collection of charac-
ters forms a table known as a character table, as shown below in Table 2.1. It contains the
information on the basis that the group class operation results in an irreducible representation
summarized by a symbol. The numbers contained in this table are explained in Fig. 2.10. In

Table 2.1 - B_2 irreducible representation for C_{2v} point group.

C_{2v}	E	$C_2(z)$	$\sigma_v(xz)$	$\sigma_v(yz)$	linear function
B_2	+1	-1	-1	+1	y

Fig. 2.10, for example, the orbital p_y undergoes transformations belonging to C_{2v} group. The
highlighted number in parenthesis indicates the resultant orbital conformation required to keep
the original orbital form unchanged. So, under E operation, p_y remains identical, and the as-
sociated symbol receives +1 as a character. When $C_2(z)$ is applied, the right lobe switches
position with the left. In order to maintain its original orientation, a -1 operation is necessary,
which gives the corresponding character. Following the same instructions, it is possible to de-
duce all the characters that form the basis of the irreducible representation. The calculation of
corresponding characters from other orbitals can be seen in Appendix A.2.
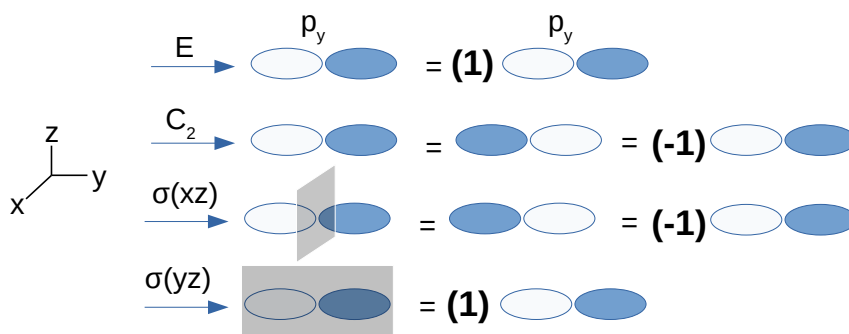
Figure 2.10 - The scheme for obtaining the characters in B_2 symmetry that is associated with the linear function
p_y. The numbers in parenthesis are the characters in respective symmetry operations.

In Table 2.2, it is possible to verify the complete C_{2v} point group character table. R.S.
Mulliken proposes a scheme for labeling the irreducible representations [36]. The group's name
is located at the top left of the table. The symbols A and B stand for unidimensional irreducible
representation, where the difference between them relies on the character of the principal rota-
tional axis. In this case, for A symbol, $+1$ character is required; otherwise, -1 character, will
labeled as B. Also, A_1 or A is used for the highest symmetry case, where all characters are $+1$,
and is associated with the s-like orbital due to its spherical symmetry. The subscripts are used
to distinguish the irreducible representation of the same kind. However, instead of the number,
when it presents a letter, such as g or u, it indicates that the representation is symmetric (from
the german word *gerade*) or antisymmetric (from the german word *ungerade*) for the inversion
operation. When higher dimensions are considered, that is, double or triple degenerated irre-
ducible representation, the character linked to the symmetry E (do not mistake to class E) and

T, is 2 and 3, respectively. It is commonly seen in these table indices accompanying the classes, where the index represents the number of allowed symmetry operations. The summation of all indices receives the name of order of the group h, and for C_{2v}, h is equal to 4.

Table 2.2 - C_{2v} character table.

C_{2v}	E	$C_2(z)$	$\sigma_v(xz)$	$\sigma_v(yz)$	linear function, rotations	quadratic functions
A_1	+1	+1	+1	+1	z	x^2, y^2, z^2
A_2	+1	+1	-1	-1	R_z	xy
B_1	+1	-1	+1	-1	x, R_y	xz
B_2	+1	-1	-1	+1	y, R_x	yz

2.3 Molecular vibrations

A free atom has three degrees of freedom, corresponding to the three coordinate axes. For N free atoms there are 3N degrees of freedom, as is shown in Fig. 2.11 for $N = 1, 2, 3$.
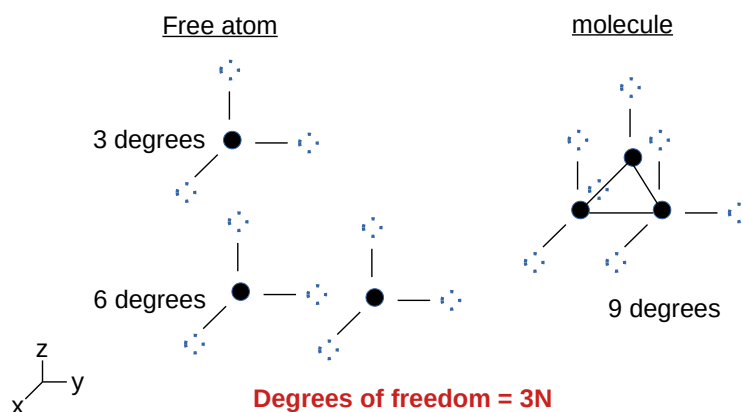
Figure 2.11 - Degrees of freedom for free atoms and molecule.

As a whole, a molecule has three translation degrees of freedom and three rotational degrees
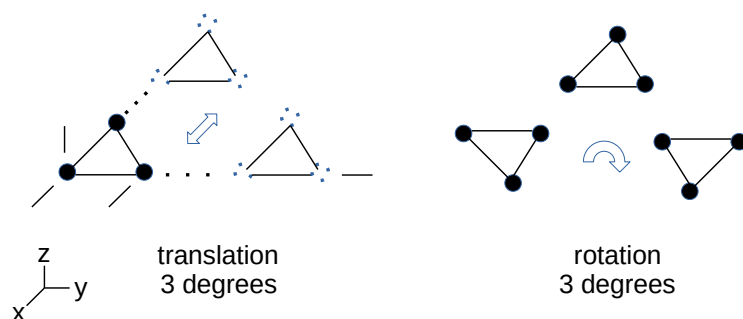
Vibrational modes = degrees of freedom - translation - rotation

Vibrational modes = 3N – 6

Figure 2.12 - Vibrational modes for non linear molecule.

of freedom. Hence, a molecule with N atoms presents $3N - 6$ degrees of freedom, where $3N$

comes from the translation motion of the *N* individual atoms and 6 from the sum of the molecule translation and rotation degrees of freedom, as is presented in Fig. 2.12 for $N = 3$.

The $3N$ allowed movements have to be written in terms of the symmetry operations and then translate to irreducible representations. Thus, to obtain the Γ_{3N} reducible representation (displacement coordinates), it is necessary to calculate the number of unshifted atoms in the molecule under each available operation class. Also, need to consider the contributions of co-ordinate vectors from every unchanged atom ($\chi_{u.a}$) [37], with each class contributing distinctly accordingly to Table 2.3.

Table 2.3 - Contributions of $\chi_{u.a}$ for all symmetry operations [37].

operation	$\chi_{u.a}$
E	3
i	-3
σ	1
C_n	$1 + 2\cos(360/n)$
S_n	$-1 + 2\cos(360/n)$

Carrying on the calculation for vibrational modes, taking the water molecule as example, all desired data are summarized in Table 2.4. The reducible representation Γ_{3N} is then obtained by product of unshifted atoms and $\chi_{u.a}$ characters. Thereafter, the procedure is to reduce the reducible representation using the reduction equation below [38]:

$$a_i = \frac{1}{h} \sum (n_R \chi_{(R)} \chi_{(IR)}), \qquad (2.1)$$

where a_i is the ith reduced representation, h is the order of the group, n_R is the number of operations in the class, $\chi_{(R)}$ is the character in the reducible representation and $\chi_{(IR)}$ is the corresponding character in the irreducible representation. Applying Eq. 2.1 yields the Γ_{3N} to be written in terms of its irreducible representation components, as shown below:

Table 2.4 - table of general data for obtaining Γ_{3N}.

C_{2v}	E	$C_2(z)$	$\sigma_v(xz)$	$\sigma_v(yz)$
unshifted atoms	3	1	1	3
$\chi_{u.a}$	3	-1	1	1
Γ_{3N}	9	-1	1	3

$$\Gamma_{3N} = 3A_1 + A_2 + 2B_1 + 3B_2. \qquad (2.2)$$

Eq. 2.2 reports all the movements. However, the actual interest is to obtain the vibra-

tional modes. In this case, Γ_{vib} can be described as:

$$\Gamma_{\mathrm{vib}} = 2A_1 + B_2. \tag{2.3}$$

Here, two vibration modes are from A_1 and one from B_2, with three modes in total, as expected by theoretical analysis ($3N-6$). By inspection of C_{2v} character table, we see that either A_1 and B_2 are mutually infrared and Raman vibrational active modes, since infrared modes are related to translation symmetry, and Raman modes to quadratic functions [34].

DFT calculations of infrared modes of a single water molecule, as seen in Fig. 2.13, exhibits an spectrum as in accordance with the experimental data [39]. The peak around 1584 cm^{-1} are refereed to A_1 bending mode, and the main peak at 3685 cm^{-1} is close to the one observed stretching B_2 mode. The details of these calculations are presented in Appendix A.3.
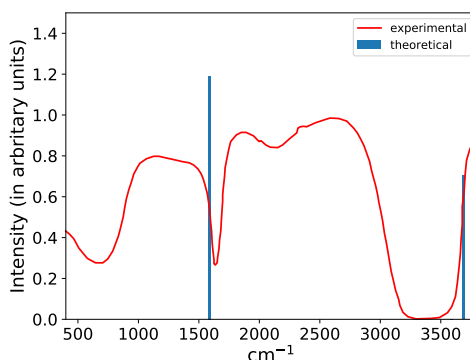
Figure 2.13 - Infra red spectrum comparison of water between theoretical calculation (blue lines) and experimental data (red line).

2.4 Electric dipole selection rule

The electric dipole selection rule is one of the main information provided by group theory, since it states the allowed symmetries available for the transition of electron from one state to other state. It depends on the initial and final states under an operation that, in general, is the electric dipole. Commonly, in quantum mechanics we face situations where it is necessary to calculate a matrix element $\langle n|\hat{\Omega}|m\rangle$, where n (m) can be understood as the wavefunction of final (initial) state, and $\hat{\Omega}$, the dipole operator in a specific direction. While the selection rule satisfies this case, performing this integral might require more work. However, group theory and character table can be used to ease this task, where a non-zero integral is indispensable, and this is guaranteed if A_1 symmetry species is presented [35].

For obtaining the allowed electric dipole transition, we must develop a direct product of the interest symmetries, as seen in Table 2.5. In the first row of this table, we observe the characters of the final state, considered a *s*-type orbital (the reason will be further explained in this chapter), meaning A_1 symmetry. The next row represents the characters of the dipole

Table 2.5 - Direct product in C_{2v} point group considering the final state as A_1 symmetry.

A_1	1	1	1	1
B_1	1	-1	1	-1
B_1	1	-1	1	-1
$A_1 \otimes B_1 \otimes B_1$	1	1	1	1

operator ($\overrightarrow{\mu_x}$) in a certain direction, and each one has the same symmetry as linear functions. Thus, B_1 corresponds to $\overrightarrow{\mu_x}$. The following row represents the symmetry from the initial state, symbolizing the p_x orbital, as shown in Table 2.2. Consequently, the direct product of these irreducible representations matches A_1 symmetry, as is shown in the last row; hence, this integral is non-zero, and the transition is electric dipole allowed. All other possible configurations are given in Appendix A.4 and summarized in Table 2.6.

Table 2.6 - Electric dipole selection rule considering a_1 as final state symmetry. Blank spaces indicate electric dipole forbidden transitions.

initial state polarization	a_1	b_1	b_2
x	-	allowed	-
y	-	-	allowed
z	allowed	-	-

DFT calculation of the water molecule, exhibits the absorption spectrum as a function of the three incident electric field directions, as displayed in Fig. 2.14. It shows that a_1 state is
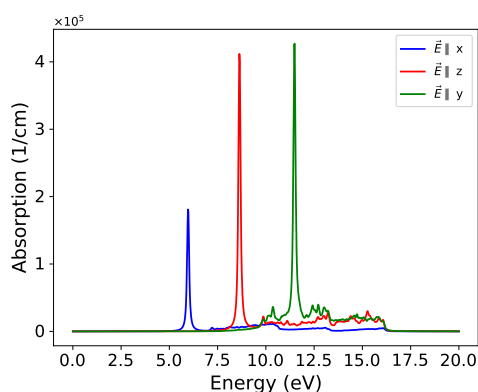
Figure 2.14 - Absorption spectrum of a single water molecule obtained via *ab initio* method.

the most suitable one as the lowest unoccupied molecular orbital (LUMO) since the first peak (blue line) around 6 eV comes from an incident light parallel to $\overrightarrow{x}$, meaning that the highest occupied molecular orbital (HOMO) have b_1 symmetry. More conveniently, this corresponds to a transition from p_x orbital to s orbital. In the same way, the HOMO -1 transition (red line) is due to transition from a_1 to a_1, and the last peak (green line) correspond to that from b_2 to a_1. Therefore, we can label the peaks of absorption arising from *ab initio* results via group theory.

2.5   Crystal field theory

In crystal field theory (CFT), Hans A. Bethe, in 1929, wrote the basis of the influence of an electric field of prescribed symmetry on an atom [**?**]. In order to do that, he also created the rules of point groups of levels in crystalline fields. At ordinary temperatures, susceptibilities follow Currie-Weiss's law for paramagnetic material. However, this equation fails to describe the experimental results in rare earth paramagnetic salts at low temperatures. In order to explore the above fact, the effect of electric field of the surrounding ions was considered, which could lower the symmetry and alter the degeneracy of energy levels, resulting in possible magnetic-moment modifications and, consequently, a change in the susceptibility [**?**]. Moreover, Penney and Schlapp in 1932, calculated the susceptibilities of salts of paramagnetic ions from the iron group, in which the $3d$ shells are incomplete, and were found to be more affected by the crystal field than the $4f$ electrons in rare earth salts [**?**]. These works helped to establish Bethe's concepts (splitting energy levels due to electrostatic potential produced by surrounding ions that are bonded to central metal), and Van Vleck's theory about electric and magnetic susceptibilities [**?**]. Although the theory primarily proposed is simple, it is still helpful to provide a qualitative understanding of the spectra and other properties of the transition metal complexes [**?**]. A theory that better explains this topic is given by the molecular orbital theory and ligand field theory.

CFT was designed to explain the properties of metal ions in crystal lattices. It is an electrostatic model which considers the effect of the electric field due to the ligand electronic charge on the energies of electrons in various orbitals of the metallic ion [**?**]. In a free ion, all d states are equivalent in energy, since there is no preferential orientation in a free space. However, it is different when an atom is located inside a crystal, where their crystallographic axes are relevant. This condition can be seen in Fig. 2.15 a), by which all five d subshells are degenerate at the lowest energy state.

In a negative uniform potential, the isolated metallic atom feels the presence of this spherical field, and an electrostatic repulsive force between the electrons of the free atom and surrounding field, results in the rising of the orbital's energy. Since the ion is within an isotropic field, there is no preferential axes direction. Therefore, all d orbitals from the central metal are equivalent, remaining degenerated, as Fig. 2.15 b) shows. However, if this metallic ion has no longer a surrounding spherical field, but four ligands forming a tetrahedral geometry around the central metallic ion, it will lower the symmetry of the compound (related to the spherical one) and, some ionic terms will interact more intensively due to higher proximity with some ligands than others. So, when electrostatic repulsion is more significant (that is, terms are more close to ligands), the orbitals will go to a higher energy level than those more distant, which will decrease their energy compared to a barycenter produced by the spherical crystal field, as in Fig. 2.15 c). This produces the crystal field splitting, and the consequence of this splitting may lead to different magnetic moment of materials.
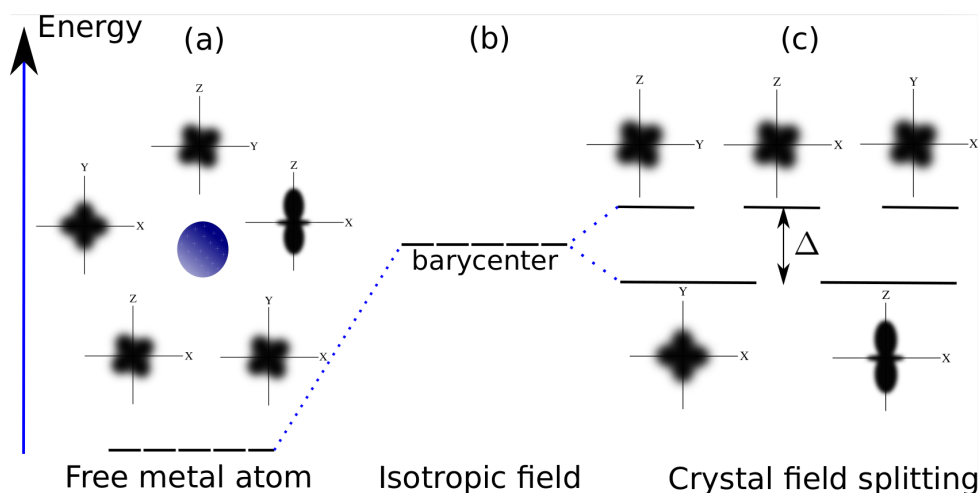
Figure 2.15 - Schematic formation of crystal field. In a), it is shown all five *d* orbitals from an isolated metal ion. In this case, all states are degenerate and, on an energetic scale, lie at the bottom. In b), one central metal atom is surrounded by an isotropic field, resulting in state energy rise due to electrostatic repulsion. In c), the metallic atom is inserted inside a crystal, where *d* orbitals interact with ligands, resulting in an energy splitting of the terms.

Due to the interest of clarify the presence of the crystal field and the mechanism of orbital splitting, we consider to represent the orbitals from the central atom in two distinct symmetries. In Fig. 2.16 a), which the d_{z^2} orbital of Ti (blue sphere) with an octahedral configuration, interacts directly (dotted arrow) with the ligands (red spheres). This interaction results in a Coulomb repulsion of intensity higher than those due to ligands that are not directly pointed out, as d_{xy} orbital (Fig. 2.16 b), which lies between the ligands. Consequently, in this geometry, the d_{z^2} orbital is at a higher energy state than d_{xy}. On the contrary, in a tetrahedron symmetry complex, when ligands (red spheres) in the z direction are not present, as seen in Fig. 2.16 c), d_{z^2} ($d_{x^2-y^2}$, as well) orbitals feel less Coulomb repulsion than others, such as d_{zx}, d_{zy} and d_{xy}.
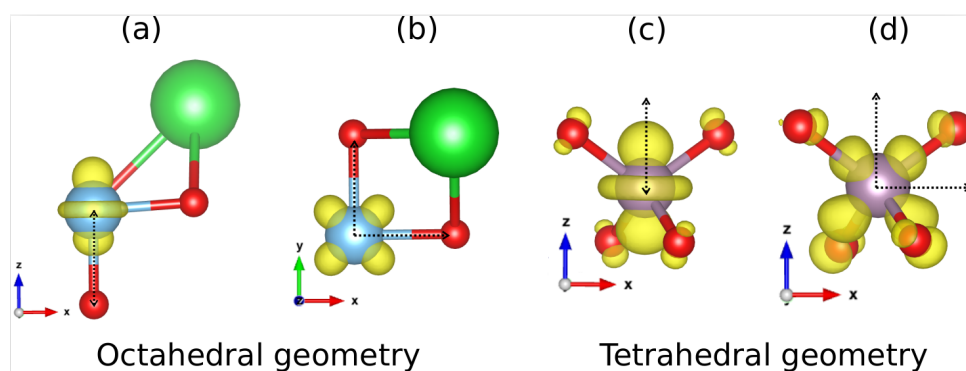
Figure 2.16 - Orbitals from metallic ion under two distinct symmetries. In a), we see dz^2 orbital from titanium (blue sphere) pointed to oxygen (red sphere) and, in b), the orbital dxy lies between the ligands (dotted arrow), both under octahedral geometry. For a tetrahedral complex, as seen in c), dz^2 orbital is not directly pointed to the ligand, but dzx, shown in d), is.

Based on the two symmetries shown in Fig. 2.16, we can build a simple diagram demonstrating the main differences between two crystal field splitting systems, where the left one is from the octahedral field (Fig. 2.17 a)), and the right exhibits the tetrahedral one. The energy states are labeled as t_{2g}, occupied by d_{zx}, d_{zy} and d_{xy}, and e_g, occupied by d_{z^2} and $d_{x^2-y^2}$. The

letter *t* means that three states are degenerate, and the subscript *g* means that these states have a symmetric center of inversion. That is, these states are unchangeable via center inversion. In the e_g label, where *e* is related to double degenerate orbitals. In tetrahedral field, Fig. 2.17 b), the *d* terms are separated into two degenerate states. The subscript *g*, which label is omitted because, in this symmetry, there is no inversion center. Moreover, the order of the states is switched. In general, crystal field splitting in octahedral geometry has a higher splitting parameter than tetrahedral.
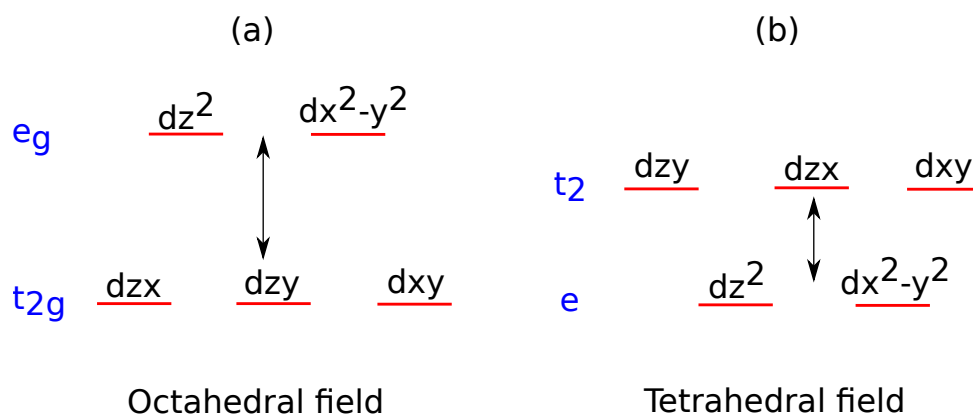
Figure 2.17 - The diagram shows CF splitting energy levels for two distinct symmetries. In a), there is an octahedral field, where the lower states are triple degenerate and labeled as t_{2g}. Above them are located double degenerate states called e_g. In b), the crystal under the tetrahedral field promotes a switch in the ordering of orbitals. We can see that the splitting energy (arrows) in the tetrahedral complex is lesser than in the octahedral one.

In order to exemplify the theory and how DFT may be used to construct the *d* orbitals energy shift, we have calculated the projected density of states (PDOS) on *d* orbitals of barium titanate (BaTiO$_3$), classified as perovskite-type, which has octahedral geometry. In Fig. 2.18 a), the conventional cell of BaTiO$_3$ is shown, where the blue sphere indicates Ti and the red and green spheres represent O and Ba, respectively. In Fig. 2.18 b), we have plotted the density of states of the *d* orbitals of Ti, where 0 eV is the energy of the highest occupied state. Ti has the oxidation state +4 in BaTiO$_3$, indicating a d^0 configuration. Hence, we observe a zero contribution from these states to valence and significant contributions to conductive bands. In this case, the valence bands are mainly populated by electrons from O 2*p*, whereas the conductive one is from Ti 3*d*. The way electrons from 3*d* orbitals are split by an octahedral crystal field follows Fig. 2.17 a), where $3d_{xy}$, $3d_{zx}$, and $3d_{zy}$ are the lower energy state, demonstrated by the black, green, and yellow lines, respectively, and above these states (t_{2g}), we see $d_{x^2-y^2}$ and d_{z^2} orbitals, the red and blue lines, respectively. This crystal field splitting, seen in Fig. 2.18 c), shows that the lowest states are not directly pointed to ligands, while the highest states possess their orbitals in the same direction as ligands.

(a)

(b)

BaTiO3

(c)
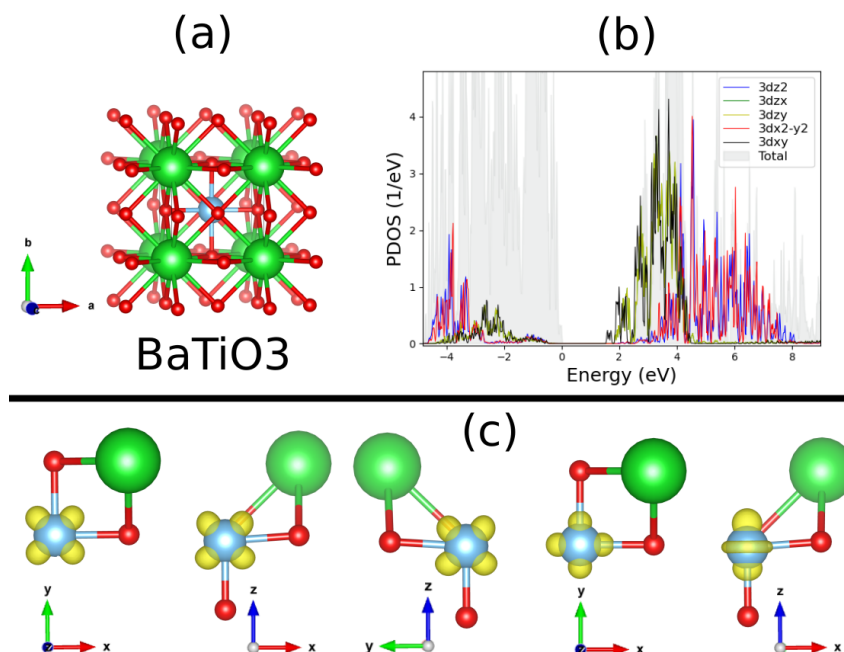
Figure 2.18 - Example of octahedral crystal field applied to a material. In a), we see the conventional cubic cell of $BaTiO_3$, composed of Ti (blue sphere) in the center of the crystal forming six bonds to oxygens (red spheres) and at the corners, Ba atoms (green spheres). In b), we have plotted the PDOS on $3d$ orbitals from Ti and compared them to the total. It is possible to see the orbitals of t_{2g} states occupying the bottom of conductive bands and after the occupation by e_g. The highest occupied band is at 0 eV. All d orbitals from Ti are plotted in c) and were obtained from bands calculation. From left to right, we have the following orbitals: dxy, dzx, dzy, $dx^2 - y^2$, and dz^2.

2.6 Molecular orbital theory

Molecular orbital (MO) theory and valence bond theory (VBT) use quantum mechanics to explain the origin of bonds in molecules. MO theory was developed and improved over many years. However, its formal establishment is attributed to Robert Sanderson Mulliken, due to his fundamental notion of molecular orbitals together with a rigorous mathematical approach that could potentially benefit a more accurate theory in chemistry [40]. For his enormous contribution to MO theory, Mulliken received the Nobel Prize in Chemistry in 1966 "for his fundamental work concerning chemical bonds and the electronic structure of molecules by the molecular orbital method" [41]. Mulliken himself addressed spectroscopy, which paved the way towards MO theory [42], since VBT could not correctly interpret some excited molecules spectra. MO is more suitable for understanding the electronic structure and, consequently, electronic spectra of molecules and their photochemical behavior. In this subsection, we intend to introduce the fundamental concepts on MO and indicate a manner for sketching the molecular orbitals diagram under its irreducible representations based on DFT calculations.

MO theory can be understood as being one electron wavefunction replacing atomic orbital description. The valence electrons occupy the molecular orbitals that are spread all over the molecule as a linear combination of atomic orbitals [43]. Therefore, the electrons describe the molecule as a whole instead of orbitals from individual atoms. Since MO is a wavefunction,

it can interact constructively or destructively. Constructive overlap occurs when there is an increase in the electronic density. The MO involved in the above case is called bonding orbital, because an increase in the electronic density means that the probability of finding one electron is more significant between two nuclei. On the other hand, antibonding (generally indicated by an upper *) is when the interference is destructive. As a consequence, the probability of finding an electron lies outside the inter-nuclei region, since a nodal plane is generated between two nuclei. Bonding orbital also lowers the energy in relation to separated atoms, promoting stabilization to molecule, while antibonding destabilizes. For each bonding orbital, there is an antibonding one. The number of MO is equal to the atomic orbital from the atoms participating in the bond. Nonbonding orbitals neither contribute to the stabilization nor destabilization of the molecule, and it is generally occupied by electrons that cannot interact with other orbitals due to their symmetry.

In order to exemplify those concepts as mentioned above, we show in Fig. 2.19 the MO of water, which is adapted from Kettle [34]. On the right side is the individual s orbital from the hydrogen atoms, which, as they are the ligands, we performed a symmetry adapted linear combination (SALC) of these orbitals to match the symmetry of the central atom. It makes the original orbitals split into two different symmetry orbitals, labeled as a_1, which is the fully symmetric case (constructive interference) and b_2 orbital, which stands for destructive interference case [44]. While on the left side, we have the valence orbitals $2s, 2p_z, 2p_x, 2p_y$ with the respective symmetries given by $A_1, A_1, B_1 and B_2$. Due to more electronegative nature of oxygen when compared to hydrogen, its corresponding s orbital lies at lower energy. It is worth mentioning that all initial p-like orbital possess the same energy. The three levels displayed in the figure provide a more explicit representation. In the middle of this diagram are the MOs. The corresponding mechanism of MO requires the knowledge about symmetry of the original orbitals. Moreover, it follows Hund's law, where electrons occupy the lowest bonding $1a_1$ MO first and so on, until the $1b_1$ nonbonding highest occupied molecular orbital (HOMO). The previous assumption, in Table. 2.5 for the final state symmetry, demonstrated to be the correct one since, from the MO diagram, the LUMO state possesses a_1 symmetry.

We have calculated the bands of energy and projected density of state (PDOS) of water to validate the obtained sketch for H_2O molecular orbitals through DFT results. So, the achieved results are shown in Fig. 2.20. In a) the shapes of the molecular orbitals and their symmetry are shown, and, in b), it is possible to see the band structure of a single water molecule through a path including some high symmetric points in the Brillouin zone. The yellow region represents the energy gap of water, where LUMO has a_1 symmetry, in accordance with MO theory. Also, the shape of LUMO is in accordance with theory since one of its lobes is smaller than the other (far from the ligands). For HOMO, the shape shows no contribution from hydrogen, as expected, and HOMO is a nonbonding b_1 symmetry MO populated by electrons from p_x orbitals. These wave vectors ($\vec{k}$) have specific symmetry properties as well electron energy bands asso-
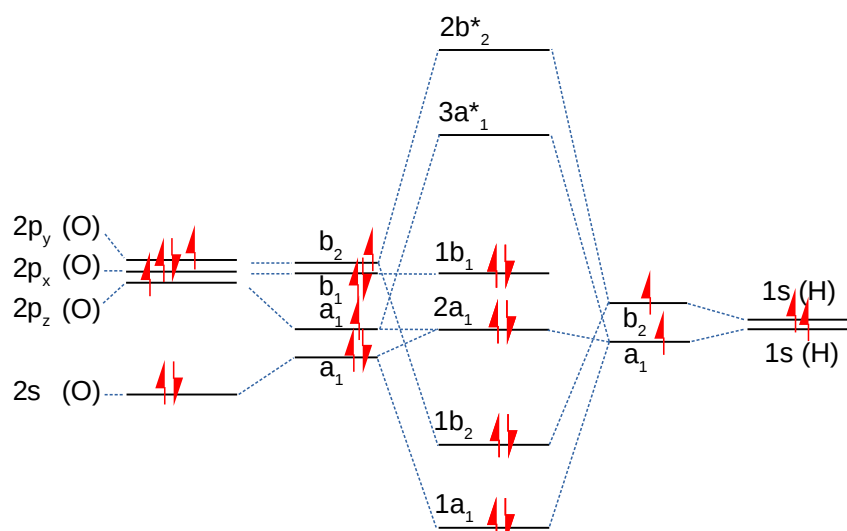
Figure 2.19 - Molecular orbital diagram of water. On the left side are shown the valence orbitals from O, in the right the orbital from the ligands, and in the middle the molecular orbitals of water labeled according to its symmetry.

ciated [45]. Then, this way provides for each band and each point in the chosen path a symmetry label corresponding to the allowed symmetry operation, as shown in a). PDOS are pictured in c) and corroborates to above discussion, which can be used, among other explanations, to identify the molecular orbitals.
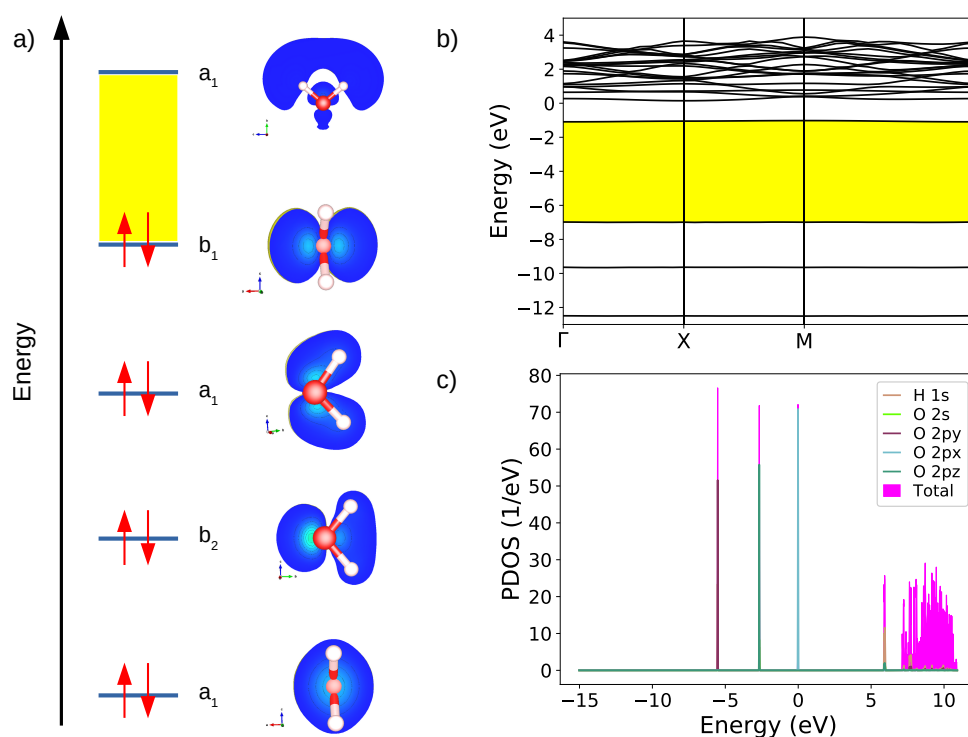
Figure 2.20 - In this figure, we show a) the schematic MO of water and its molecular shapes, b) the band spectrum of a single water molecule and c) the projected density of states on the valence orbitals normalized by the HOMO energy. The yellow area means the energy gap region.

However, the focus is the bonding mechanism of the coordination complex, that is, one central metal bonded to a nonmetal, e.g., oxygen, forming atomic conglomerates known as a

cluster. MO theory is suitable for determining the qualitative bonding description in metal complexes of the type $[ML_n]^m$, including $[MoO_4]^{-2}$ [46]. The electronic properties of transition metal compounds are determined, mainly, by the nature of ligands, and, only in some exceptional cases, are affected by a more distant neighbor from metal ion [47]. In a simple molecule, the central atom contains only *s* and *p* orbitals. However, in metal, it is composed of an extra *d* orbitals which can be combined with the ligands in a new set of delocalized orbitals with appropriated symmetry to form bonding, antibonding and nonbonding MO. These orbitals can be ordered and labeled using the irreducible representation symbols of the symmetry point group of the cluster [48]. The way these orbitals interact with the orbitals from ligands is not trivial. However, the basic concept of creating SALC is still valid.

Due to the high complexity that these MO could achieve, it makes it necessary to represent them through theoretical calculations, obtained, for example, via *ab initio* computation within DFT theory-based software. The overview of this theory will be presented in the next chapter.

METODOLOGY

In this chapter, we will review the basic concepts on the theories that are essential for the programs we used. i.e., QE and their packages, which was used to understand the physical properties like band spectrum, the density of state, absorption and index of refraction spectrum, bulk and Young modulus, conductivity, the figure of merit, etc.

3.1 Density functional theory

Density functional theory (DFT) is a method used to describe the electronic structure of many-body systems. It is a powerful theoretical tool that can (with high accuracy) predict the electronic structure of molecules and solids and has become an invaluable tool in modern materials research. DFT is an *ab initio* method which states that the total energy of a system of electrons is a functional of the electron density, that is a fundamental quantity in DFT and contains all the information about the system.

It is mainly based on the Hohenberg-Kohn theorems [49] which provide a rigorous proof of the existence and uniqueness of the ground state of a given many-body system. The theorems were formulated in 1964 by Pierre Hohenberg and Walter Kohn which demonstrate that there is a one-to-one correspondence between the ground-state density of an N-electron system and the external potential acting on it [50]. For the N-electron system, a significant simplification concerning this equation has been made to reduce the number of variables. Since the focus lies on the systems where the position of the ions is practically unchanged (solid state), the nuclei are considered immobile; thus, its kinetic energy in relation to electrons is not considered. In addition, Coulomb's repulsion between the nuclei is a constant. Therefore, the many-electrons equation, in atomic units, is:

$$\hat{H}(\mathbf{r}_1, \mathbf{r}_2, \ldots, \mathbf{r}_N) = -\sum_i \frac{1}{2}\nabla_i^2 + \sum_i V_n(\mathbf{r}_i) + \frac{1}{2}\sum_{i \neq j} \frac{1}{|\mathbf{r}_i - \mathbf{r}_j|}, \qquad (3.1)$$

where the first term is related to the electron's kinetic energy, the middle term is the external potential arising from the Coulomb interaction between the nuclei and electrons, and the last term is the electron repulsion. Completing the Hohenberg-Kohn theorem, the ground-state

density is given by:

$$n(\mathbf{r}) = \sum_i |\psi_i(\mathbf{r})|^2, \tag{3.2}$$

which is a functional of $\psi(\mathbf{r})$, and $\psi(\mathbf{r})$ is a unique functional of $n(\mathbf{r})$. Since $\psi(\mathbf{r})$ defines the many-electrons Hamiltonian, the ground state of this system is also a unique functional of $n(\mathbf{r})$.

An important consequence of the Hohenberg-Kohn theorem is the formulation of a variational principle concerning the ground-state density of a system. Since Ψ is the ground-state many-body wavefunction and a functional of $n(\mathbf{r})$, kinetic energy $(\hat{T})$ and the Coulomb repulsion energy $(\hat{W})$ are also considered as function of $n(\mathbf{r})$. Therefore, the total energy E can be defined as:

$$E[n] = \int d\mathbf{r}\, n(\mathbf{r}) V_n(\mathbf{r}) + F[n], \tag{3.3}$$

where $F[n] = \langle \Psi[n]|\hat{T} + \hat{W}|\Psi[n]\rangle$ is a universal functional, valid for any external potential. The Eq. 3.3 is minimal at the exact ground-state density, and its minimum gives the ground-state energy of the many-electron system. One can split the functional $F[n]$ separating the Coulomb interaction due to its long-range behavior. Thus, $F[n]$ is given by:

$$F[n] = \frac{1}{2} \int \frac{n(\mathbf{r})n(\mathbf{r}')d\mathbf{r}d\mathbf{r}'}{|\mathbf{r}-\mathbf{r}'|} + G[n], \tag{3.4}$$

where the integral is written as the Hartree potential and $G[n]$ is a universal functional like $F[n]$. Then, we can write,

$$E[n] = \int d\mathbf{r}\, n(\mathbf{r}) V_n(\mathbf{r}) + \frac{1}{2} \int \frac{n(\mathbf{r})n(\mathbf{r}')d\mathbf{r}d\mathbf{r}'}{|\mathbf{r}-\mathbf{r}'|} + G[n]. \tag{3.5}$$

This is the starting point of Kohn-Sham equations [51]. The idea of Kohn and Sham was to split the implicit density-dependent terms (those within $G[n]$) into the kinetic and Coulomb energy of independent electrons (like in single-particle Schrödinger equation) and add an extra term including the effects of exchange and correlation. Thus, $G[n]$ becomes:

$$G[n] \equiv T_s[n] + E_{xc}[n], \tag{3.6}$$

where $T_s[n]$ is the kinetic energy of non-interacting electrons with density $n(\mathbf{r})$ and $E_{xc}[n]$ is the exchange and correlation energy of an interacting system with density $n(\mathbf{r})$. Therefore, Eq. 3.5 displayed in its complete form [52] can be written as,

$$E[n] = \int d\mathbf{r}\, n(\mathbf{r}) V_n(\mathbf{r}) - \sum_i \int d\mathbf{r}\, \phi_i^*(\mathbf{r}) \frac{\nabla^2}{2} \phi_i(\mathbf{r}) + \frac{1}{2} \int \int d\mathbf{r}d\mathbf{r}' \frac{n(\mathbf{r})n(\mathbf{r}')}{|\mathbf{r}-\mathbf{r}'|} + E_{xc}[n], \tag{3.7}$$

with ϕ_i being the single-particle wavefunction. As a consequence, the ground-state density $n(\mathbf{r})$ can be decomposed exactly to a sum of N independent and orthonormal orbitals, i.e., $n(\mathbf{r}) =$

$\sum_i^N \phi_i^*(\mathbf{r})\phi_i(\mathbf{r})$. This density precisely minimizes the total energy $E[n]$; hence, by variational principle we have

$$\frac{\delta E[n]}{\delta n} = 0, \tag{3.8}$$

which allows us to obtain the Kohn-Sham equations, as follows:

$$\left[-\frac{1}{2}\nabla^2 + V_n(\mathbf{r}) + V_H(\mathbf{r}) + V_{xc}(\mathbf{r}) \right] \phi_i(\mathbf{r}) = \varepsilon_i \phi_i(\mathbf{r}), \tag{3.9}$$

where V_n is the external potential, V_H, the Hartree potential, and the extra term, V_{xc}, the exchange-correlation,

$$V_{xc}(\mathbf{r}) = \frac{\delta E_{xc}[n]}{\delta n}. \tag{3.10}$$

The Eq. 3.9 is the central equation to the first-principle materials modeling. Up to this point, the Kohn-Sham equations are exactly solvable; however, V_{xc} has no defined expression, and for this reason, requires an approximate method to construct $E_{xc}[n]$. Once the exchange and correlation potential are defined, the Kohn-Sham equation is solvable self-consistently [53]. The first part is to define a trial density $n^{(1)}$, which is connected to the initial potential

$$v_{\mathbf{ext}}^{(1)}(\mathbf{r}) = V_n(\mathbf{r}) + V_H[n^{(1)}](\mathbf{r}) + V_{xc}[n^{(1)}](\mathbf{r}). \tag{3.11}$$

Using Kohn-Sham equation of the form

$$\left[-\frac{1}{2}\nabla^2 + v_{\mathbf{ext}}^{(1)}(\mathbf{r}) \right] \phi_i(\mathbf{r}) = \varepsilon_i \phi_i(\mathbf{r}), \tag{3.12}$$

one can obtain the orbitals $\phi_i^{(2)}$ which lead to an improved density $n(\mathbf{r})^{(2)}$ given by $n(\mathbf{r})^{(2)} = \sum_i \phi_i^{(2)*} \phi_i^{(2)}$. The density $n(\mathbf{r})^{(2)}$ can be used once again to improve the potentials $V_H[n^{(2)}](\mathbf{r})$ and $V_{xc}[n^{(2)}](\mathbf{r})$, until the difference between the densities acquired in two successive iterations has no more than an established predefined accuracy.

3.2 Spin in density functional theory

In this section, we will briefly discuss the procedure for obtaining the equations concerning the introduction of the spin into the density functional theory. All the assumptions taken in the previous section are still valid; however, adding spin induces a change in the functional, which now must account for the spin density contribution. The extension of the Hohenberg-Kohn theorem to spin-DFT is summarized below:

$$\text{DFT} \quad : \qquad n(\mathbf{r}) \longrightarrow E = F[n(\mathbf{r})]$$

$$\text{spin-DFT} \quad : \qquad n(\mathbf{r}), \mathbf{s}(\mathbf{r}) \longrightarrow E = G[n(\mathbf{r}), \mathbf{s}(\mathbf{r})], \tag{3.13}$$

where $\mathbf{s}(\mathbf{r})$ is the density of spin-angular momentum, or in short, spin density. The quantities expressed in Eq. 3.13 in its complete form:

$$n(\mathbf{r}) = \sum_i \Psi_i^\dagger(\mathbf{r})\Psi_i(\mathbf{r}), \tag{3.14}$$

$$\mathbf{s}(\mathbf{r}) = \sum_i \Psi_i^\dagger(\mathbf{r})\mathbf{S}(\mathbf{r})\Psi_i(\mathbf{r}), \tag{3.15}$$

with $\mathbf{S} = \frac{\hbar}{2}\vec{\sigma}$ being the spin operator, $\vec{\sigma}$ the Pauli matrices, and the 2-spinors is given by:

$$\Psi_i(\mathbf{r}) = \phi_i(\mathbf{r};1)\chi_\uparrow + \phi_i(\mathbf{r};2)\chi_\downarrow. \tag{3.16}$$

Using Eqs. 3.14, 3.15, and 3.16, we obtain

$$n(\mathbf{r}) = \sum_i |\phi_i(\mathbf{r};1)|^2 + \sum_i |\phi_i(\mathbf{r};2)|^2, \tag{3.17}$$

$$s_x(\mathbf{r}) = \frac{\hbar}{2} 2\,\mathrm{Re}\sum_i \phi_i^*(\mathbf{r};1)\phi_i(\mathbf{r};2), \tag{3.18}$$

$$s_y(\mathbf{r}) = \frac{\hbar}{2} 2\,\mathrm{Im}\sum_i \phi_i^*(\mathbf{r};1)\phi_i(\mathbf{r};2), \tag{3.19}$$

$$s_z(\mathbf{r}) = \frac{\hbar}{2}\sum_i \left[|\phi_i(\mathbf{r};1)|^2 - |\phi_i(\mathbf{r};2)|^2\right]. \tag{3.20}$$

In the above equations, the sum is performed over all the electrons, and the quantities $n(\mathbf{r})$ and $\mathbf{s}(\mathbf{r})$ are commonly written in terms of a compact object called the density matrix [54], defined as follows:

$$n_{\alpha\beta}(\mathbf{r}) = \sum_i \phi_i^*(\mathbf{r};\alpha)\phi_i(\mathbf{r};\beta), \tag{3.21}$$

where α and β can have values of 1 or 2 to associate it to the spinor components $\chi_\uparrow$ and $\chi_\downarrow$. From this point, the mechanism for minimizing the functional $E = G[n_{\alpha\beta}]$ is similar to those used in the Kohn-Sham equation (Eq. 3.8), where E is a functional of the density matrix. Hence,

$$\frac{\delta G[n_{\alpha\beta}]}{\delta n_{\alpha\beta}} = 0, \tag{3.22}$$

which leads to the Kohn-Sham equations for the spin case, as shown below:

$$\left[-\frac{1}{2}\nabla^2 + V_n(\mathbf{r}) + V_H(\mathbf{r})\right]\phi_i(\mathbf{r};\alpha) + \sum_\beta v_{\alpha\beta}^{xc}(\mathbf{r})\phi_i(\mathbf{r};\beta) = \varepsilon_i\phi_i(\mathbf{r};\alpha), \tag{3.23}$$

with $v_{\alpha\beta}^{xc}(\mathbf{r})$ being the exchange and correlation potential, defined by:

$$v_{\alpha\beta}^{xc}(\mathbf{r}) = \frac{\delta E_{xc}}{\delta n_{\alpha\beta}}. \tag{3.24}$$

Kübler *et al.* [54] showed a way to rewrite the exchange and correlation potential so that it becomes more physically meaningful, which is given by

$$v_{\alpha\beta}^{xc}(\mathbf{r}) = V_{xc}(\mathbf{r})\mathbf{1} + \mu_B \vec{\sigma} \cdot \vec{B}_{xc}(\mathbf{r}). \tag{3.25}$$

From this relation, we obtained the Kohn-Sham equations in a compact form for spin-DFT [52], as shown below. This equation is analogous to Eq. 3.9, despite the additional term $\vec{B}_{xc}$, which is the effective magnetic field generated by the electrons called exchange and correlation magnetic field. Considering the unpolarized case, $\vec{B}_{xc} = 0$, the spin-DFT equations fall into the traditional DFT, Eq. 3.9, as expected. Thus,

$$\left[-\frac{1}{2}\nabla^2 + V_n(\mathbf{r}) + V_H(\mathbf{r}) + V_{xc}(\mathbf{r}) + \mu_B \vec{\sigma} \cdot \vec{B}_{xc}(\mathbf{r}) \right] \Psi_i(\mathbf{r}) = \varepsilon_i \Psi_i(\mathbf{r}). \tag{3.26}$$

If we consider the collinear case, the electron densities up and down can be defined as:

$$n_\uparrow(\mathbf{r}) = \sum_{i\uparrow} |\phi_{i\uparrow}(\mathbf{r})|^2, \;\; n_\downarrow(\mathbf{r}) = \sum_{i\downarrow} |\phi_{i\downarrow}(\mathbf{r})|^2, \tag{3.27}$$

and the magnitude of the magnetization along the z axis is given by $n_\uparrow(\mathbf{r}) - n_\downarrow(\mathbf{r})$, in units of Bohr magneton, μ_B.

3.3 Approximation for the exchange and correlation functional

Through the Kohn-Sham equations, it is known that there is a functional E_{xc} which provides the exact density and, consequently, the ground state energy of this system. However, its formal definition still needs to be discovered. Hence, to overcome this issue, Kohn and Sham proposed an approximate relation for the $E_{xc}[n]$, as:

$$E_{xc}^{\mathrm{LDA}}[n] = \int n(\mathbf{r})\varepsilon_{xc}(n(\mathbf{r}))d\mathbf{r}, \tag{3.28}$$

where $\varepsilon_{xc}(n)$ is the exchange and correlation energy per electron of a uniform electron gas of density n. The electronic density distribution in a molecule is inhomogeneous. However, we can assume its homogeneity in a small portion of the space. In Fig. 3.1, we show a representation of this technique called local density approximation (LDA). LDA is based on the assumption that the electron density of a system can be divided into small regions, each of which is treated as a homogeneous system with a constant local electron density. The LDA then approximates the energy of the system by using the local electron density to calculate the exchange and correlation energies of each region. The total energy of the system is obtained by summing over all of the regions.
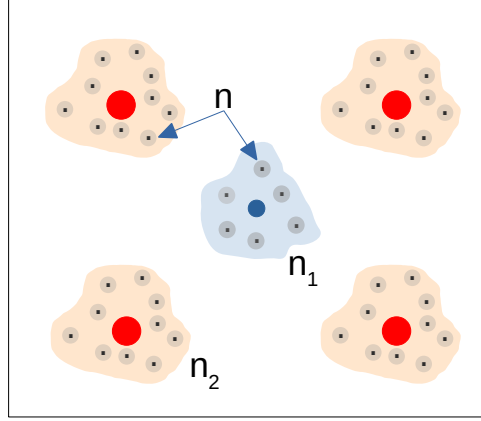
Figure 3.1 - This image shows a schematic representation of the local density approximation (LDA) procedure. In this picture, we have two distinct sets of atoms with similar densities n_1 and n_2, representing a molecule. The red and blue circles are the core of the ions, the dots represent the electrons, and the gray circles surrounding the electrons are the infinitesimal volume element that guarantees the same density, n, for all constituents of the electron cloud.

So, using Eq. 3.28 the exchange-correlation potential becomes

$$V_{xc}^{\text{LDA}}(\mathbf{r}) \equiv \frac{\delta E_{xc}^{\text{LDA}}[n]}{\delta n(\mathbf{r})} = \varepsilon_{xc}(n(\mathbf{r})) + n(\mathbf{r})\frac{d\varepsilon_{xc}(n(\mathbf{r}))}{dn(\mathbf{r})}. \tag{3.29}$$

In analogy to the Kohn-Sham procedure, in the local density approximation, the total ground-state energy is given by

$$E_0^{\text{LDA}} = \sum_i \varepsilon_i - \frac{1}{2}\int n(\mathbf{r})\frac{e^2}{|\mathbf{r}-\mathbf{r}'|}n(\mathbf{r}')d\mathbf{r}d\mathbf{r}' - \int n(\mathbf{r})\left[\frac{d\varepsilon_{xc}}{dn}\right]_{n=n(\mathbf{r})} n(\mathbf{r})d\mathbf{r}. \tag{3.30}$$

One can split the exchange-correlation energy, ε_{xc}, into two parts, ε_x and ε_c. For exchange energy, ε_x, the simplest model of interacting electrons, the homogeneous electron gas (HEG), provided an exact expression, yielding [52]:

$$\varepsilon_x = -\frac{3}{4}\left(\frac{3}{\pi}\right)^{1/3}\int n(\mathbf{r})^{4/3}d\mathbf{r}. \tag{3.31}$$

Several expressions for ε_c were developed; however, the most used was proposed by Perdew and Zunger [55], which is a parametrization of the correlation energy obtained by Ceperley and Alder [56] via Monte Carlo calculations. For unpolarized homogeneous electron gas, we have:

$$\varepsilon_c(r_s) = \begin{cases} -0.1423/(1+1.0529\sqrt{r_s}+0.3334\,r_s), & \text{for } r_s \geq 1, \\ -0.0480 + 0.0311\ln r_s - 0.0116\,r_s + 0.0020\,r_s\ln r_s & \text{for } r_s < 1, \end{cases} \tag{3.32}$$

with r_s being the dimensionless Wigner-Seitz radius, which is the ratio between the radius of the sphere, which is on the average occupied by a single electron of the gas, and the Bohr radius,

a_0,

$$r_s = \left(\frac{3}{4\pi n_0}\right)^{1/3} \frac{1}{a_0}. \tag{3.33}$$

LDA itself does not accurately reproduce some results, even of great importance for structural optimization. In order to provide a better description of the exchange and correlation energies, other approaches, including the effects of exchange and correlation beyond the local density approximation, were proposed [57]. As pointed out by Becke [58], LDA underestimates the exchange energies by about 10%. He also suggested a modified gradient-corrected exchange-energy functional, contributing to a refined version of a gradient-generalized approximation (GGA) functional by Perdew, Burke, and Ernzerhof (PBE) [59], which will be used for our calculations in this thesis. GGA adds corrections for gradient terms of the electron density to account for the non-uniformity of the local electron density, resulting in improved accuracy over LDA. The base GGA equation is:

$$E_{xc}^{\text{GGA}}[n_\uparrow, n_\downarrow] = \int d^3 r \, f(n_\uparrow, n_\downarrow, \nabla n_\uparrow, \nabla n_\downarrow). \tag{3.34}$$

In the PBE scheme, all parameters are fundamental constants. The exchange and correlation in this formalism are given by:

$$E_c^{\text{GGA}}[n_\uparrow, n_\downarrow] = \int d^3 r \, n[\varepsilon_c^{\text{HEG}}(r_s, \zeta) + H(r_s, \zeta, t)], \tag{3.35}$$

$$E_{xc}^{\text{GGA}}[n_\uparrow, n_\downarrow] = \int d^3 r \, n \varepsilon_x^{\text{HEG}}(n) F_{xc}(r_s, \zeta, s). \tag{3.36}$$

Its straightforward form and intuitive derivation are the main reasons for the success of this functional.

3.4   Pseudopotential

Since the works of Lewis on the bonding mechanism, it is well known that valence electrons play a crucial role in forming molecules and more complex structures. The full description of the Kohn-Sham equations implies dealing with rapid oscillating wavefunctions near atomic nuclei. Considering a regular arrangement of the atoms, it is convenient to use a set of planewaves to represent the Kohn-Sham wavefunctions as a linear combination of such waves since they satisfy the periodic boundary conditions in the system of interest [52]. This procedure allows us to write the Kohn-Sham wavefunctions as a Fourier series, which depends on the number of planewaves. Although more planewaves indicate more computational efforts, more accuracy can be achieved. Therefore, the oscillatory part, which embraces the core electrons, requires many planewaves to describe this behavior correctly. One mechanism to overcome

this issue involves separating the atoms into core and valence electrons. This can be done by the usage of the pseudopotentials technique. A historical well-studied pseudopotential is those proposed by Hamann *et al.*, known as norm-conserving pseudopotential [60], whose pictorial description is shown in Fig. 3.2.
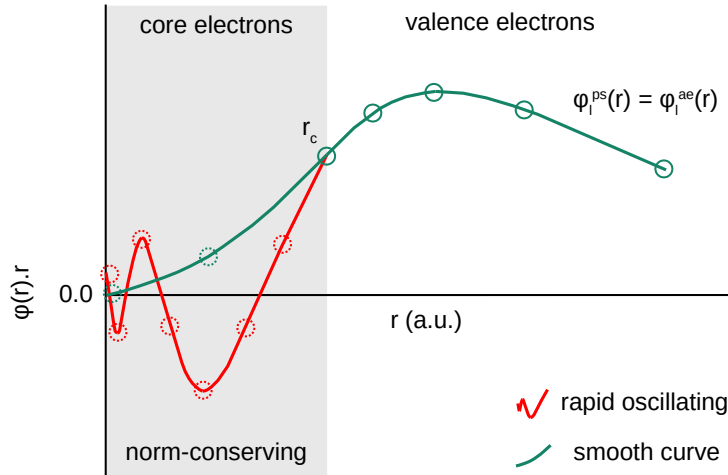
Figure 3.2 - We substitute the rapid oscillating all-electron wavefunction, in red, by a smoother pseudo wavefunction, in green, keeping their norms identical. After a considered radius, r_c, both wavefunctions match precisely.

In this figure, the radial atomic wavefunctions of the electrons (red solid line) are plotted and pseudo (ps) wavefunction (green solid line). The core electrons demonstrate a rapid oscillating behavior. Hence, the amount of planewaves, represented by dashed circles, required to reproduce these curves is greater than that required for the pseudo wavefunction. Moreover, the pseudo wavefunction is smoother. Beyond a radius (r_c), both radial and pseudo wavefunctions coincide and demonstrate similar behavior. This is one of the proposals by Hamann, and it is given in Eq. 3.37. Another proposal is shown in Eq. 3.38, which states that in the core region, $r < r_c$, the norm of all-electron and pseudo radial wavefunctions must be conserved.

$$\phi_l^{\text{ps}}(r) = \phi_l^{\text{ae}}(r) \qquad \text{for} \quad r > r_c, \tag{3.37}$$

$$\int_{r<r_c} dr\, r^2 |\phi_l^{\text{ps}}(r)|^2 = \int_{r<r_c} dr\, r^2 |\phi_l^{\text{ae}}(r)|^2. \tag{3.38}$$

Therefore, norm-conserving pseudopotential can be added as a subroutine to any DFT program.

Blöchl proposed an expanded concept of pseudopotential in his work about the projector augmented-wave (PAW) method [61]. PAW is an all-electron method that provides the complete wavefunction information and deals efficiently with first-row and transition-metal elements. It is considered to be an improvement over the norm-conserving *ab initio* pseudopotential, which is computationally less efficient than PAW and other pseudopotentials methods, like ultrasoft pseudopotential. In this thesis, transition metals are a constituent of the materials, PAW approach would be utilized for majority of the calculations, except for those not implemented for PAW, e.g., absorption calculation via epsilon.x code.

3.5 Equilibrium structures of materials

As presented in the previous chapter, the crystal structure play an essential role in the properties of the materials since the symmetry determines, for example, the allowed states by light absorption. Through x-ray diffraction and subsequent refinement, it is possible to build a crystallographic information file (CIF) containing the positions of the atoms within a cell of the required material. This information is the starting point for any DFT software. However, modifications, i.e., substitution and defects are usually inevitable, and their CIF might not be available. Hence, the equilibrium structures of these new materials need to be determined. Below we will briefly introduce the steps encoded within the DFT software, especially QE, used to obtain the optimized atomic position given the ionic coordinates of an unrelaxed structure.

We begin with the many-body Schrödinger equation similar to Eq. 3.1, but in this case, we take into consideration their complete form, as illustrated in [52]

$$
\left[-\sum_i \frac{\nabla_i^2}{2} - \sum_I \frac{\nabla_I^2}{2M_I} - \sum_{i,I} \frac{Z_I}{|\mathbf{r}_i - \mathbf{R}_I|} + \frac{1}{2}\sum_{i \neq j} \frac{1}{|\mathbf{r}_i - \mathbf{r}_j|} + \frac{1}{2}\sum_{I \neq J} \frac{Z_I Z_J}{|\mathbf{R}_I - \mathbf{R}_J|} \right] \Psi = E_{\text{tot}}\Psi, \quad (3.39)
$$

with M_I, R_I, Z_I, being the mass, position, and charge of the nuclei I, respectively, and r_i, the position of the electron. The atomic position is the nuclei position and we intend to compute the optimized nuclei coordinates. Hence, we must ensure that the forces on the nuclei are zero or close to zero in numerical calculations. So, based on the discrepancy between the ratio of kinetic and potential energy from nuclei and electrons in their equilibrium configuration, the total wavefunction, Ψ, can be written as a product of its individual wavefunctions as follows:

$$
\Psi(\mathbf{r}_1, ..., \mathbf{r}_N, \mathbf{R}_1, ..., \mathbf{R}_M) = \Psi_R(\mathbf{r}_1, ..., \mathbf{r}_N)\chi(\mathbf{R}_1, ..., \mathbf{R}_M), \quad (3.40)
$$

where Ψ_R (χ) depends only on electrons (nuclear) coordinates. This simplification allows us to obtain the many-body Schrödinger equation for the nuclei alone, as shown below:

$$
\left[-\sum_I \frac{\nabla_I^2}{2M_I} + \frac{1}{2}\sum_{I \neq J} \frac{Z_I Z_J}{|\mathbf{R}_I - \mathbf{R}_J|} + E(\mathbf{R}_1, ..., \mathbf{R}_M) \right] \chi = E_{\text{tot}}\chi. \quad (3.41)
$$

In this equation, $E(\mathbf{R}_1, ..., \mathbf{R}_M)$ corresponds to an effective potential due to the electronic energy at a fixed nuclear position. So, we can interpret Eq. 3.41 as a sum of nuclear Coulomb repulsion and the total energy of the electrons. The decoupling process seen in Eq. 3.40 that permitted obtaining the nuclear wavefunction of the system, is known as Born-Oppenheimer approximation, or adiabatic approximation, where the nucleus is considered to be moving so slowly that, from initial to final ground state, the electrons do not exchange energy with the nuclei.

Rearranging Eq. 3.41 in a compact form, we obtain

$$\hat{H}_n = -\sum_I \frac{\nabla_I^2}{2M_I} + U(\mathbf{R}_1, ..., \mathbf{R}_M), \tag{3.42}$$

and the total energy of the nuclei to be:

$$U(\mathbf{R}_1, ..., \mathbf{R}_M) = \frac{1}{2}\sum_{I \neq J} \frac{Z_I Z_J}{|\mathbf{R}_I - \mathbf{R}_J|} + E(\mathbf{R}_1, ..., \mathbf{R}_M). \tag{3.43}$$

We assume that, classically, the wavefunction of the nuclei has a highly localized character, i.e., the nucleus behaves like a point particle. Thus, the force acting on the nucleus is given by:

$$\mathbf{F}_I = -\frac{\partial U}{\partial \mathbf{R}_I}. \tag{3.44}$$

The above derivative is of impractical use concerning a system with many electrons, because of its dependence on 3M nuclear degrees of freedom. One practical solution, is to replace the derivative of an eigenvalue of the Hamiltonian by the expectation value of the derivative of the Hamiltonian which was proposed by Hellmann and Feynman [62]. So, the equation only depends on the density:

$$\mathbf{F}_I = Z_I \left[\int d\mathbf{r}\, n(\mathbf{r}) \frac{\mathbf{r} - \mathbf{R}_I}{|\mathbf{r} - \mathbf{R}_I|^3} - \sum_{J \neq I} Z_J \frac{\mathbf{R}_J - \mathbf{R}_I}{|\mathbf{R}_J - \mathbf{R}_I|^3} \right]. \tag{3.45}$$

The procedure briefly presented above is known as the Hellmann-Feynman theorem and is of great importance for finding the equilibrium structures. The numerical steps used by *ab-initio* software are summarized in Fig. 3.3. The minimization algorithm consists of evaluating the ground state energy and density. Then, using the Hellmann-Feynman theorem, one evaluates the force on each nucleus and compares it to a tolerance value, typically close to zero. If this value is greater than tolerance, the minimization of U is performed by using the Broyden-Fletcher-Goldfarb-Shanno [63] (BFGS) method, which is the default choice in QE for ionic dynamics optimization. The BFGS algorithm is a second-order quasi-newton method for finding the minima in non-linear functions.

3.6   Hubbard correction

One essential property of insulating and semiconductor materials is their gap. This quantity is often used as an essential parameter to indicate the quality of the theoretical calculations. Sometimes, these results are not in accordance with the experimental values and other computational corrections, e.g., other pseudopotential and functionals needs to be considered for better estimations. In materials composed of atoms from the *d* and *f* wave, the above ap-
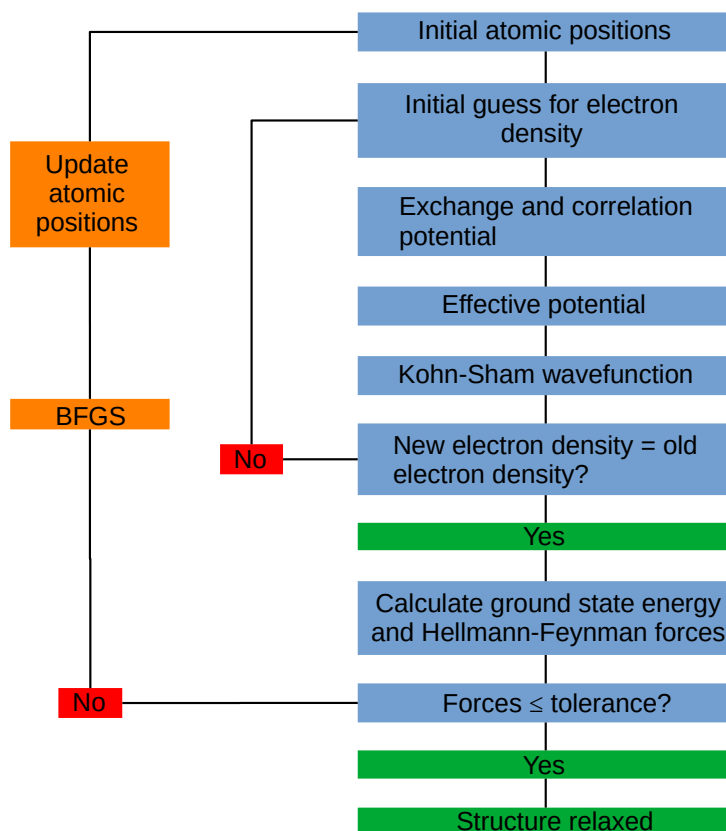
Figure 3.3 - Simplified scheme for BFGS structure optimization process used in QE. The blue boxes are related to standard SCF calculations, and the orange boxes are to minimization of the potential energy function, which gives the new positions of the atoms.

proaches might not be sufficient to correct the gap due to the strong correlation among these electrons. Then, another method needs to be considered to account for the localized d, f, and in some exceptional cases, the p electrons. This approach is known as the Hubbard correction, or often seen in the literature, as LDA+U. The work of Xiang *et al.* [64] contemplating hydrogen production, within a massive sample of compounds has shown the importance of using Hubbard to describe those compounds accurately.

The general form of the Hubbard correction energy is:

$$E_{DFT+U} = E_{DFT} + E_U, \qquad (3.46)$$

where E_{DFT} is the ground-state energy from self-consistent calculations, and E_U is the Hubbard corrective energy, which can be adjusted via experimental results in a semi-empirical way. However, experimental measurements are not always available for adjustment for most new materials. Thus, an *ab initio* method is required to overcome this problem. One of the most straightforward method to compute the Hubbard energy U is based on the linear-response constrained DFT (LR-cDFT) proposed by Cococcioni and Gironcoli [65], which reproduced quite good electronic properties results in metals and transition metals oxides (TMO). However, it is necessary to construct supercells so that periodic images of the perturbed on-site terms are not

affected, leading to a high computational cost.

In QE, the Hubbard parameter is provided by the HP code developed by Timrov and co-workers [66], which, in principle, is equivalent to the formulation of Cococcioni and Gironcoli. However, the actual code uses the reciprocal space formulation of density functional perturbation theory (DFPT) instead of DFT only. The DFPT has some advantages, since its formulation permits us to substitute an isolated perturbation in a supercell with a sum of individual perturbations in its primitive unit cell. Moreover, each perturbation can be computed individually and in a parallel framework, reducing the computational efforts drastically, and is more precise in the obtained data. The details could be found in HP code in the paper by Timrov *et al.* [67]. The main essence of the above method will be discussed briefly below.

As in the linear-response approach, the Hubbard U correction energy is given by the difference of the bare, χ_0^{-1}, and screened, χ^{-1}. The inverse response matrix is given by:

$$U^{\mathrm{I}} = (\chi_0^{-1} - \chi^{-1})_{\mathrm{II}}, \qquad (3.47)$$

where I is the atomic site index, and II indicates that we are considering only the diagonal terms. The key behind recasting monochromatic perturbations lies in the fact that we can rewrite the reciprocal lattice vector of the supercell ($\mathbf{G}$) as a sum of the reciprocal lattice vectors for the primitive unit cell ($\mathbf{g}$), and the vectors residing inside the first Brillouin zone of the primitive unit cell ($\mathbf{q}$), as follows:

$$\mathbf{G}_{klm} = \mathbf{g}_{k'l'm'} + \mathbf{q}_{\bar{k}\bar{l}\bar{m}}, \qquad (3.48)$$

$$\mathbf{g}_{k'l'm'} = k'\mathbf{b}_1 + l'\mathbf{b}_2 + m'\mathbf{b}_3, \qquad (3.49)$$

$$\mathbf{q}_{\bar{k}\bar{l}\bar{m}} = \frac{\bar{k}}{L_1}\mathbf{b}_1 + \frac{\bar{l}}{L_2}\mathbf{b}_2 + \frac{\bar{m}}{L_3}\mathbf{b}_3, \qquad (3.50)$$

where the subscripts are related to integers k, l, m of the reciprocal vectors of the supercell. In the monochromatic perturbation in DFPT formulation, the linear-response occupation matrix, χ (χ^0, similarly), can be written as

$$\frac{dn_{m_1 m_2}^{sl\sigma}}{d\lambda^{s'l'}} = \frac{1}{N_{\mathbf{q}}} \sum_{\mathbf{q}}^{N_{\mathbf{q}}} e^{i\mathbf{q}\cdot(\mathbf{R}_l - \mathbf{R}_{l'})} \Delta_{\mathbf{q}}^{s'} \bar{n}_{m_1 m_2}^{s\sigma} \qquad (3.51)$$

with λ being the strength of the perturbation, $N_{\mathbf{q}}$ is the number of $\mathbf{q}$ points, $\mathbf{R}$ is related to Bravais lattice vector. $\Delta_{\mathbf{q}}^{s'} \bar{n}_{m_1 m_2}^{s\sigma}$ is the lattice-periodic response of the atomic occupation to a monochromatic perturbation of wave vector $\mathbf{q}$, given by:

$$\Delta_{\mathbf{q}}^{s'} \bar{n}_{m_1 m_2}^{s\sigma} = \frac{1}{N_{\mathbf{k}}} \sum_{\mathbf{k}}^{N_{\mathbf{k}}} \sum_{v}^{N_{\mathrm{occ}}} \left[\left\langle \bar{u}_{v\mathbf{k}\sigma}^{\circ} | \hat{P}_{m_2,m_1,\mathbf{k},\mathbf{k}+\mathbf{q}}^{s} | \Delta_{\mathbf{q}}^{s'} \bar{u}_{v\mathbf{k}\sigma} \right\rangle + \left\langle \bar{u}_{v\mathbf{k}\sigma}^{\circ} | \hat{P}_{m_1,m_2,\mathbf{k},\mathbf{k}+\mathbf{q}}^{s} | \Delta_{\mathbf{q}}^{s'} \bar{u}_{v\mathbf{k}\sigma} \right\rangle \right], \quad (3.52)$$

where, N_{occ} and $N_{\mathbf{k}}$ are the numbers of occupied states and the points to sample the first Brillouin zone in the primitive unit cell, respectively; the superscript $^\circ$ indicates the quantities in the unperturbed ground state of the system, as $\bar{u}^\circ_{\nu\mathbf{k}\sigma}$ being the lattice-periodic part of the ground-state of the Kohn-Sham equation, $\hat{P}^s_{m_2,m_1,\mathbf{k},\mathbf{k}+\mathbf{q}}$ is the lattice-periodic projector operator, and $\Delta^{s'}_{\mathbf{q}}\bar{u}_{\nu\mathbf{k}\sigma}$ is the linear-response Kohn-Sham, that can be obtained by solving:

$$(\hat{\bar{H}}^\circ_{\mathbf{k}+\mathbf{q},\sigma} + \alpha\hat{\bar{\mathscr{O}}}_{\mathbf{k}+\mathbf{q},\sigma} - \varepsilon^\circ_{\nu\mathbf{k}\sigma})|\Delta^{s'}_{\mathbf{q}}\bar{u}_{\nu\mathbf{k}\sigma}\rangle = -\hat{\bar{\mathscr{P}}}_{\mathbf{k}+\mathbf{q},\sigma}(\Delta^{s'}_{\mathbf{q}}\hat{\bar{V}}_{\text{Hxc},\sigma} + \hat{V}^{s'}_{\text{pert},\mathbf{k}+\mathbf{q},\mathbf{k}})|\bar{u}^\circ_{\nu\mathbf{k}\sigma}\rangle. \quad (3.53)$$

The above equation depends on several terms that are explicitly shown in Ref. [67]. Then, the Hubbard parameters are given by solving the Eqs. 3.53, 3.52 and 3.51, and substituting into Eq. 3.47.

3.7   Band structures and density of states

The physical properties of materials depends strongly on the electronic structure. In order to compute the properties of the materials using DFT, all calculations must be done in crystals, i.e., a system with discrete translational invariance to obtain the band structures. This implies that we can use the Bloch theorem, and all the calculations can be restricted to a single unit cell. So, using Bloch's theorem,

$$\phi_i(\mathbf{r}) \to \phi_{i\mathbf{k}}(\mathbf{r}) = e^{i\mathbf{k}\cdot\mathbf{r}}u_{i\mathbf{k}}(\mathbf{r}), \quad (3.54)$$

means that any Kohn-Sham wavefunction, $\phi_i(\mathbf{r})$, can be written as the product of a planewave and a function with the same periodicity as the direct lattice. Then, applying the above relation into the Eq. 3.9, we achieved the Kohn-Sham equations expressed in Bloch basis [52],

$$\left[-\frac{1}{2}(\nabla + i\mathbf{k})^2 + V_{\text{tot}}(\mathbf{r})\right]u_{i\mathbf{k}}(\mathbf{r}) = \varepsilon_{i\mathbf{k}}u_{i\mathbf{k}}(\mathbf{r}), \quad (3.55)$$

where $\mathbf{k}$ is a wave vector belonging to the first Brillouin zone (BZ), V_{tot} is the effective potential, and $u_{\mathbf{k}}(\mathbf{r})$ are lattice-periodic functions. For each given $\mathbf{k}$, we will get a set of $\varepsilon_i(\mathbf{k})$, which is known as the dispersion relation.

Regarding obtaining the band structure of the desired material, one has to calculate the eigenvalues of the equation (3.55) for a specific set of values of $\mathbf{k}$. In particular, we want to construct a path in $\mathbf{k}$ space which connects all the high symmetry points of the Brillouin zone, and then calculate $\varepsilon_{\mathbf{k}}$ for this path.

The density of electronic states (DOS) is obtained from the dispersion relationship $\varepsilon(\mathbf{k})$ using the formula

$$\rho(E) = \sum_i \int_{\text{BZ}} \frac{d\mathbf{k}}{\Omega_{\text{BZ}}} \delta(E - \varepsilon_{i\mathbf{k}}), \quad (3.56)$$

and can be evaluated after acquiring the correct self-consistent potential and charge density.

3.8 Optical properties

Optical properties such as the absorption coefficient, reflection, and refractive index are experimental measurements that characterize the materials. These coefficients can be evaluated indirectly by employing the epsilon.x program [68], a post-processing code embedded within QE software, which provides the real and imaginary parts of the dielectric tensor through the eigenvalues and eigenvectors stored via SCF calculations. The imaginary part of the dielectric tensor as a function of frequency is given as follows:

$$
\begin{aligned}
\varepsilon_{2_{\alpha,\beta}}(\omega) \quad = \quad & \frac{4\pi e^2}{\Omega N_{\mathbf{k}} m^2} \sum_{n,\mathbf{k}} \frac{df(E_{\mathbf{k},n})}{dE_{\mathbf{k},n}} \frac{\eta\,\omega \hat{\mathbf{M}}_{\alpha,\beta}}{\omega^4 + \eta^2 \omega^2} + \\
+ \quad & \frac{8\pi e^2}{\Omega N_{\mathbf{k}} m^2} \sum_{n\neq n'} \sum_{\mathbf{k}} \frac{\hat{\mathbf{M}}_{\alpha,\beta}}{E_{\mathbf{k},n'} - E_{\mathbf{k},n}} \frac{\Gamma\omega f(E_{\mathbf{k},n})}{[(\omega_{\mathbf{k},n'} - \omega_{\mathbf{k},n})^2 - \omega^2]^2 + \Gamma^2 \omega^2},
\end{aligned}
\tag{3.57}
$$

where Ω is the volume of the lattice cell, n (n') belongs to valence (conduction) bands, $f(E_{\mathbf{k},n})$ is the Fermi distribution with $E_{\mathbf{k},n}$ being the eigenvalues of the Hamiltonian. The real part comes from the Kramers-Kronig transformation and is given by

$$
\begin{aligned}
\varepsilon_{1_{\alpha,\beta}}(\omega) \quad = \quad & 1 + \frac{2}{\pi} \int_0^\infty \frac{\omega' \varepsilon_{2_{\alpha,\beta}}(\omega')}{\omega'^2 - \omega^2} d\omega' \\
= \quad & 1 - \frac{4\pi e^2}{\Omega N_{\mathbf{k}} m^2} \sum_{n,\mathbf{k}} \frac{df(E_{\mathbf{k},n})}{dE_{\mathbf{k},n}} \frac{\omega^2 \hat{\mathbf{M}}_{\alpha,\beta}}{\omega^4 + \eta^2 \omega^2} + \\
+ \quad & \frac{8\pi e^2}{\Omega N_{\mathbf{k}} m^2} \sum_{n\neq n'} \sum_{\mathbf{k}} \frac{\hat{\mathbf{M}}_{\alpha,\beta}}{E_{\mathbf{k},n'} - E_{\mathbf{k},n}} \frac{[(\omega_{\mathbf{k},n'} - \omega_{\mathbf{k},n})^2 - \omega^2] f(E_{\mathbf{k},n})}{[(\omega_{\mathbf{k},n'} - \omega_{\mathbf{k},n})^2 - \omega^2]^2 + \Gamma^2 \omega^2},
\end{aligned}
\tag{3.58}
$$

where η and Γ are the adjustable intra and intersmear parameter, respectively, and $\hat{\mathbf{M}}_{\alpha,\beta}$ are the square matrix elements defined as:

$$
\begin{aligned}
\hat{\mathbf{M}}_{\alpha,\beta} \quad = \quad & \langle u_{\mathbf{k},n'} | \hat{\mathbf{p}}_\alpha | u_{\mathbf{k},n} \rangle \langle u_{\mathbf{k},n} | \hat{\mathbf{p}}_\beta^\dagger | u_{\mathbf{k},n'} \rangle \\
\propto \quad & u_{\mathbf{k},n'}^*(\mathbf{r}) \frac{d}{dx_\alpha} u_{\mathbf{k},n}(\mathbf{r}) u_{\mathbf{k},n}^*(\mathbf{r}) \frac{d}{dx_\beta} u_{\mathbf{k},n'}(\mathbf{r}),
\end{aligned}
\tag{3.59}
$$

and $|u_{\mathbf{k},n}\rangle$ is the term multiplying the plane wave in the single particle Bloch function extracted from SCF calculations, and $\mathbf{p}_\alpha$ is the electric dipole.

The absorption and refraction of a material can be characterized by the complex refractive index, given by:

$$
\tilde{n}_{\alpha,\beta}(\omega) = n_{\alpha,\beta}(\omega) + i\kappa_{\alpha,\beta}(\omega),
\tag{3.60}
$$

with $\tilde{n}$ being the complex refractive index, n, the real part, and κ, the extinction coefficient, which is related to the absorption coefficient α, through [69]:

$$\alpha_{\alpha,\beta} = \frac{2\kappa_{\alpha,\beta}(\omega)\omega}{c}. \tag{3.61}$$

The numerical data obtained from Eq. 3.57 and Eq. 3.58 permits us to calculate the index of refraction and the extinction coefficients via the following equations:

$$n_{\alpha,\beta}(\omega) = \frac{1}{\sqrt{2}}\left(\varepsilon_{1_{\alpha,\beta}}(\omega) + (\varepsilon_{1_{\alpha,\beta}}(\omega)^2 + \varepsilon_{2_{\alpha,\beta}}(\omega)^2)^{1/2}\right)^{1/2}, \tag{3.62}$$

$$\kappa_{\alpha,\beta}(\omega) = \frac{1}{\sqrt{2}}\left(-\varepsilon_{1_{\alpha,\beta}}(\omega) + (\varepsilon_{1_{\alpha,\beta}}(\omega)^2 + \varepsilon_{2_{\alpha,\beta}}(\omega)^2)^{1/2}\right)^{1/2}. \tag{3.63}$$

The reflectivity spectra can be evaluated through the relation between the reflected and normal incident light

$$R_{\alpha,\beta}(\omega) = \left|\frac{\tilde{n}_{\alpha,\beta(\omega)} - 1}{\tilde{n}_{\alpha,\beta(\omega)} + 1}\right|^2 = \frac{(n_{\alpha,\beta}(\omega) - 1)^2 + \kappa_{\alpha,\beta}(\omega)^2}{(n_{\alpha,\beta}(\omega) + 1)^2 + \kappa_{\alpha,\beta}(\omega)^2}. \tag{3.64}$$

3.9 Mechanical and thermal properties

Elastic constants are essential for understanding how materials respond to applied forces. In physics, elasticity is the ability of a material to deform under applied stress and then return to its original shape when the load is removed. Elastic constants are the coefficients in the stress-strain equations, which allow us to predict the effects of external forces on a material, e.g., bulk and shear modulus. The stress-strain relationship is described by the stress and the strain tensors, which are functions of the elastic constants. The stress tensor, σ, describes the relationship between force and stress, while the strain tensor, ε, describes the relationship between strain and deformation. The elastic constants are used to calculate the stress and strain tensors and to predict the materials behavior under certain load conditions. In the limit of small strain, the stress tensor is proportional to the strain

$$\sigma_l = \sum_{ij} C_{i,j}\varepsilon_l, \tag{3.65}$$

where $C_{i,j}$ is the tensor of elastic constants given by:

$$C_{i,j} = \frac{\partial \sigma_i}{\partial \varepsilon_j}\bigg|_{\varepsilon=0} = \frac{1}{V}\frac{\partial^2 U}{\partial \varepsilon_i \partial \varepsilon_j}\bigg|_{\varepsilon=0}, \tag{3.66}$$

with

$$U = \frac{V}{2}\sum_{i,j} \varepsilon_i C_{i,j}\varepsilon_j. \tag{3.67}$$

This will produce a quadratic relation to strain, and a quadratic fitting can be used to determine the elastic constants.

In this work, we have used thermo_pw [70] package to calculate the elastic tensor. The package also provides the mechanical properties based on Voigt-Reuss-Hill approximation (VRH) [71], which is the average value of the calculated module by Voigt [72] and Reuss [73]. We evaluated the mechanical properties related to all molybdates, with and without vacancy, such as the bulk modulus (B), Young's modulus (E), shear modulus (G), and Poisson's ratio (v). The Voigt equations consist in the derivation of bulk (B_V) and shear modulus (G_V) from elastic stiffness constants C_{ij}, as is presented in the below equations:

$$
\begin{aligned}
B_V &= \frac{1}{9}\left((C_{11}+C_{22}+C_{33})+2(C_{12}+C_{23}+C_{31})\right) \\
G_V &= \frac{1}{15}\left((C_{11}+C_{22}+C_{33})-(C_{12}+C_{23}+C_{31})+\right. \\
&\qquad \left. 3(C_{44}+C_{55}+C_{66})\right).
\end{aligned}
\tag{3.68}
$$

The bulk and the shear moduli can also be obtained from the Reuss formalism:

$$
\begin{aligned}
1/B_R &= \frac{1}{9}\left((S_{11}+S_{22}+S_{33})+2(S_{12}+S_{23}+S_{31})\right) \\
1/G_R &= \frac{1}{15}\left(4(S_{11}+S_{22}+S_{33})-4(S_{12}+S_{23}+S_{31})+\right. \\
&\qquad \left. 3(S_{44}+S_{55}+S_{66})\right),
\end{aligned}
\tag{3.69}
$$

where S_{ij} are the compliance tensor components, B_R (G_R) the bulk (shear) modulus. In the Voigt-Reuss-Hill approximation (VRH), the stiffness module is given by the equations:

$$
B_H = \frac{B_V+B_R}{2}
\tag{3.70}
$$

$$
G_H = \frac{G_V+G_R}{2}.
\tag{3.71}
$$

From the above results, we can obtain the Poisson ratio (v) and Young modulus (E), which are given by:

$$
v = \frac{1}{2}\frac{3B_H-2G_H}{3B_H+G_H}
\tag{3.72}
$$

$$
E_H = \frac{9B_HG_H}{3B_H+G_H}.
\tag{3.73}
$$

Also, from the knowledge of the mechanical properties previously calculated, it is possible to estimate if the material is ductile or brittle through the Pugh's ratio [74] B/G. Values of B/G greater (less) than 1.75 defines the material to be ductile (brittle). Hardness is described as the capability of a material to resist deformation. In a polycrystalline material, the hard-

ness is correlated to shear and bulk modulus, given by a modification of Vickers hardness (H_v) expression proposed by Chen *et al.* [75] designated by

$$H_v = 2(G_H^3/B_H^2)^{0.585} - 3. \tag{3.74}$$

The Debye temperature is associated with the mechanical properties according to Anderson [76] and can be written as:

$$\Theta_D = \frac{h}{k_B}\left(\frac{n}{4\pi}\frac{N_A\rho}{M}\right)^{1/2}\bar{v}_m \tag{3.75}$$

where h is the Planck constant, k_B is the Boltzmann constant, N_A is Avogadro's number, n is the number of atoms per formula unit, ρ is the material density, M is the molecular weight, and $\bar{v}_m$ is the average sound velocity, which is given by:

$$\bar{v}_m = \left(\frac{1}{3}\left[\frac{2}{v_t^3} + \frac{1}{v_l^3}\right]\right)^{-1/3}, \tag{3.76}$$

with v_t and v_l being the transverse and longitudinal velocities, respectively, given as a function of the mechanical parameters B_H and G_H, i.e., $v_t = \sqrt{G_H/\rho}$ and $v_l = \sqrt{(3B_H+4G_H)/3\rho}$.

3.10   Thermoelectric properties

The Boltzmann equation has been widely used to investigate the transport properties in metals and semiconductors. The electrical current density **J** and the heat current density $\mathbf{J}_Q$ can be written in terms of the three coefficients: electrical conductivity σ, the Seebeck coefficient **S**, and thermal conductivity **K** [50]:

$$\mathbf{J} = \sigma(\mathbf{E} - \mathbf{S}\nabla T) \tag{3.77}$$

$$\mathbf{J}_Q = T\sigma\mathbf{S}\mathbf{E} - \mathbf{K}\nabla T, \tag{3.78}$$

where the coefficients are tensors to accomplish all directions. Rearranging Eq. 3.77 and substituting into Eq. 3.78, we found

$$\sigma\mathbf{E} = \mathbf{J} + \sigma\mathbf{S}\nabla T$$

$$\mathbf{J}_Q = T\mathbf{S}(\mathbf{J} + \sigma\mathbf{S}\nabla T) - \mathbf{K}\nabla T$$

$$\mathbf{J}_Q = T\mathbf{S}\mathbf{J} - \kappa_e\nabla T, \tag{3.79}$$

where

$$\kappa_e = \mathbf{K} - \mathbf{S}\sigma\mathbf{S}T \tag{3.80}$$

is the electron contribution to thermal conductivity. These quantities depend on the temperature and the value of the chemical potential μ [77]

$$[\sigma]_{ij}(\mu,T) = e^2 \int_{-\infty}^{+\infty} d\varepsilon \left(-\frac{\partial f(\varepsilon,\mu,T)}{\partial \varepsilon} \right) \sum_{ij}(\varepsilon), \qquad (3.81)$$

$$[\sigma S]_{ij}(\mu,T) = \frac{e}{T} \int_{-\infty}^{+\infty} d\varepsilon \left(-\frac{\partial f(\varepsilon,\mu,T)}{\partial \varepsilon} \right) (\varepsilon - \mu) \sum_{ij}(\varepsilon), \qquad (3.82)$$

$$[\mathbf{K}]_{ij}(\mu,T) = \frac{1}{T} \int_{-\infty}^{+\infty} d\varepsilon \left(-\frac{\partial f(\varepsilon,\mu,T)}{\partial \varepsilon} \right) (\varepsilon - \mu)^2 \sum_{ij}(\varepsilon), \qquad (3.83)$$

with $f(\varepsilon,\mu,T)$ denoting the Fermi-Dirac distribution function

$$f(\varepsilon,\mu,T) = \frac{1}{e^{(\varepsilon-\mu)/K_B T} + 1}, \qquad (3.84)$$

and

$$\sum_{ij}(\varepsilon) = \frac{1}{V} \sum_{n,\mathbf{k}} v_i(n,\mathbf{k}) v_j(n,\mathbf{k}) \tau(n,\mathbf{k}) \delta(\varepsilon - E_{n,k}) \qquad (3.85)$$

is the Transport Distribution Function tensor, composed by the total volume (V), $E_{n,\mathbf{k}}$ is the energy of the n-th band at $\mathbf{k}$, $v_i(n,\mathbf{k})$ is the ith component of the band velocity, δ is the Dirac's delta function transport lifetime (τ) or relaxation time, and in this work, it will be considered as a constant.

As a metric of usability of thermoelectric materials, we can use a relation that accounts for the conductivity, the Seebeck coefficient and thermal conductivity, given by the sum of the electronic (κ_e) and lattice (κ_l) thermal conductivities. This quantity is called the figure of merit Z_T. Z_T is defined by

$$ZT = \frac{\sigma S^2}{\kappa_e + \kappa_l} T. \qquad (3.86)$$

One way to increase the figure of merit is to reduce thermal conductivity. Materials with low thermal conductivity are of interest for thermoelectric devices, and thermal barrier coating [78]. Clarke [79] proposes an equation that estimates the minimum of thermal conductivity as follows:

$$\kappa_{\min} = 0.87 k_B \left(\frac{M}{n N_A} \right)^{-2/3} E_H^{1/2} \rho^{1/6}. \qquad (3.87)$$

While electronic thermal conductivity can be computed via Eq. 3.80, the lattice contribution of this equation requires another approach. In this work, we have used the equation formulated by Slack [80] for nonmetallic solids. In a crystal with n atoms per unit cell:

$$\kappa_l = A \cdot \frac{\bar{M} \Theta_D^3 \delta}{\gamma^2 T n^{2/3}}, \qquad (3.88)$$

where $\bar{M}$ is the average mass of an atom in the crystal, δ^3 is the volume per atom, Θ_D is the Debye temperature given by Eq. 3.75, γ is the Grüneisen constant, which can be evaluated in terms of Poisson's coefficient as described by [81, 82]

$$\gamma = \frac{3(1+v)}{2(2-3v)}. \tag{3.89}$$

The remaining term is the constant A [83]

$$A = \frac{2.43 \cdot 10^{-6}}{1 - 0.514/\gamma + 0.228/\gamma^2}. \tag{3.90}$$

3.10.1 Klemens theory of lattice thermal conductivity

When point defects are introduced into the crystal lattice, they scatter the phonons and become more challenging to the heat flow. The κ_l proposed by Slack does not account for this effect. Thus, we have used a theory by Klemens [84] in order to accomplish the oxygen vacancies in our materials. The lattice thermal conductivity is given by

$$\kappa = \frac{1}{3} \int S(\omega)v^2\tau(\omega)d\omega, \tag{3.91}$$

where $S(\omega)d\omega$ is the specific heat per unit volume due to lattice modes of frequency ω, v is the velocity of the lattice waves, and $\tau(\omega)$ their effective relaxation time. For phonons scattered by point defects

$$\frac{1}{\tau'} = A\omega^4. \tag{3.92}$$

At high temperatures, the intrinsic resistance is due to anharmonic phonon process which does not conserve the total wavevector, called U processes. The inverse relaxation time is of the form

$$\frac{1}{\tau_u} = B\omega^2. \tag{3.93}$$

If the scattering by the defect is mainly given by the difference of mass, the parameter A found in Eq. 3.92 is given by:

$$A = \frac{a^3}{4\pi v^3}\varepsilon, \tag{3.94}$$

where a^3 is the atomic volume and

$$\varepsilon = \frac{\sum_i c_i(M_i - M)^2}{M^2} \tag{3.95}$$

$$M = \sum_i c_i M_i, \tag{3.96}$$

with c_i being the concentration of the *i*-atoms and M_i the mass of i-atoms. Including the point defect scattering and U processes, we can write

$$\tau(\omega) = \frac{\tau' \tau_u}{(\tau' + \tau_u)}. \tag{3.97}$$

Substituting Eq. 3.97 into Eq. 3.91, we find the specific heat at high temperatures

$$S(\omega) = \frac{3k_b}{2\pi^2} \frac{\omega^2}{v^3}. \tag{3.98}$$

Performing the substitution of Eq. 3.97 and Eq. 3.98 in Eq. 3.91:

$$\kappa = \frac{1}{3} \int_0^{\omega_D} \frac{3k_b}{2\pi^2} \frac{\omega^2 v^2 \tau' \tau_u}{v^3 (\tau' + \tau_u)} d\omega$$

$$\kappa = \frac{k_b}{2\pi^2 v} \int_0^{\omega_D} \omega^2 \frac{\tau' \tau_u}{(\tau' + \tau_u)} d\omega. \tag{3.99}$$

It is possible to rewrite $\tau' \tau_u / (\tau' + \tau_u)$ as:

$$\frac{\tau' \tau_u}{(\tau' + \tau_u)} = \frac{1}{AB\omega^6} \frac{AB\omega^6}{B\omega^2 + A\omega^4} = \frac{1}{B\omega^2 + A\omega^2} = \frac{1}{B\omega^2} = \frac{1}{B\omega^2 \left(1 + A\frac{\omega^2}{B}\right)}. \tag{3.100}$$

Substituting Eq. 3.100 in Eq. 3.99:

$$\kappa = \frac{k_b}{2\pi^2 vB} \int_0^{\omega_D} \frac{d\omega}{1 + A\frac{\omega^2}{B}} \tag{3.101}$$

$$\kappa = \frac{k_b}{2\pi^2 vB} \omega_0 \tan^{-1} \frac{\omega_D}{\omega_0}, \tag{3.102}$$

where $\omega_0 = \sqrt{\frac{B}{A}}$.

Thermal conductivity in the lack of point defects makes Eq. 3.93 transform into:

$$\tau_u = \frac{1}{B\omega^2} = \tau(\omega).$$

Substituting the above equation in Eq. 3.91,

$$\kappa_0 = \frac{1}{3} \int \frac{3k_b}{2\pi^2} \frac{\omega^2}{v^3} \frac{v^2}{B\omega^2} d\omega$$

$$\kappa_0 = \frac{k_b}{2\pi^2 vB} \int_0^{\omega_D} d\omega = \frac{k_b}{2\pi^2 v} \frac{\omega_D}{B}. \tag{3.103}$$

Dividing Eq. 3.102 by Eq. 3.103

$$\frac{\kappa}{\kappa_0} = \frac{\tan^{-1}(u)}{u} \tag{3.104}$$

where $\omega_D/\omega_0 = u$. In terms of constants A and B, $u = \omega_D \frac{\sqrt{A}}{\sqrt{B}}$, therefore, $u^2 = \omega_D \frac{A}{B}$. Constant B can be taken from Eq. 3.103, thus, u^2:

$$u^2 = \omega_D^2 A \frac{2\pi^2 v \kappa_0}{\omega_D \kappa} = \frac{2\pi^2 A v \omega_D \kappa_0}{\kappa}. \tag{3.105}$$

From Eqs. 3.94, 3.95 and 3.96, we can express the constant A as:

$$A = \frac{a^3}{4\pi v^3} \frac{\sum_i c_i (M_i - M)^2}{M^2}. \tag{3.106}$$

Putting this equation into Eq. 3.105:

$$u^2 = \frac{2\pi^2 v \omega_D \kappa_0}{\kappa} \frac{a^3}{4\pi v^3} \frac{\sum_i c_i (M_i - M)^2}{M^2}$$

$$u^2 = \frac{\pi a^3}{2k_b} \frac{\omega_D \kappa_0}{v^2} \frac{\sum_i c_i (M_i - M)^2}{M^2}.$$

Defining $\Gamma = \frac{\sum_i c_i (M_i - M)^2}{M^2}$,

$$u^2 = \frac{\pi a^3}{2k_b} \frac{\omega_D \kappa_0 \Gamma}{v^2}. \tag{3.107}$$

From the relation $\hbar\omega_D = k_b \Theta_D$, it is possible to substitute ω_D in equation 3.107, resulting:

$$u^2 = \frac{\pi a^3}{2k_b} \frac{2\pi k_b \Theta_D}{h} \frac{\kappa_0 \Gamma}{v^2}$$

$$u^2 = \frac{\pi^2 a^3 \Theta_D \kappa_0 \Gamma}{h v^2}. \tag{3.108}$$

Finally, the lattice thermal conductivity is given by:

$$\kappa = \kappa_0 \frac{\tan^{-1}(u)}{u} \tag{3.109}$$

MOLIBDATES DESCRIPTION AND COMPUTATIONAL DETAILS

This chapter will detail the general structure of molybdates and the computational steps taken to obtain the appropriate inputs to perform the required properties calculations.

4.1 General information about molybdates

The molybdates of the form $AMoO_4$ (where A = Ba, Sr, Ca and Pb) are materials from the scheelite-type family, belonging to the space group $I4_1/a$ and point group symmetry C_{4h}^6 [7, 85, 86]. The conventional cell is composed of four formula units, that is, four Ba, four Mo, and sixteen O, with a total of twenty-four atoms. Each Mo is bonded to four O atoms, defining a slightly distorted tetrahedral cluster $[MoO_4]$ of T_d symmetry, with four faces, as is shown in Fig. 4.1 a). Each Ba is bonded to eight O atoms in covalent character, forming a deltahedral complex $[AO_8]$ of symmetry D_{2d}, with twelve faces, Fig. 4.1 b). In Fig. 4.1 c), we see the junction of these structures forming a scheelite. In scheelite, each oxygen bonded to the central metal (lattice former) atom is also shared by two lattice modifier atoms, e.g., Ba.
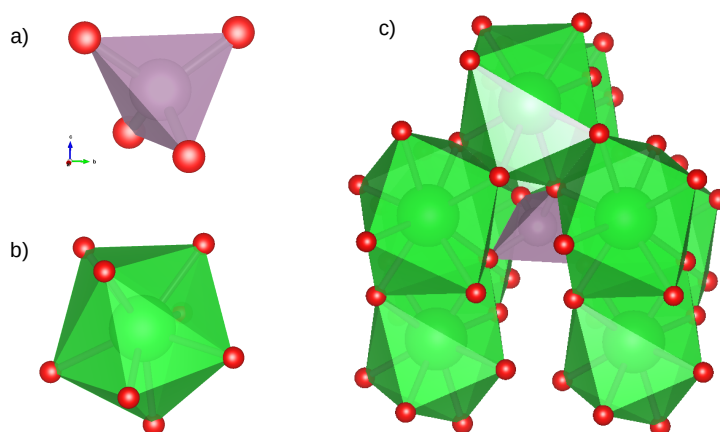
Figure 4.1 - General scheelite structure. In a), we see the tetrahedral complex formed by the $[MoO_4]$ cluster; in b), the deltahedral complex $[BaO_8]$ and, in c), the complete molybdate.

Accordingly to the Lewis theory, the electronic configuration of $BaMoO_4$, which can be extended to the other molybdates, consists of one Ba = $[Xe]6s^2$, one Mo = $[Kr]4d^5 5s^1$, and four

$O = [He]2s^2 2p^4$. That means the Ba (oxidation state +2) donates its two valence electrons to two oxygen (each O has oxidation state -2), and this oxygen guarantees its stability by receiving the other two electrons given by the central Mo (oxidation state +6) atom. The two remaining oxygen receives two electrons each from Mo, turning the Mo into a d^0 ionic metal and, the formula unit, electrically neutral. The Lewis structure is shown below in Fig. 4.2.
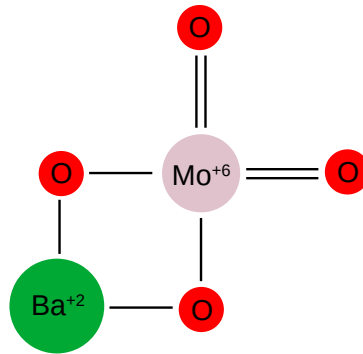
Figure 4.2 - Lewis structure of molybdates.

4.2 Technical details

An essential part of own theoretical calculation is to achieve the optimal structural parameters, since the electronic ground state properties depend on its values, and a poorly optimized input may lead to spurious results. The workflow of this thesis is presented below:

Initial parameters	Optimzation	Calculated properties	
CIF	ecut	band structure	IR-spectrum**
vacancy test*	ecut rho	PDOS	optical properties
vc-relax	kpoints	charge density	Mehcanical and thermal properties
Hubbard	smearing*	Kohn-Sham orbitals	transport properties
vc-relax	lattice		
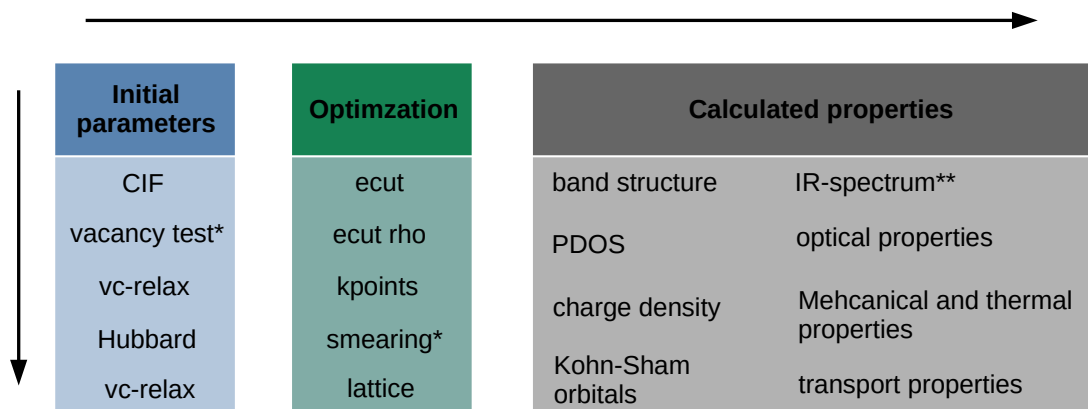
Figure 4.3 - Proceeded workflow. The steps marked as * are only presented in vacancy cases, and ** are not presented in vacancy cases. The arrows indicate the order of the utilized calculations.

Thus, from Fig. 4.3, the starting point was to obtain the CIF so that the initial coordinates of the atoms forming the structure of interest could be used. For barium and strontium molybdates, we used the CIF provided by Nogueira *et al.* [7]; for calcium and lead molybdate we used the CIF provided by Hazen *et al.* [87], and Lugli *et al.* [88], respectively. The calculations presented in the workflow were carried out using the QUANTUM ESPRESSO package

(QE) [89,90] utilizing DFT. The PAW method, developed by Blöchl [61], was used to represent the valence and core electrons, whereas the electron exchange-correlation interactions were described by the Perdew-Burke-Ernzerhof (PBE) functional [59]. All pseudopotentials used are from the Pslibrary v1.0.0 [91]. The next step is to develop a cell-free optimization upon the data extracted from CIFs. In this case, the lattice parameters and atomic positions were fully relaxed using the BFGS algorithm, with residual force and convergence threshold converged to 0.001 Ry/Bohr and 10^{-4} Ry, respectively, which is the standard value. In general, all calculations are spin-polarized and all adjustable required parameters were chosen as the default.

An optimization procedure aims to guarantee the stability of the obtained results. It benefits hardware usage since the optimal resources are chosen based on a rigid convergence test. The adopted parameters are summarized in Table 4.1, and all convergence tests are presented ranging from Appendix B.3-B.10 and Table B.1. While the cutoff energies vary a few among the materials, integration over the Brillouin zone remains the same using a $4 \times 4 \times 2$ Monkhorst-Pack [95] k-mesh for a conventional cell in both cases, with and without vacancies. Due to technical reasons, in order to investigate magnetism in vacancy materials, the usage of a smearing function was necessary.

Table 4.1 - Summary of all used optimized input quantities.

Material	Ecut (Ry)	Ecut rho (Ry)	Kpoints	Smearing type	Degauss (eV)
$BaMoO_4$	110	440	$4 \times 4 \times 2$	-	-
$BaMoO_4 - V_O^\times$	110	440	$4 \times 4 \times 2$	mv	0.02
$SrMoO_4$	100	400	$4 \times 4 \times 2$	-	-
$SrMoO_4 - V_O^\times$	100	400	$4 \times 4 \times 2$	mv	0.02
$CaMoO_4$	130	520	$4 \times 4 \times 2$	-	-
$CaMoO_4 - V_O^\times$	100	400	$4 \times 4 \times 2$	mv	0.02
$PbMoO_4$	120	480	$4 \times 4 \times 2$	-	-
$PbMoO_4 - V_O^\times$	120	480	$4 \times 4 \times 2$	mv	0.02

An oxygen vacancy in $AMoO_4$, was introduced in a unit cell of the pristine compound by removing one oxygen atom and then performing the geometry optimization. Assuming that each class of atoms is indistinguishable in pristine $AMoO_4$, that is, the choice of vacancy is arbitrary, we removed one neutral oxygen, described as $V_O^\times$, following the Kröger-Vink notation [92]. This procedure is reasonable since, from the ground state energy calculation (see Appendix B.1) we observed that, regardless of oxygen position around the Mo atom, with reasonable accuracy, its vacancy produces the same energy value.

DFPT calculations of Hubbard parameters, were performed using the uniform $\mathbf{q}$ point mesh of size $2 \times 2 \times 2$ alongside the 'ortho-atomic' Hubbard projector. These calculations demanded a very high computational cost. The calculated U values for all considered atoms and

Table 4.2 - Hubbard parameters obtained via DFPT encoded in hp.x for all structures.

Material	Atomic type	Hubbard (eV)
$BaMoO_4$	Mo	3.6
$BaMoO_4 - V_O^\times$	Mo	3.0
	O	9.0
	O1	8.0
$SrMoO_4$	Mo	3.9
$SrMoO_4 - V_O^\times$	Mo	3.4
	O	9.0
	O1	8.4
$CaMoO_4$	Mo	3.7
$CaMoO_4 - V_O^\times$	Mo	3.7
	O	9.2
	O1	8.8
	O2	7.9
$PbMoO_4$	Mo	3.7
$PbMoO_4 - V_O^\times$	Mo	3.9
	O	8.0

materials are shown in Table 4.2. Since, in some cases, the hp.x code provided distinct U values for oxygen, we have grouped the similar ones and labeled them following the values obtained as they play a different roles in electronic properties. For $PbMoO_4$-$V_0^\times$, the difference was nearly 0.1 eV among all oxygen atoms. Hence, all oxygen were considered to be of the same type. Regarding the Hubbard correction U_p for oxygen $2p$ orbital, its importance has been reported on several metal oxides materials, in which the U_d alone for d orbital does not reproduce with precision the band gap in semiconductors. Recently, K. J. May and A. M. Kolpak [93] presented an extensive study on self-consistent calculation of U_d and U_p for peroviskites $LaMO_3$ (M=V, Cr, Mn, Fe, CO, Ni). According to the authors, for these compounds, U_p calculated for oxygen $2p$ states ranges from around 4.8 to 7.6 eV, which are in qualitative agreement with the experimental U_p values obtained from x-ray spectroscopy. Besides, the DFT calculation of the band gaps also agrees with the experiment. Recent studies on TiO_2 [94] also applied the Hubbard parameter U_p for oxygen orbital $2p$ to reproduce the experimental energy gap. Considering the pristine materials from this work, oxygen Hubbard's corrections were unnecessary, as we will see in the next chapter.

After adding corrective Hubbard U values, a second cell-free optimization needs to be carried out as these interactions tend to modify the total energy. The resultant cells are presented in Fig. 4.4. In the upper row, Figs. 4.4 a)-d), we see the relaxed conventional cells for the pristine case composed of 24 atoms, in which the oxygen atom surrounded by a dashed circle will be removed. In order to take advantage of the crystallographic symmetry (that means less computational effort), one of the first tasks performed by pw.x (software responsible for
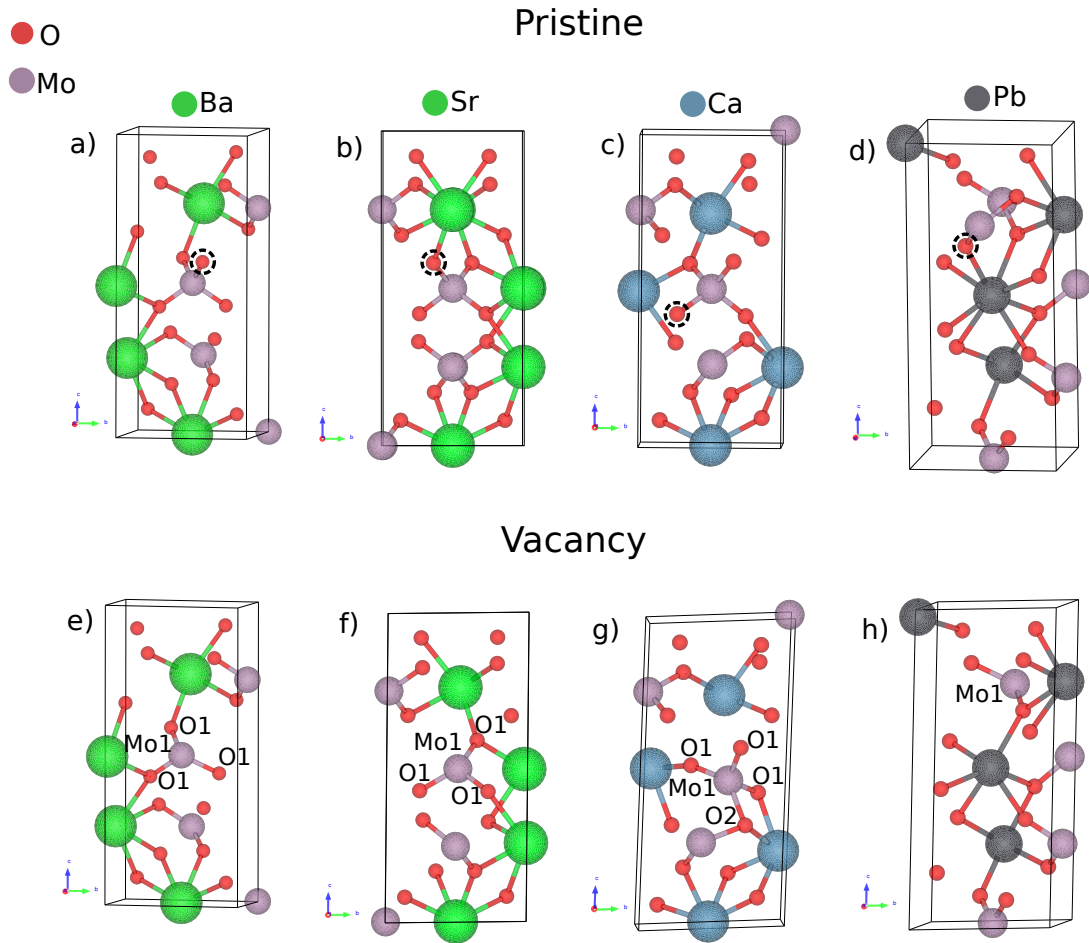
Figure 4.4 - Molybdates relaxed conventional cell description. The dashed circle marks the oxygen removed in the pristine row a)-d).

scf calculation) is to find the symmetry operations in the crystal. In all pristine cases, the cell-free optimized structure exhibit the same space and point group as found within experimental measurements. In the presence of the vacancy, as shown in Figs. e)-h), we observe that in $BaMoO_4 - V_O^\times$ and $SrMoO_4 - V_O^\times$, the $[MoO_4]$ cluster associated with vacancy becomes a trigonal $[MoO_3]$ structure, while in $CaMoO_4 - V_O^\times$ and $PbMoO_4 - V_O^\times$, there is a substantial deformation in the $[MoO_3]$ cluster, so that, during the optimization process, the rearrangement makes the trigonal structure return to one with coordination four. Table 4.3 details the lattice parameters characterizing each material.

From these crystallographic data, it is possible to observe that for pristine $AMoO_4$, the lattice vectors obtained from the relaxation process are slighting greater than the experimental values provided by their respective CIF, maintaining the same values of the crystallographic angles α, β, and γ. When one oxygen vacancy is introduced, we observe a similar behavior in $BaMoO_4 - V_O^\times$, $SrMoO_4 - V_O^\times$, and $PbMoO_4 - V_O^\times$, where lattice vector **a** (**c**) increases (decreases) when compared to that of the pristine structure. On the contrary, for $CaMoO_4 - V_O^\times$, **a** diminishes a little. However, all lattice vectors do not vary substantially from the original CIF. Considering the volume, vacancy materials have a smaller volume, with the exception of

Table 4.3 - Calculated cell parameters of $AMoO_4$ with and without oxygen vacancies and the comparison with the experimental data.

Structure	Cell parameters (Å)			Volume ($Å^3$)	Atomic mass (g/mol)	Density (g/cm^3)	Angle (°)		
	a	b	c				α	β	γ
$BaMoO_4$	5.660	5.660	12.984	415.946	1189.138	4.747	90.000	90.000	90.000
$BaMoO_4{}^a$	5.584	5.584	12.829	400.147	1189.138	4.934	90.000	90.000	90.000
$BaMoO_4 - V_O^\times$	5.675	5.661	12.643	406.168	1173.139	4.796	90.637	89.843	89.646
$SrMoO_4$	5.459	5.459	12.167	362.769	990.310	4.534	90.000	90.000	90.000
$SrMoO_4{}^a$	5.402	5.402	12.041	351.463	990.310	4.678	90.000	90.000	90.000
$SrMoO_4 - V_O^\times$	5.486	5.442	11.937	356.328	974.311	4.540	91.142	90.581	90.687
$CaMoO_4$	5.276	5.276	11.555	321.705	800.142	4.130	90.000	90.000	90.000
$CaMoO_4{}^b$	5.222	5.222	11.425	321.552	800.142	4.132	90.000	90.000	90.000
$CaMoO_4 - V_O^\times$	5.175	5.450	11.524	321.938	784.143	4.044	86.057	83.566	92.140
$PbMoO_4$	5.509	5.509	12.279	372.764	1468.630	6.542	90.000	90.000	90.000
$PbMoO_4{}^c$	5.434	5.434	12.107	357.500	1468.630	6.821	90.000	90.000	90.000
$PbMoO_4 - V_O^\times$	5.644	5.333	11.928	358.484	1452.631	6.728	87.510	90.697	87.786

[a] Ref. [7] (experiment).

[b] Ref. [87] (experiment).

[c] Ref. [88] (experiment).

$CaMoO_4 - V_O^\times$, keeping its volume nearly unaltered. In general, the lack of an oxygen atom reduces the cell parameters along the crystallographic direction [001], modifies their angles, and the crystal structure becomes triclinic instead of tetragonal body-centered for pristine $AMoO_4$.

Another interesting measurement used to characterize the materials is the bond length among the atoms within the unit cell. In this work, the compiled data of the average interatomic distances are shown in Table 4.4, and in a graphical way, in Appendix B.2. For pristine molybdates, the interatomic Mo-O is practically constant, whereas A-O is proportional to the atomic radius in the alkaline earth metals family (Ba, Sr and Ca). Defect average distances A-O and Mo-O are less affected than those who are directly bonded to vacancy Mo-O-$V_O^\times$, in which the distance are slightly lower than pristine $BaMoO_4$ and $SrMoO_4$, and bigger for $CaMoO_4$ and $PbMoO_4$.

To define the size of the supercell, we followed the methodology of reference [27], which calculated the formation energies of oxygen vacancy for the scheelite-type compound BiVO4, which has the same structure as $AMoO_4$. The authors verified that oxygen vacancy formation

Table 4.4 - Interatomic distances A-O and Mo-O in $AMoO_4$ (A=Ba, Sr, Ca and Pb) with and without oxygen vacancies.

Structure	Average interatomic distances (Å)			
	Ba	Sr	Ca	Pb
Pristine A-O	2.805	2.631	2.487	2.666
Pristine Mo-O	1.781	1.781	1.784	1.784
Defect A-O	2.779	2.610	2.441	2.622
Defect Mo-O	1.752	1.756	1.774	1.762
Defect Mo-O-$V_O^\times$	1.776	1.779	1.817	1.914

energy varies very little for $1 \times 1 \times 1$, $2 \times 1 \times 1$ and $2 \times 2 \times 1$ supercells, the reason by which we used a $1 \times 1 \times 1$ supercell. Thus, the formation energy (or cohesive energy) is given by [96]:

$$H_f^{AMoO_4} = E(AMoO_4) - \mu_A - \mu_{Mo} - 4\mu_O, \qquad (4.1)$$

where $E(AMoO_4)$ is the total energy of the pristine molybdate, μ_A, μ_{Mo}, and μ_O are the chemical potential of A, Mo, and O, which usually are equal to the DFT total energies. We have to remember that the supercell has four formula units. In Fig. 4.5, it is possible to see that all cases have negative values, which means that these structures are stable despite the vacancy breaking the symmetry.
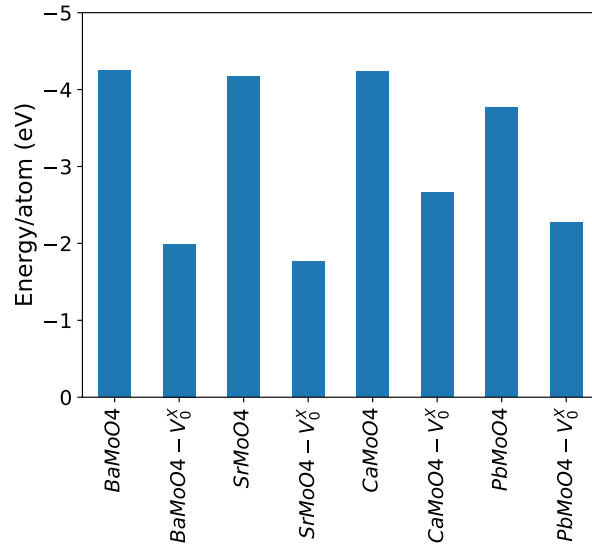
Figure 4.5 - Molybdates conventional cell description

The oxygen vacancy formation energy ΔE_v^o is calculated as in [96]:

$$\Delta E_v^o = E(A_4Mo_4O_{15}) + \mu_O - 4E(AMoO_4), \qquad (4.2)$$

where $E(A_4Mo_4O_{15})$ is the energy of $AMoO_4$ with vacancy, μ_o is the chemical potential of oxygen atom and $4E(AMoO_4)$ is the energy of the pristine $AMoO_4$ supercell. We obtained

$\Delta E_{\rm v}^{\rm O} \approx 3.0$ eV per oxygen atom, see Fig. 4.6, which is consistent with the results for $LaXO_3$ (X=Cr, Mn, Fe, Co, Ni) from [96].
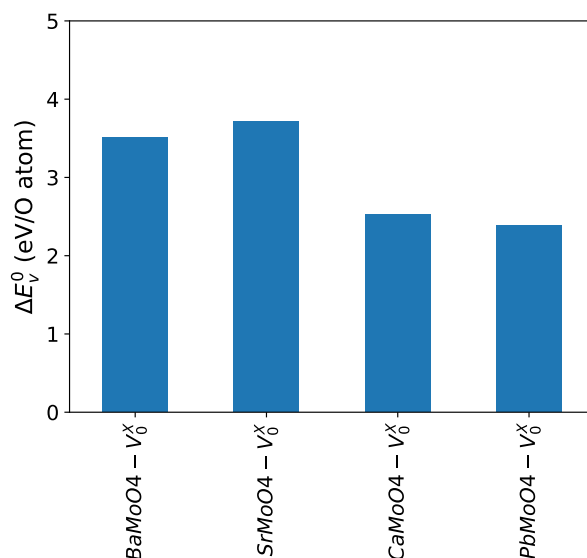
Figure 4.6 - Comparison of oxygen vacancy formation energy among all molybdates.

Carrying on the technical procedures, the epsilon.x program was utilized for optical properties calculations, e.g., absorption, reflection, and index of refraction spectrum since it allows the usage of spin-polarized and Hubbard in the same input. This program demands norm-conserving pseudopotential; thus, in Appendix E.1, we calculated all electronic properties using norm-conserving pseudopotential to verify its use without losing quantitative accuracy compared to PAW.

ELECTRONICS AND OPTICAL PROPERTIES OF MOLYBDATES

In this chapter, we will present the results obtained for $BaMoO_4$, $SrMoO_4$, $CaMoO_4$, and $PbMoO_4$ with and without vacancy, concerning electronic band spectrum, the projected density of states, charge density, orbitals, and how these results explain the induced magnetism presented in vacancy case. Furthermore, we also show the absorption, reflection, and refractive index spectrum for all materials. The infrared modes and dielectric constant are discussed for pristine only.

5.1   Electronic properties

The Mo and O atoms in $[MoO_4]^{2-}$ complex of pristine $AMoO_4$ have oxidation +6 and -2, respectively. In this case, Mo donates all its valence electrons to the four O atoms, leading empty the $4d$ and $5s$ orbitals. Hence, the complex $[MoO_4]^{2-}$ has no unpaired electrons, indicating that the pure crystal is nonmagnetic. When $V_O^\times$ is introduced in the form of a point defect into $AMoO_4$, in principle, two electrons will be trapped by Mo, which was originally bonded to O. However, the vacancy will modify the symmetry of $[MoO_4]^{2-}$ cluster as well as the whole crystal. Then, the order in which the $4d$ orbitals will be occupied depends on the crystal field splitting of this new configuration.

For a quantitative and qualitative analysis of the electronic properties, initially we have performed the calculation of the band structure in $AMoO_4$ with and without oxygen vacancy, as is shown in Fig. 5.1, where the zero in energy scale corresponds to the energy of the top of the valence band in pure molybdates, and its corresponding contribution in presence of the vacancy. In the left column of Fig. 5.1, we present the pristine $AMoO_4$ band structure. The chosen path $(\Gamma - X - M - \Gamma)$ used to perform the band structure follows the suggestions of Setyawan and Curtarolo for tetragonal lattice [?]. We observe that for pristine $BaMoO_4$, Fig. 5.1 a), both spin channels are degenerate with a direct gap of 4.08 eV at Γ point with S_4 symmetry. Similar behavior occur in $SrMoO_4$ and $CaMoO_4$ (with S_4 symmetry), is demonstrated in Figs. 5.1 b) and c), respectively. The gap energy diminishes and is found to be dependent on the atomic size of the lattice ion. The value are 3.77 eV in $SrMoO_4$, and 3.47 eV in $CaMoO_4$. Unlike the above compound, $PbMoO_4$ (Fig. 5.1 d)) exhibits an indirect gap of 2.99 eV at k with symmetry C_1,

which is reasonably smaller than that of $SrMoO_4$, although being a crystal with similar volume and cationic-oxygen distance. Generally, an insulating character can be attributed to materials in a) and b) and large semiconductors in c) and d).
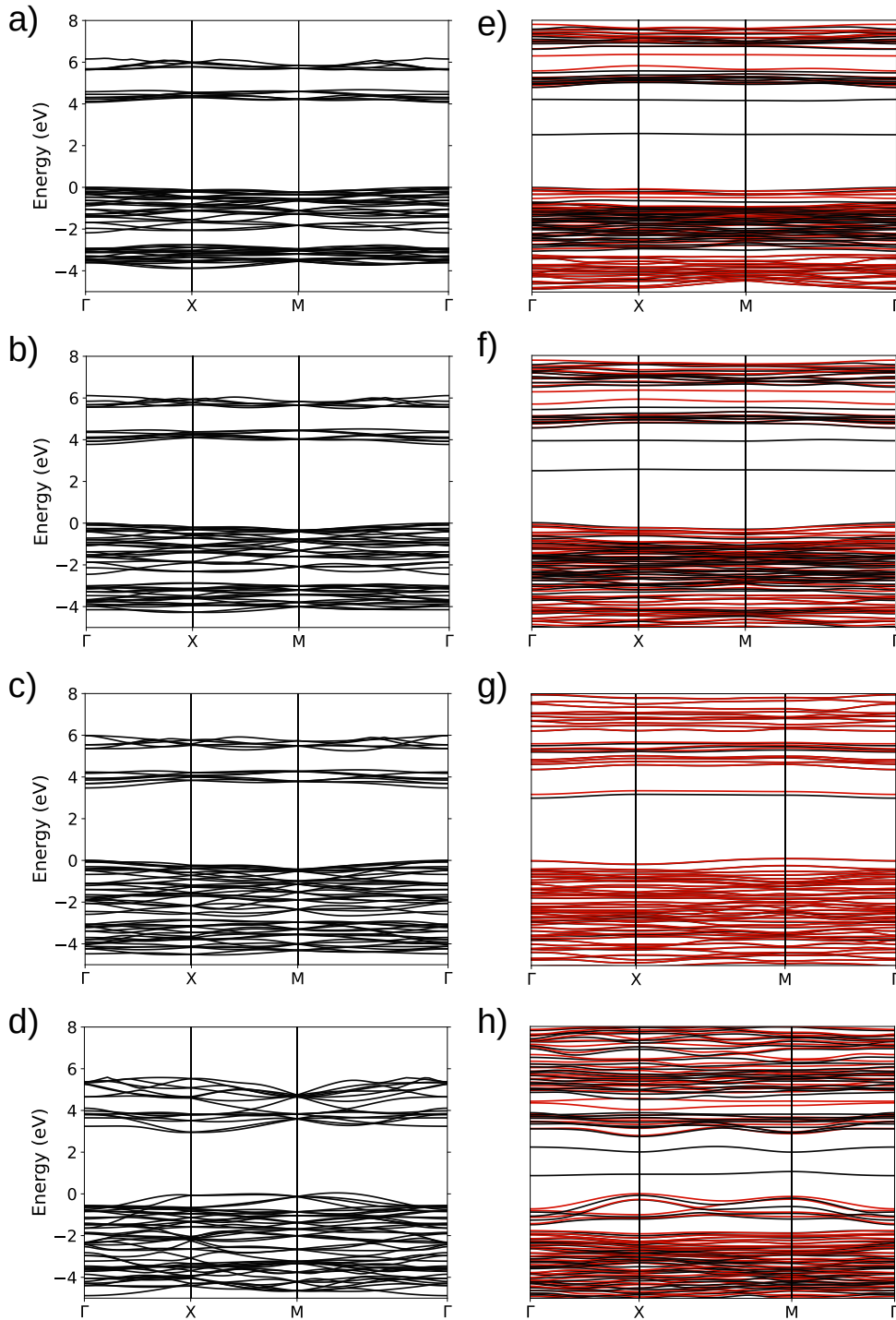
Figure 5.1 - Electronic band structures along the symmetry points of the Brillouin Zone ($\Gamma - X - M - \Gamma$) corresponding to the tetragonal body-centered lattice as indicated by Setyawan and Curtarolo [103]. For $AMoO_4$ without vacancy, a) - d), $BaMoO_4$, $SrMoO_4$, $CaMoO_4$, and $PbMoO_4$, respectively, the band spectrum presents a matching contribution to spin-up and down channels. When O is removed, e) - h), there are significant differences in the band structure related to its pristine crystal (left column), where spin-up (black line) and spin-down (red line) distinction are displayed.

When one neutral oxygen atom is removed from the MoO_4 complex, there are significant modifications in the electronic band structure of all molybdates, as presented in Figs. 5.1 e) - h). The same high-symmetry points in first Brillouin Zone are considered in order to compare them with that of the pristine cases. In Fig. 5.1 e), we show the electronic band structure for the spin-up channel (black line) and spin-down channel (red line) of $BaMoO_4$ in the presence of vacancies. In this case, two narrow bands in the spin-up channel are created inside the forbidden gap region. The first narrow band (from bottom to top) is at 2.58 eV, and the second at 4.21 eV above the valence band at the Γ point. Moreover, C_1 symmetry, are also found in all other vacancy materials. Therefore, $BaMoO_4 - V_0^\times$ is a semiconductor with a direct gap of 0.58 eV, which is considerably lower than the gap of pristine $BaMoO_4$ (4.08 eV). Since there is an asymmetry between the spin-up and the spin-down contributions, the material exhibits a net magnetization. For $SrMoO_4 - V_0^\times$, Fig. 5.1 f), the two narrow bands with spin-up are located at 2.55 eV and 3.98 eV above the top of valence bands, and that in the conduction band at 4.53 eV, resulting in an indirect gap of 0.55 eV. From crystallographic data, we observe that

Table 5.1 - Summarized electronic and magnetic properties of molybdates calculated via DFT and comparison with experimental measurements.

Material	Band gap (eV)	Experimental (eV)	Tot magnetization (μ_B)	Nature
$BaMoO_4$	4.07	4.08^a	0.00	direct
$BaMoO_4 - V_0^\times$	0.58		2.00	direct
$SrMoO_4$	3.77	3.81^b	0.00	direct
$SrMoO_4 - V_0^\times$	0.55		2.00	indirect
$CaMoO_4$	3.47	3.55^c	0.00	direct
$CaMoO_4 - V_0^\times$	1.01		0.15	indirect
$PbMoO_4$	2.99	3.07^a	0.00	direct
$PbMoO_4 - V_0^\times$	0.47		2.00	indirect

^{a} Ref. [1]
^{b} Ref. [97]
^{c} Ref. [98]
^{d} Ref. [99]

$BaMoO_4$-$V_0^\times$ is most resistant to cell parameters modifications. This can explain why the direct nature of the gap is retained only in this material. For $CaMoO_4$-$V_0^\times$, the energy bands in Fig. 5.1 g), is significantly different when compared to the other molybdates since, in this case, only one narrow band appears within the gap region. Both spin channels are practically identical, although the highest occupied state is located in the spin-down channel at 3.24 eV above the valence, providing a gap of 1.01 eV, the highest value calculated in the vacancy case. Unlike, $CaMoO_4$-$V_0^\times$, $PbMoO_4$-$V_0^\times$ has the lowest band gap of 0.47 eV in the spin-up channel, as seen in Fig. 5.1 h). This material also presents two narrow bands inside the forbidden energy gap in the spin-up channel, one at 1.14 eV above the valence band and another at 2.33 eV, with no intermediary states for the spin-down channel. Table 5.1 summarizes information on electronic

properties.

In Fig. 5.2 a) - d), we exhibit the results of the projected density of states (PDOS) for pristine $BaMoO_4$, $SrMoO_4$, $CaMoO_4$, and $PbMoO_4$, respectively. Due to a standard scheelite-like structure, all materials have a similar PDOS shape, where we observe that the main contribution to the valence bands comes from O $2p$ states and, for the conduction band, the contributions are predominantly from Mo $4d$ states in MoO_4 cluster (blue line) and antibonding O $2p$ states (black line). However, there is a difference in the PDOS of $PbMoO_4$ as their outermost shell is composed of $6p$ states, not a s state as in the others. Then, in the conduction band, we also see a relevant contribution from empty $6p$ states, whereas in the valence band, the Pb $6s$ mixes with O $2p$. Above the conduction band, with a gap of approximately 1 eV, there is another empty band formed essentially by of Mo $4d$ orbitals, O $2p$, Mo $5s$, and s-like orbitals from the alkaline earth metals. However, its contribution diminishes and is proportional to the atomic number. In $PbMoO_4$, this gap does not exist, being filled by Pb $6p$. The O $2p$ states in the valence band are composed of two degenerate $2p_y$ and $2p_x$ orbitals and a minor contribution from the $2pz$ orbital. In contrast, in the conduction band, almost 60% of the states originated from Mo $4d$, 19% from O $2p_z$, and minor contributions from the other orbitals. However, in $PbMoO_4$, Mo $4d$ orbital contribution shrink to 48%, and Pb $6p$ increases to 28%. The shape of the orbitals in pristine materials can be found in Fig. C.2.
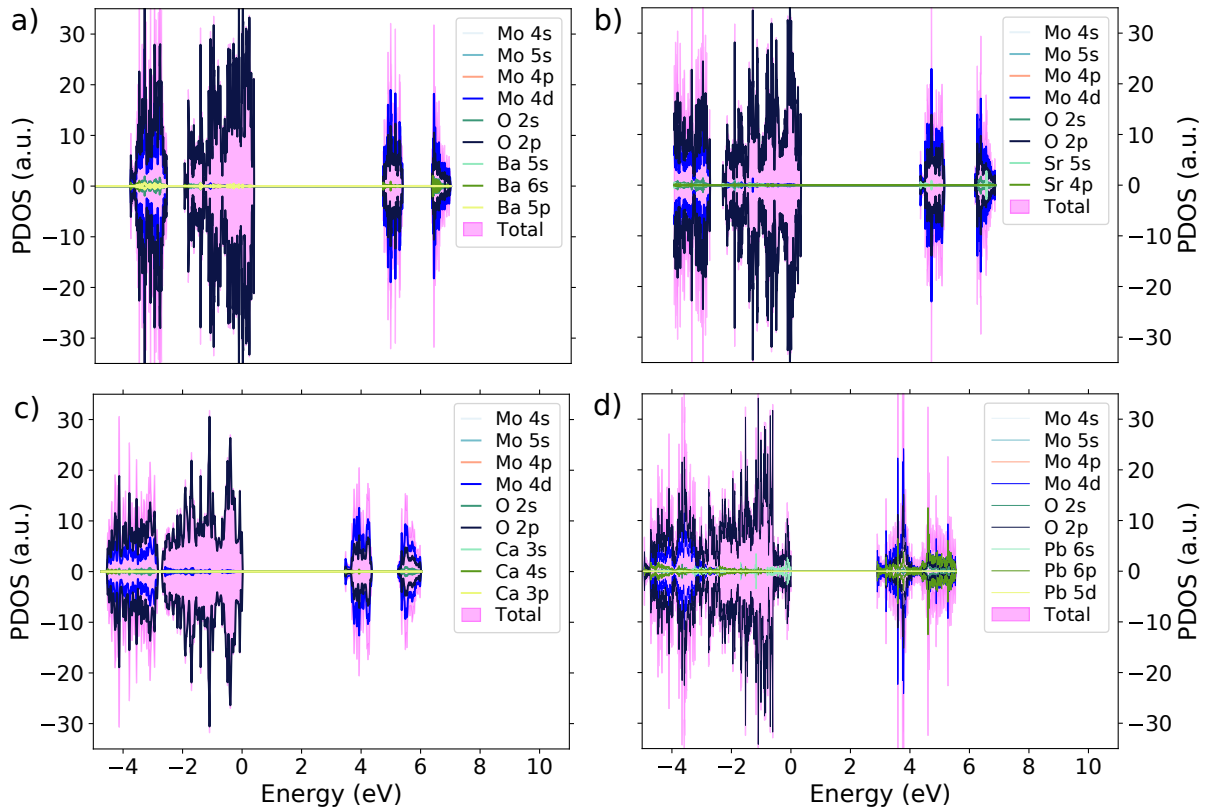
Figure 5.2 - Projected density of the main orbitals in pristine $BaMoO_4$, a), $SrMoO_4$, b), $CaMoO_4$, c), and $PbMoO_4$, d).

In order to check the crystal field in these materials, we have rearranged the *d* orbitals as a function of its symmetry. Although S_4 symmetry is found at valence and conduction bands (see Appendix C.1 for comparison), which is in accordance to Porto *et al.* [100], and Basiev *et al.* [101] studies on Raman spectroscopy of molybdates, this lower symmetry appears due to deformations of the scheelite structures due to the presence of $[MoO_4]^{-2}$ cluster. However, the use of T_d symmetry to represent the $[MoO_4]^{-2}$ cluster is widely adopted [13, 102, 103]. In Figs. 5.3 a) - d), we present the PDOS in terms of the calculated crystal field splitting for the tetragonal symmetry in $[MoO_4]^{2-}$ of BaMoO$_4$, SrMoO$_4$, CaMoO$_4$, and PbMoO$_4$, respectively. From CFT, we should expect the *e* states (d_{z^2} and $d_{x^2-y^2}$ orbitals) below the t$_2$ states (d_{zx}, d_{zy} and d_{xy}). Since *e* states are not towards the ligands, they feel lower Coulomb repulsion, leading to lower energies than the t_2 state, which is towards the ligands. The obtained results of all the materials agree with CFT. It is also observed that the spin-up and spin-down PDOS channels are symmetrical, resulting in null magnetization.
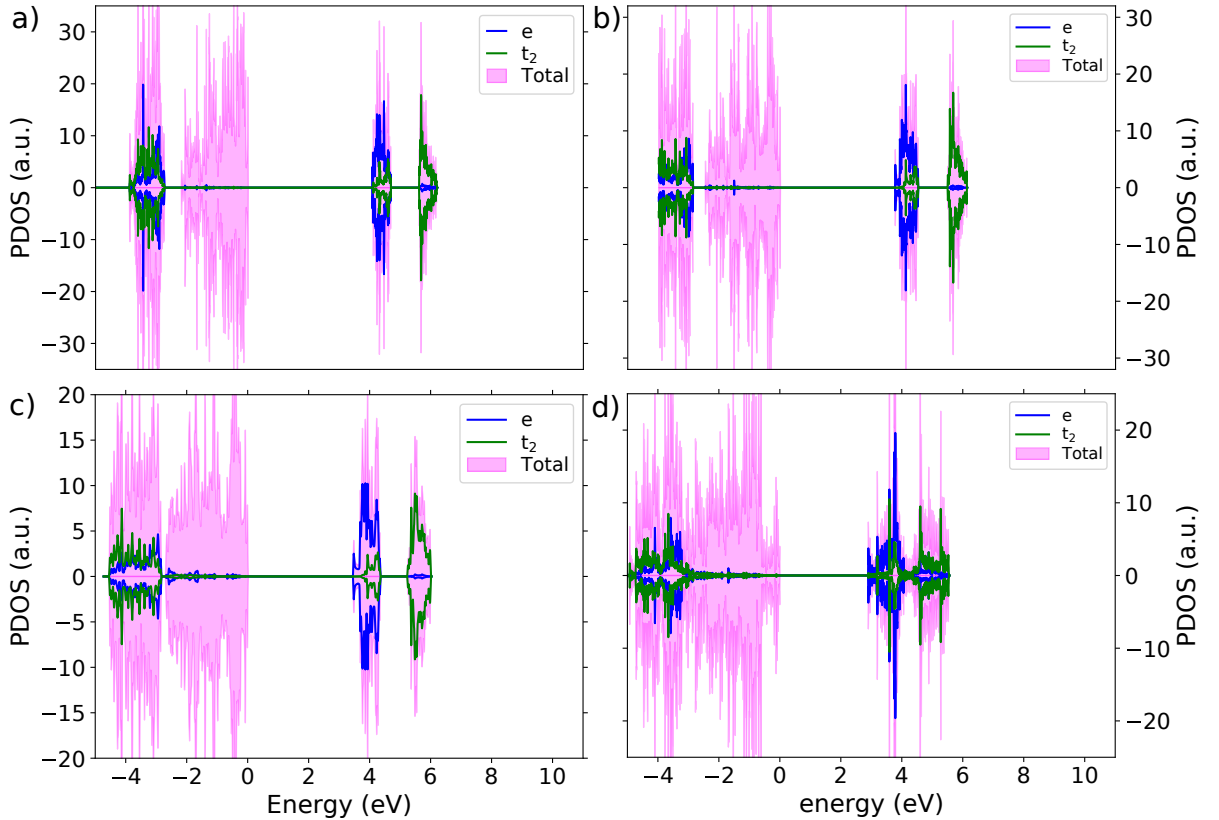
Figure 5.3 - Crystal field splitting considering T_d point group in pristine BaMoO$_4$, a), SrMoO$_4$, b), CaMoO$_4$, c), and PbMoO$_4$, d).

Unlike the pristine case, the removal of one oxygen atom from AMoO$_4$ breaks the symmetry of $[MoO_4]$ tetrahedra and $[AO_8]$ polyhedron, consequently changing the crystal point group to the lowest possible, C_1. These not only cause the appearance of new energy levels inside the forbidden band but mainly breaks the spin-up and down channels, resulting in a spin state with net magnetization ($n_\uparrow - n_\downarrow \neq 0$, Eq. 3.27). This behavior also appears in other ma-

terials, such as $ATiO_3$-$V_O^\times$ ($A = Mn, Ti, Fe$) [104]. In Fig. 5.4, we have plotted the PDOS of molybdates with one vacancy, and the Fermi level normalizes the energy axis. For $BaMoO_4$-$V_0^\times$ and $SrMoO_4$-$V_0^\times$, corresponding to Figs. 5.4 a) and b), we observe similar contributions from the orbitals. In these cases, the $[MoO_4]$ tetrahedron formed by Mo1 becomes $[MoO_3]$ trigonal. The contribution for the narrow bands inside the gap comes only from the spin-up component (upper side of each figure). We observe that the top of wide valence band states is composed mainly of O1 $2p$ orbitals. The states of the two narrow bands are as follows: a combination of 55% Mo1 $4d$ orbitals of MoO_3 cluster (red line), 22% of Mo1 $5s$ (light green line), and 10% of O1 $2p$ orbitals (black line) for a lower narrow band, and 58% of Mo1 $4d$, and 28% O1 $2p$ for the narrow upper band. This resulted in a magnetization of 2 μ_B per cell. Considering the conduction bands, it is predominantly given by empty states from the remaining $[MoO_4]$ tetra-hedron Mo $4d$ and O $2p$ orbitals. In $CaMoO_4$-$V_0^\times$, exhibited in Fig. 5.4 c), we see a significant
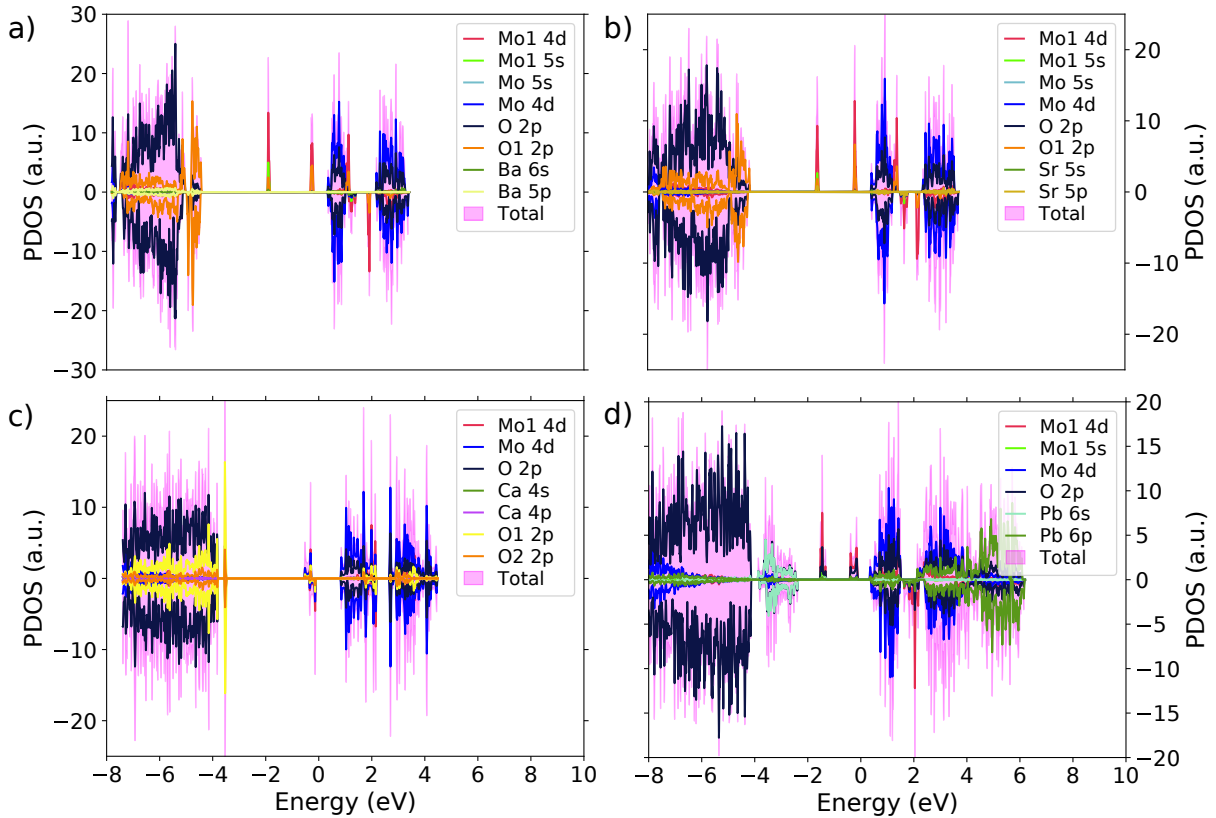
Figure 5.4 - Projected density of the main orbitals in $BaMoO_4$-$V_0^\times$, a), $SrMoO_4$-$V_0^\times$, b), $CaMoO_4$-$V_0^\times$, c), and $PbMoO_4$-$V_0^\times$, d).

difference in comparison to other molybdates, as there is only one narrow band inside the gap and both the spin channels contribute almost equally. However, this small discrepancy results in a total magnetization of 0.15 μ_B per cell. The states participating in narrow bands are composed of approximately 30% of Mo1 $4d$ hybridized with 20% of Mo $4d$, and 10% of O1 $2p$ and O2 $2p$ (see Fig. C.3 c)). The conduction bands follow the same composition as define when Mo $4d$ and O $2p$ are dominant. The PDOS of $PbMoO_4$-$V_0^\times$ is presented in Fig. 5.4 d). Compared to the O $2p$ predominance of the top of the wide valence band of the pristine case, the valence in

vacancy PbMoO$_4$ is composed of O $2p$ and Pb $6s$ in equal proportions. PbMoO$_4$-$V_0^\times$ has two narrow bands which are wider than the other cases. It leads to the total magnetization of 2 μ_B as in BaMoO$_4$-$V_0^\times$ and SrMoO$_4$-$V_0^\times$. The states and proportions forming these bands are similar to a) and b). Fig. C.3 exhibits the shape of the orbitals in defective materials.

Besides the tetragonal geometry of MoO$_4$ cluster, the vacancy $V_O^\times$ generates the trigonal geometry relative to MoO$_3$ cluster in BaMoO$_4$-$V_0^\times$ and SrMoO$_4$-$V_0^\times$, which is associated with the degenerate d_{xz} and d_{yz} orbitals, and non-degenerate d_{z^2}, d_{xy} and $d_{x^2-y^2}$ orbitals, with energies increasing in this order provided by its trigonal CF [105]. In BaMoO$_4$ and SrMoO$_4$ with vacancy, the lowest valence narrow band is composed mainly of 35% of Mo1 $4d_{xz}$ orbital, 8% of Mo1 $4d_{xy}$ and Mo1 $4d_{yz}$ orbitals, and the highest valence narrow band is composed of 50% of Mo1 $4dz^2$ and 8% of Mo1 $4d_{xy}$ orbitals. The $4d_{x^2-y^2}$ lies at the top of the conduction band. The above order of the orbital energies does not agree with what is expected for trigonal geometry. Therefore, the PDOS in terms of the crystal field orbitals of BaMoO$_4$ and SrMoO$_4$ with oxygen vacancy, follows the Abraham *et al.* nomenclature [106] applied to crystal field states of CaMoO$_4$ and PbWO$_4$ with oxygen vacancy and no Hubbard. They are them denoted by e', t'_2 and t''_2. In this nomenclature, $e'(t'_2)$ is a mixture of e and t_2 orbitals, with predominance of e (t_2) orbital, and t''_2 is a non-degenerate state composed only of t_2 orbital. The t''_2 (t'_2) orbital has the lowest (highest) energy and e' is the intermediate energy state. In Figs. 5.5 a) and b) we show the PDOS in terms of e and t_2 orbital for MoO$_4$ cluster and e', t'_2 and t''_2 for MoO$_3$ cluster. We observe that the lowest (highest) energy narrow band is composed mainly of $t''_2(e')$ orbital, and the t'_2 orbital lies inside the conduction band. It is interesting to notice that, for [MoO$_4$]$^{2-}$, the tetragonal crystal field splitting remains as in pristine material.

It is worth mentioning that, unlike Abraham *et al.* [106] where the threefold [MoO$_3$] appears in CaMoO$_4$-$V_0^\times$ and PbMoO$_4$-$V_0^\times$, the trigonal complex is not obtained. Hence, the crystal field scheme adopted in BaMoO$_4$-$V_0^\times$ and SrMoO$_4$-$V_0^\times$ is neither suitable for describing the states nor the magnetization in these cases due to fourfold [MoO$_4$] complex. In order to address tetragonal CF contribution, we plotted in Figs. 5.5 c) and d), the e (red line) and t_2 (black line) states from Mo1, and for CaMoO$_4$-$V_0^\times$ in Fig. 5.5 c), we observe that its CF splitting energy is not strong enough, so that we have low spin [MoO$_4$] complex, which benefits paired electrons. For PbMoO$_4$-$V_0^\times$ in Fig. 5.5 d), the difference in e-Mo1 and t_2-Mo1 splitting energy favors a high spin [MoO$_4$] complex, and leads to the observed magnetization.

In the interest of supporting the assumption that MoO$_3$ keeps two unpaired electrons from the oxygen vacancy, we calculate the net spin-charge density for all defective molybdates, which is presented in Fig. 5.6. In Fig. 5.6 a) for BaMoO$_4$-$V_0^\times$, the oxygen vacancy removes six O $2p$ states from the valence bands while removing only four valence electrons, leaving two extra electrons which can be held by MoO$_3$ complex [106]. The yellow region represents precisely this behavior, where the spin-up charge surface occupy the Mo1 atom and the $V_0^\times$
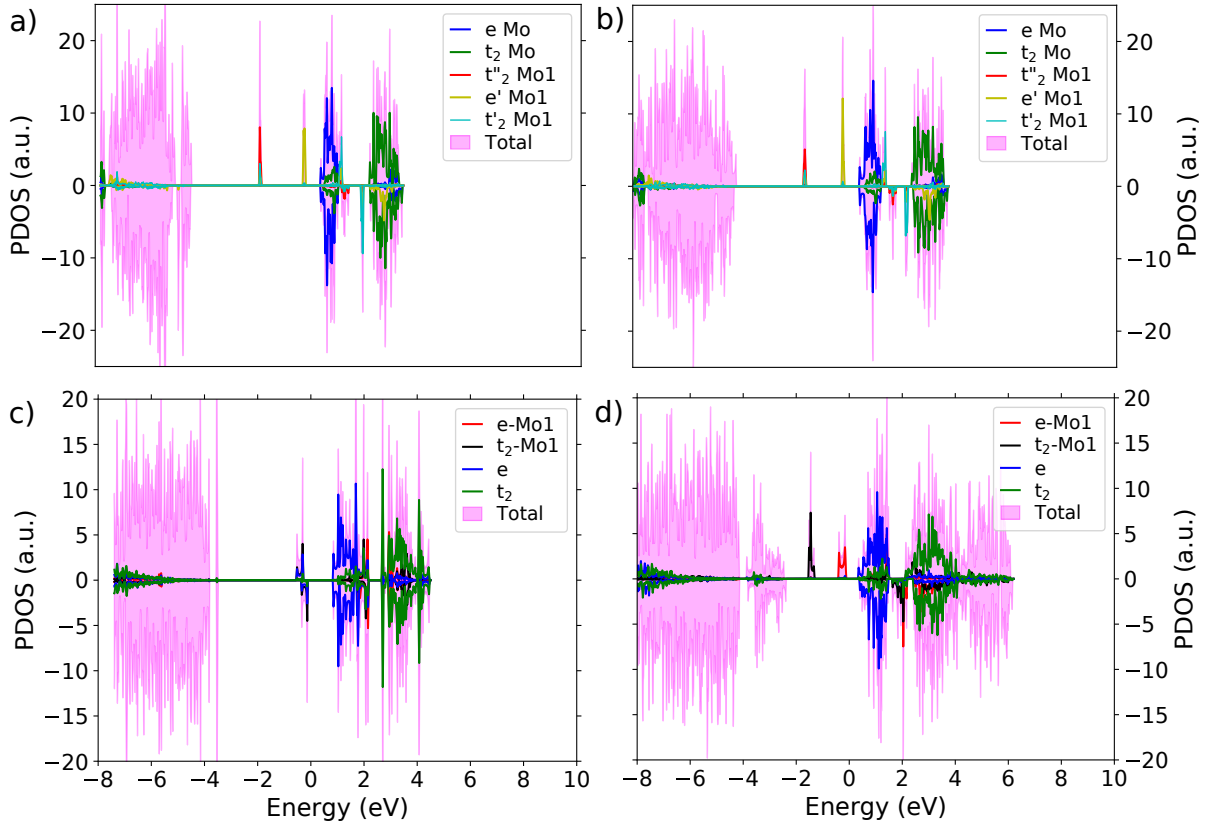
Figure 5.5 - Crystal field splitting considering Abraham *et al.* [113] in vacancy BaMoO$_4$, a), SrMoO$_4$, b), and T_d point group in CaMoO$_4$, c), and PbMoO$_4$, d).

region. In this case, the conventional cell presents a magnetization of 2.00 μ_B and Lowdin charges of 1.83e around Mo1 atom in addition to 0.10e around the nearest oxygen atom. That means the two electrons were trapped by an empty Mo1 4d state, and the point defect would not be considered as an F center. This study was published in Ref. [17]. Alike BaMoO$_4$-$V_0^\times$, in SrMoO$_4$-$V_0^\times$ (Fig. 5.6 b)), the spin-up charge density concentrates around the [MoO$_3$] cluster and the created vacancy, with identical magnetization per cell and Lowdin charges as before. Recently, Wang *et al.* [107] found that the electrons from a $V_0^\times$ in SrMoO$_4$ are mainly localized on the Mo1 atom rather than on the oxygen vacancy site. For CaMoO$_4$-$V_0^\times$, see Fig. 5.6 c), we have to reduce the isosurface value to 0.005 ev/Å^3, smaller than the standard value of 0.013 ev/Å^3 used in the others. Even reducing the isosurface, we observe a small amount of spin-up charge density around Mo closest to Mo1. In Fig. 5.6 d), PbMoO$_4$-$V_0^\times$ shows similar net spin-charge density and a total magnetization per cell of 2 μ_B and 1.80e of Lowdin charge on Mo1.

The results of DOS and magnetic moment depend on the oxygen vacancy concentration as is shown in [30], where the authors used a supercell for BaMoO$_4$ with 24 oxygen atoms, with 4.17% and 8.34% of oxygen vacancy, corresponding to one and two oxygen vacancies, respectively. It corroborates with our result for a supercell with 16 oxygen atoms, with a concentration of 6.25% of oxygen vacancy. Although the DOS obtained from the present calculation is differ-

ent from that obtained in reference [30], the magnetic moment is in complete agreement with that of reference [30] for 8.33% of vacancy concentration. In the work of Wang *et al.* [107] for $SrMoO_4$, they used a supercell containing 96 atoms, being 64 oxygen atoms. They created one oxygen vacancy, which corresponds to a diluted vacancy concentration of 1.5%. The DOS obtained by the authors is similar to [30]. However, they did not calculate the total magnetization. In summary, there are two crucial points in understanding these results: the Hubbard value on Mo atoms can affect the CF of $4d$ states, and the vacancy ratio compared to supercell modifies the total magnetization of the bulk.
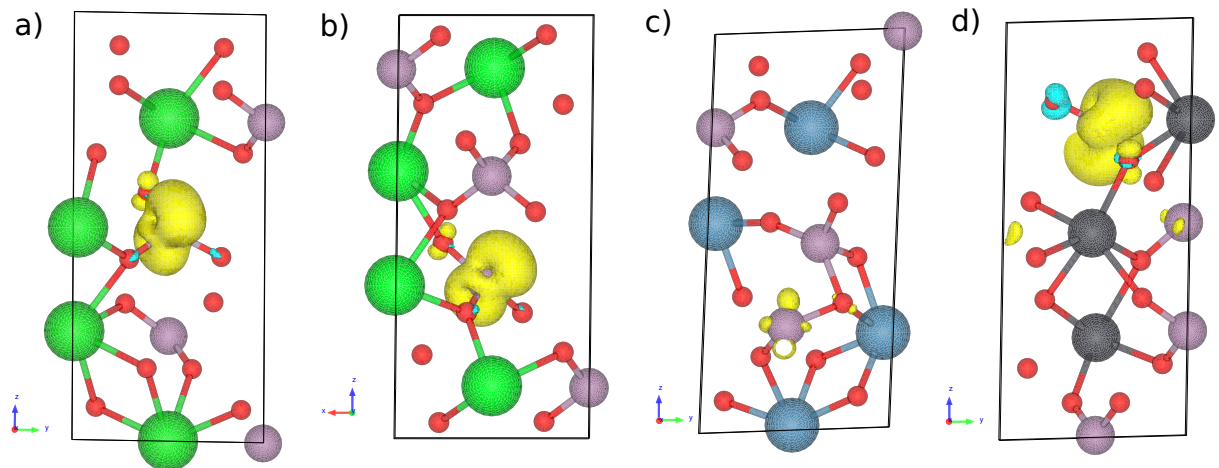
Figure 5.6 - Net spin-charge density in vacancy $BaMoO_4$, a), $SrMoO_4$, b), $CaMoO_4$, c), and $PbMoO_4$, d). The yellow surface mans spin-up density.

5.2   Optics

By calculating the bands of pure molybdates, the point group of the top of the valence and the bottom of conduction band was found to be S_4. Thus, the calculations concerning optical properties, including the absorption spectra, are driven by the selection rule, which depend on each point group. Despite the common use of T_d point group for defining the $[MoO_4]$ cluster, we consider S_4 as the most suitable one for explaining the theoretical results. It is noted that
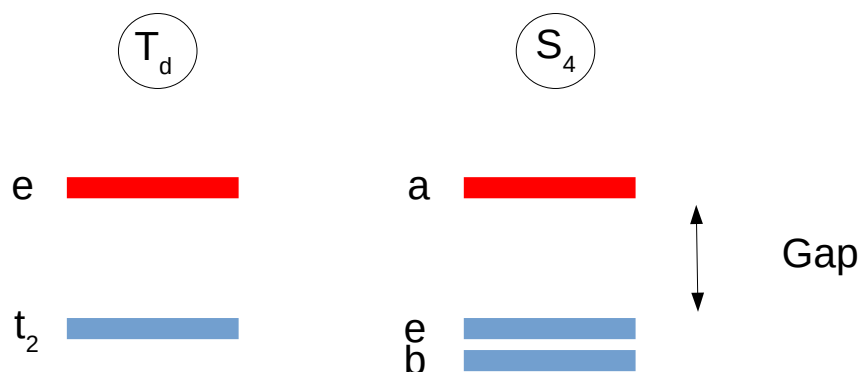
Figure 5.7 - Energy diagram sketch from valence (blue line) and conduction (red line) states using S_4 symmetry provided by theoretical calculations, and T_d symmetry widely adopted.

for T_d point group, the valence bands (due to T_2 symmetry) has $2px$, $2py$, and $2pz$ degeneracy. However, in our work, as shown in PDOS (Fig. 5.2) and by orbitals (Fig. C.2), only $2px$, $2py$ are degenerate, even though $2pz$ lies close to the valence band and is consistent with S_4. The schematic comparison is presented in Fig. 5.7.

In this section, we have focused on the optical properties of the incident electromagnetic wave in the z direction to facilitate the comparison among the molybdates with and without vacancies.

Below we will check the electronic transition from the top of the valence band to the lower part of the conduction band under the point group selection rule. In Table 5.2, we show the direct product from the required symmetry given by the T_d character table (Appendix C.1).

Table 5.2 - Direct product in T_d point group considering the final state with E symmetry and polarization with T_2 symmetry.

E	2	-1	2	0	0
T_2	3	0	-1	-1	1
T_2	3	0	-1	-1	1
$E \otimes T_2 \otimes T_2$	18	0	2	0	0

As explained in Chapter 2, the presence of A_1 ensures the transition occurrence. This is achieved by:

$$A_1 = \frac{1}{24}[(1.1.18) + (8.1.0) + (3.1.2) + (6.1.0) + (6.1.0)] = 1; \qquad (5.1)$$

therefore, it is an electric dipole allowed transition. For S_4 point group, the same procedures are given in Table 5.3 using respective character table (Appendix C.2), which is electric dipole

Table 5.3 - Direct product in S_4 point group considering the final state with A symmetry and polarization with B symmetry.

A	1	1	1
B	1	-1	1
B	1	-1	1
$A \otimes B \otimes B$	1	1	1

allowed. For the initial state (top of valence band) with E symmetry, only for x or y polarization is the transition allowed, a result different from T_d. The deviation among other polarization can be seen in Appendix C.2 and is completely explained by S_4 symmetry. Figs. 5.8 a) - c) shows the absorption, reflectivity, and index of refraction spectra, respectively, for all molybdates. In Fig. 5.8 a), the energy threshold varies according to the optical gap energy. The first peak, around 5 eV, corresponds to the optical transitions from the b valence states to a conduction states. This material does not absorb photons with frequencies in the visible range, meaning it is transparent.
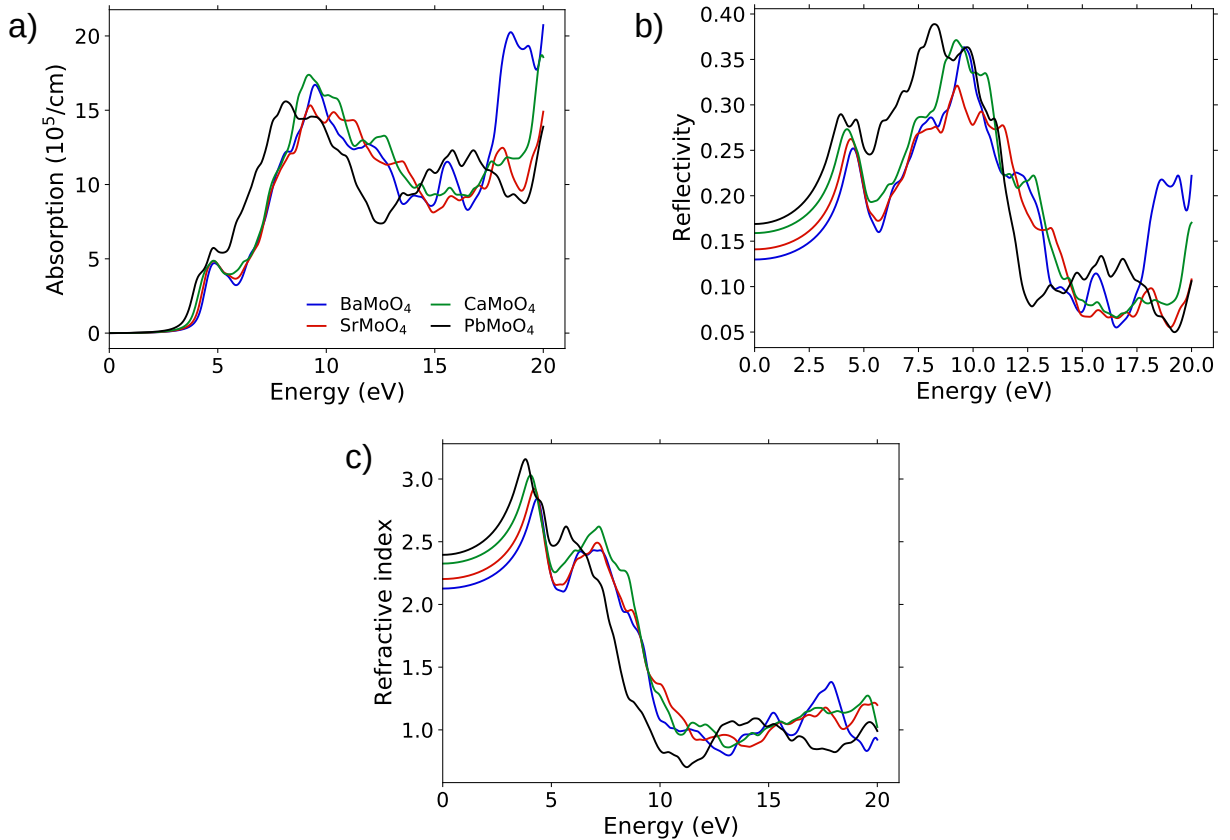
Figure 5.8 - Comparison of absorption, a), reflectivity, b), and index of refraction, c), for pure $BaMoO_4$, $SrMoO_4$, $CaMoO_4$, and $PbMoO_4$.

However, this characteristic favors UV photocatalytic degradation of known pollutants, such as methyl orange [108], sulfamethoxazole drug [109], 2,6-dichlorobenzamide (BAM) pesticide [110], organic compound, and water splitting [18]. In Fig. 5.8 b), the reflectivity in the infrared region varies between 14% in $BaMoO_4$ and 17% in $PbMoO_4$, with a maximum of approximately 40% for higher frequencies in the order of 10 eV in incident light. Fig. 5.8 c) presents the

Table 5.4 - Summarized index of refraction (n) in z direction of molybdates calculated via DFT and comparison with experimental measurements.

Material	n	Experimental
$BaMoO_4$	2.12	
$BaMoO_4 - V_0^\times$	1.82	
$SrMoO_4$	2.20	1.95^a
$SrMoO_4 - V_0^\times$	1.89	
$CaMoO_4$	2.32	2.04^a
$CaMoO_4 - V_0^\times$	2.28	
$PbMoO_4$	2.39	2.24^b
$PbMoO_4 - V_0^\times$	2.17	

^{a} Ref. [111]
^{b} Ref. [112]

refraction index, and an experimental comparison is given in Table 5.4. The obtained values are reasonably close to experiments. When polarization in *x* and *y* axes are considered, in Figs. C.4 c), C.6 c), C.8 c), and C.10 c), a birefringence is observed, as expected in S_4 point group and by experimental measurements.

Defects in materials with bounded metal and oxygen atoms enhance photocatalytic activity, as is shown for CeO_2 with Fe impurities [113], and for co-doped CeO_2 with and without oxygen vacancies [114, 115]. In Fig. 5.9, we show the absorption, reflectivity, and refractive
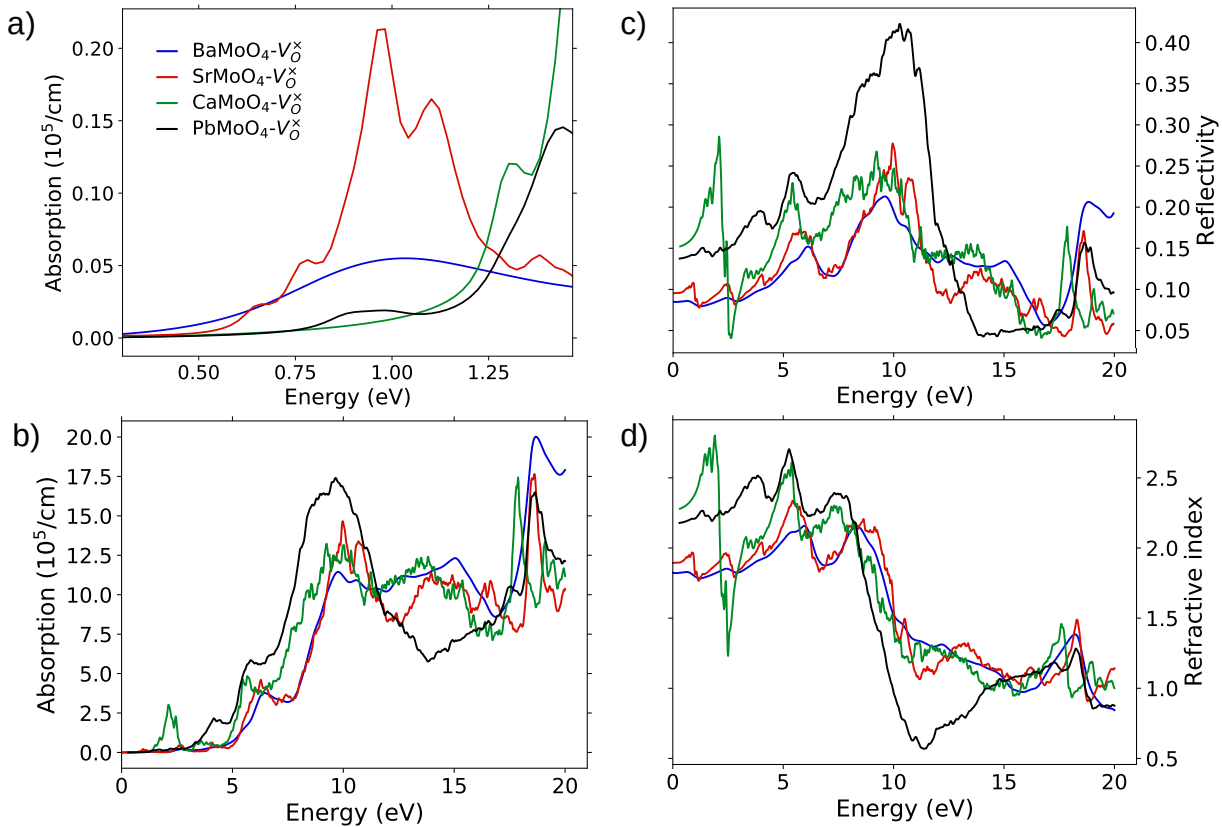
Figure 5.9 - Comparison of absorption insert, a), absorption, b), reflectivity, c), and index of refraction, d), for defective $BaMoO_4$, $SrMoO_4$, $CaMoO_4$, and $PbMoO_4$.

index of $AMoO_4$ with oxygen vacancy. Fig. 5.9 a) presents the absorption spectra focusing on the peaks that are related to the narrow bands created inside the gap. For $BaMoO_4$ and $PbMoO_4$ with vacancy, the energy threshold is around 0.5 eV with a maximum of around 1.0 eV, similar to $SrMoO_4$-$V_0^\times$, but, in the later, the peaks are more pronounced due to minor smoothing settings. For $CaMoO_4$-$V_0^\times$, the absorption peak at 1.3 eV is in complete accordance with PDOS. In all cases, the absorption comes from O $2p$ to Mo $4d$. The full range spectrum, given in Fig. 5.9 b), shows a strong absorption at about 2.0 eV in $CaMoO_4$-$V_0^\times$ due to the presence of a larger number of states in the narrow bands when compared to the others. The peaks above 5 eV are reminiscent of the pristine $AMoO_4$, corresponding to the optical transition from the wide valence band to the lowest and higher empty bands, respectively. We also observe that the oxygen vacancy induces absorption in the near-infrared region (NIR) and visible region, which

is not seen in pristine material. This can be potentially favorable to photocatalysis activity since the optical gap is reduced, and this reduction favors the electron-hole pair formation, although the absorption due to non-vacancy [MoO_4] clusters in $BaMoO_4$-Vo is blue-shifted.

For reflectivity spectra in Fig. 5.9 c), the introduction of oxygen vacancy decreases the reflectivity of $AMoO_4$ about 30% at low energies for all materials considered in this study. Even the maximum value is shrunk by oxygen vacancy. Since the absorption in $CaMoO_4$-$V_0^\times$ are so intense, the reflectivity drops sharply. When incident energy rises, reflectivity behavior becomes similar, indicating that vacancy effects on optical properties are confined up to 16 eV. The same behavior occurs in the refractive index, as is shown in Fig. 5.9 d), where the initial index of refraction is less than that one for pristine, as given in Table 5.4.

5.3   Infrared spectra and dielectric constant

In the previous section, we calculated the optical properties derived from the real and imaginary dielectric functions. While the imaginary part addresses absorption, the high-frequency of the real part is often used to obtain the optical dielectric constant or relative permittivity of the material. Due to technical reasons, only pristine crystals had their dielectric constant (ε_R) calculated, as shown in Fig. 5.10. In this graph, it is observed that the high-frequency (ε_∞) di-
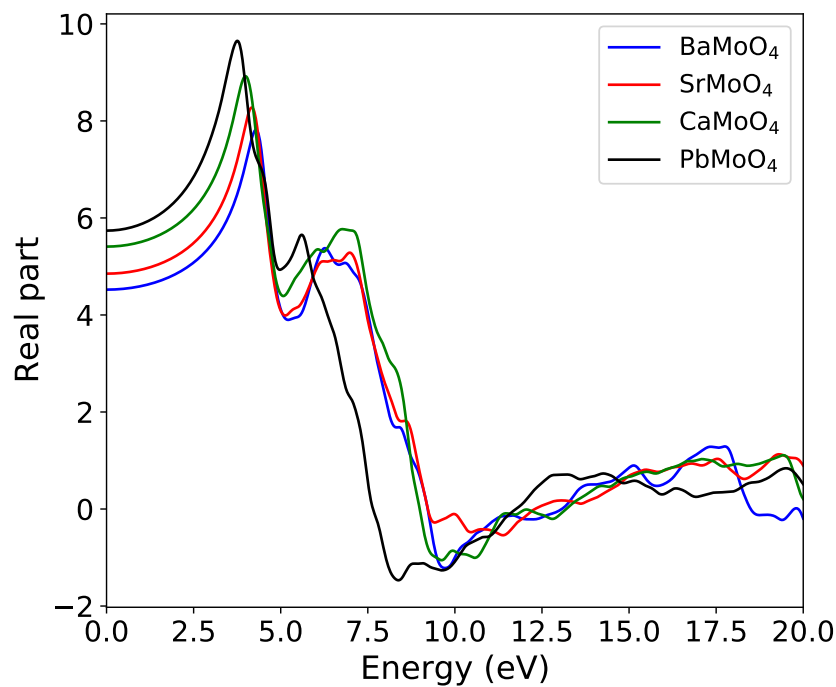
Figure 5.10 - Comparison of the real part of the dielectric function for an electric field along *z* for all pristine molybdates.

electric constant increases as the gap of the material decreases, a phenomenon typically seen[1], and can be rationalized by the fact that the band gap reflects the bonding-antibonding separation. So a small gap means higher electronic polarizability associated with the facile excitation into antibonding states, leading to higher ε_R [116].

For numerical comparison, given in Table 5.5, ε_∞ are not in agreement with the experimental. Thus, a possible manner to overcome this issue comes from group theory, where the tetragonal cluster [MoO$_4$] has T_d, or more precise, S_4 symmetry, meaning no inversion center, and this, together with the birefringence property, indicates that these molybdates in scheelite structure are polar crystals. Therefore, the transverse-longitudinal optical modes play an important role in describing the dielectric constant. In order to execute this task, we have performed the phonon calculation only at the Γ point. The obtained results are vibrational modes that can be used to plot the infrared spectrum.

Table 5.5 - Comparison of dielectric constant (ε_R) obtained with contribution of TO-LO splitting, high-frequency dielectric constant (ε_∞), and experimental measurements.

Material	ε_R	ε_∞	Experimental
BaMoO$_4$	9.54	4.52	9.30[a]
SrMoO$_4$	9.25	4.85	9.49[a]
CaMoO$_4$	10.90	5.40	10.79[a]
PbMoO$_4$	27.37	5.74	25.40[b]

[a] Ref. [14]
[b] Ref. [117]

The molybdate primitive cell with C_{4h} point group, has 26 vibrational modes [103], given by:

$$\Gamma_{\text{Raman+Infrared}} = (3A_g + 5B_g + 5E_g) + (5A_u + 3B_u + 5E_u), \tag{5.2}$$

where Raman active modes are A_g, B_g, and E_g, and the infrared modes are, A_u, B_u, and E_u. We plot the infrared spectrum and compare it to experimental data, as can be seen in Figs. 5.11 a) - d), for BaMoO$_4$, SrMoO$_4$, CaMoO$_4$, and PbMoO$_4$, respectively. A good agreement with the experiment is observed, especially in external modes (ranging from 790 cm^{-1} to 900 cm^{-1}) relative to [MoO$_4$]$^{2-}$. Taking into account the TO-LO splitting in the calculation, it allows us to obtain a precise dielectric value (ε_R) in all molybdates, as seen in Table 5.5. We expected the ε_R in SrMoO$_4$ to be greater than BaMoO$_4$ since experiments show smaller gap in SrMoO$_4$. However, this discrepancy is not too large. This work shows the importance of considering the inclusion of TO-LO splitting in phonon calculation since a precise dielectric constant value is

---

[1] This is not a rule. In fact, it is a field of study in materials science seeking high dielectric materials with a large band gap.

sensitive to TO-LO splitting.
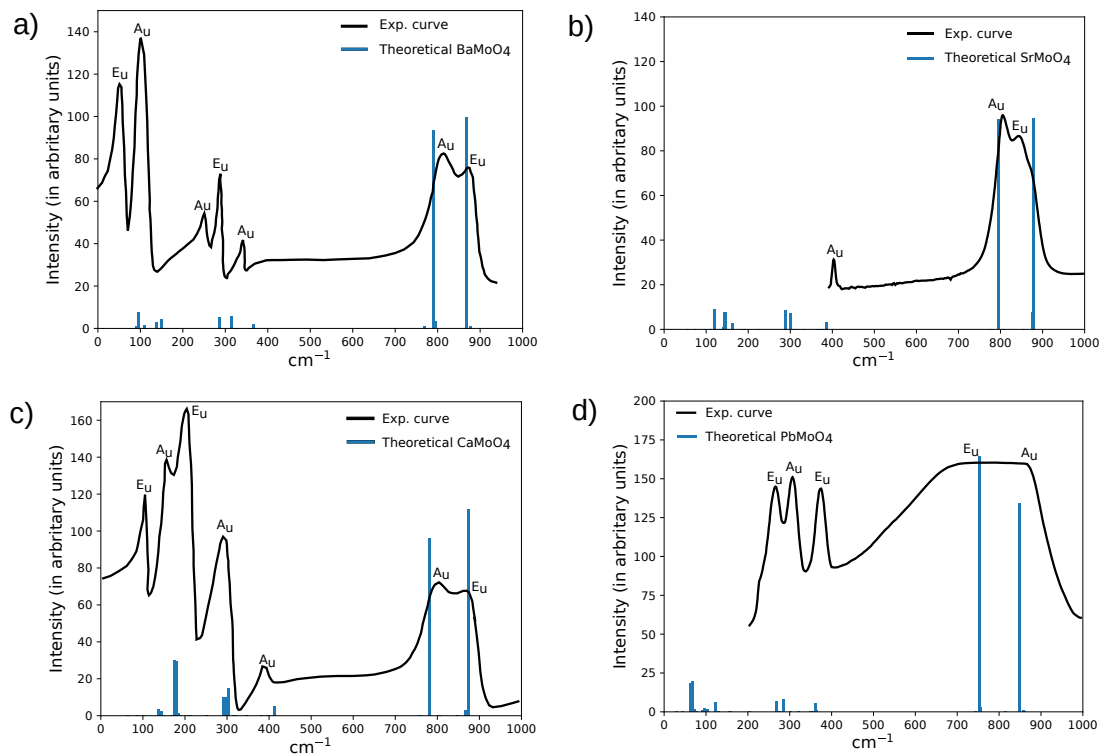
Figure 5.11 - Comparison of the real component of dielectric function in direction *z* for all pristine molybdates.

MECHANICAL, THERMAL, AND TRANSPORT PROPERTIES OF MOLYBDATES

In this chapter, we present the results for mechanical, thermal and thermoelectrical properties of $BaMoO_4$, $SrMoO_4$, $CaMoO_4$, and $PbMoO_4$ with and without vacancy. The mechanical properties, include the bulk modulus, Young modulus, shear modulus, Poisson ratio, and Vicker's hardness, which are derived from the calculated elastic constants. For the thermal properties we obtained the Debye temperature and the lattice thermal conductivity, via Slack and Klemens theory. The thermolectrical properties calculated, include the electronic conductivity, the Seebeck coefficient, the electronic thermal conductivity, and the power factor. From these last results the figure of merit was developed, indicating that these materials are efficient candidates to convert thermal energy into electrical one.

6.1 Mechanical properties

The elastic constants are essential to provide insight into the mechanical properties of a material. Specifically, they are used to determine the stiffness of a material, which directly affects its ability to resist the deformation under stress. They can also predict the mechanical stability of materials, especially those including engineered defects, assuring their possible existence. In the present work, we have calculated all required stiffness constants for pristine $AMoO_4$ and for $AMoO_4$ with oxygen vacancy. We calculated all their elastic constants, according to the stress-strain model, to assure the possible existence of $AMoO_4$ crystal with oxygen vacancy.

The pristine $AMoO_4$ point group is classified as Laue class C_{4h} $(4/m)$, which is associated with a tetragonal crystal system. Its stiffness matrix is composed of 7 independent elastic constants. To be mechanically stable, it must fully meet the Born stability criteria [118] given by:

$$C_{11} > |C_{12}| \tag{6.1}$$
$$2C_{13}^2 < C_{33}(C_{11}+C_{12}) \tag{6.2}$$
$$C_{44} > 0 \tag{6.3}$$
$$2C_{16}^2 < C_{66}(C_{11}-C_{12}). \tag{6.4}$$

The stiffness constants (in GPa) for pristine $AMoO_4$ and $AMoO_4 - V_O^\times$ are presented in Table 6.1.

Table 6.1 - This table presents the calculated elastic constants in GPa for pristine and defective molybdates.

	Materials							
	Pristine				**Vacancy**			
C_{ij}	$BaMoO_4$	$SrMoO_4$	$CaMoO_4$	$PbMoO_4$	$BaMoO_4$	$SrMoO_4$	$CaMoO_4$	$PbMoO_4$
C_{11}	89.2	108.0	118.6	107.6	108.4	104.4	95.8	86.7
C_{22}	89.2	108.0	118.6	107.6	103.4	106.2	119.2	80.4
C_{33}	88.5	96.1	117.6	91.6	91.3	90.5	87.5	47.0
C_{44}	14.9	32.1	30.3	28.5	38.1	28.0	27.4	20.4
C_{55}	14.9	32.1	30.3	28.5	40.2	25.9	17.6	21.7
C_{66}	32.2	36.6	37.3	37.8	48.7	38.5	46.5	36.3
C_{12}	35.0	46.5	48.3	47.0	46.5	50.5	51.0	34.6
C_{13}	29.7	44.3	49.3	43.3	47.4	30.2	29.6	22.7
C_{14}	-	-	-	-	0.3	-4.2	-3.2	-2.4
C_{15}	-	-	-	-	8.9	-5.6	-6.4	0.6
C_{16}	-10.1	9.5	-8.1	-10.0	15.7	23.3	-0.9	-18.3
C_{23}	29.7	44.3	49.3	43.3	35.0	34.2	34.9	20.7
C_{24}	-	-	-	-	0.2	-4.5	-8.7	0.3
C_{25}	-	-	-	-	1.3	-5.3	-0.5	0.8
C_{26}	10.1	-9.5	8.1	10.0	-1.4	3.1	22.1	-4.7
C_{34}	-	-	-	-	-11.5	-5.4	-11.4	-1.4
C_{35}	-	-	-	-	31.4	-6.7	-2.1	-0.1
C_{36}	-	-	-	-	-8.4	5.6	-13.4	2.9
C_{45}	-	-	-	-	-3.8	-2.6	-8.1	-1.2
C_{46}	-	-	-	-	-2.9	-0.9	-2.2	-1.8
C_{56}	-	-	-	-	4.9	-1.8	4.7	0.9

Considering the pure crystals, the Born stability is achieved in all cases. We observe that $C_{11} = C_{22} > C_{33}$, although in $BaMoO_4$ and $CaMoO_4$ these differences are relativity small, that means along the [100] direction the bonding strength are stiffer than [001]. For shear deformation, which is connected to C_{44}, C_{55} and C_{66}, related to (100), (010), and (001) crystal planes, respectively, it is seen that the shear along (100) and (010) are easier than along (001) as $C_{44} < C_{66}$. The elastic constants agree well with other experimental and theoretical studies, especially in $PbMoO_4$, as can be seen in Table 6.2.

When the vacancy is introduced, the symmetry is reduced, resulting in a triclinic crystal of Laue class C_1. In this symmetry, the total number of independent tensor elements is 21. Thus, according to [118], the necessary and sufficient condition to assure elastic stability is that all eigenvalues of C_{ij} must be positive. The stiffness constants are shown by the stiffness matrix (6.1). After numerical analysis, we verified that all its eigenvalues are positive, obeying the above stability criterion. The obtained results, in general, indicates that $AMoO_4$ with a vacancy is more vulnerable to compression along all principal axis when compared to pristine case. However, an increase in the tensile strength as well its shear resistance is observed for $BaMoO_4$. For $SrMoO_4$-$V_0^{\times}$ and $CaMoO_4$-$V_0^{\times}$, the shear stress along (001) plane increases, while in $PbMoO_4$-$V_0^{\times}$ decreases a little.

Table 6.2 - Table containing experimental and theoretical stiffness constants for comparison to pristine molybdates in scheelite phase calculated in this work. The elastic constants are given in GPa.

Materials	Stiffness constants						
	C_{11}	C_{12}	C_{13}	C_{16}	C_{33}	C_{44}	C_{66}
$BaMoO_4$							
PBEsol[b]	96.6	56.6	44.8	-10.9	84.1	27.6	34.4
PBEsol[c]	98.7	55.0	45.2	-13.1	97.5	30.0	37.7
$SrMoO_4$							
Exp.[a]	119.0	62.0	48.0	-12.0	104.0	34.9	42.0
PBEsol[b]	121.1	61.0	46.1	-13.1	105.7	34.0	43.7
PBEsol[c]	123.6	59.5	49.9	13.2	114.3	34.1	44.3
$CaMoO_4$							
Exp.[a]	144.0	65.0	45.0	-14.0	126.0	36.9	46.1
PBEsol[b]	140.4	61.0	46.1	-13.1	105.7	34.0	43.7
PBEsol[c]	147.6	68.5	52.4	-14.7	132.8	34.6	43.7
$PbMoO_4$							
Exp.[a]	109.0	68.0	53.0	-14.0	92.0	26.7	33.7
PBEsol[b]	113.6	69.2	53.7	-12.5	95.7	25.9	40.5

[a] Ref. [119].
[b] Ref. [120].
[c] Ref. [32].

The mechanical properties, such as the bulk modulus (B_H), Young's modulus (E_H), shear modulus (G_H) and Poisson's ratio (ν_H) using the Hill approximation for all molybdates, with and without vacancy, are calculated in order to compare the load resistance variation promoted by the oxygen vacancy. These data are summarized in Table 6.3. Through experimental measurements available, it is possible to observe that bulk modulus in all pristine cases is in accordance with the literature, although the adopted pseudopotential underestimates the mechanical constants. At the same time, the functional PBEsol agrees better to the experimental. However, through an empirical formula to estimate the bulk modulus for scheelite compound proposed by Errandonea *et al.* [9] written as $B = 610Z_i/d^3$, where $Z_i = 2$ is the formal A-cation charge ($AMoO_4$) and d is the mean distance between A and O (see Table 4.4), the bulk modulus calculated in this work agree better than compared to PBEsol.

Generally, all mechanical constants decrease when the vacancy is introduced compared to that of pristine case. In $BiVO_4$ with oxygen vacancy [27] at the monoclinic scheelite phase, it reproduced similar behavior reducing the elastic constants, even though being in a less symmetric phase than pure scheelite. However, for $BaMoO_4$, we observe an increase in all mechanical constants, and this behavior is recently seen in $BaTiO_3$-V_0 [124].

The cation-oxygen distance inside the AO_8 complex plays a vital role in understanding the compression strength [122] in $AMoO_4$. As its charge Z_i is lower than the charge in the MoO_4 complex, the electrons inside the AO_8 complex are not highly localized as in the latter. When external pressure is applied to a $AMoO_4$ sample, the volume of the deltahedron AO_8 deforms more than the volume of tetrahedron MoO_4. The same occurs in $AMoO_4$ and $AMoO_4$ with a vacancy (see Table 4.4), but this does not explain the increase in bulk modulus in $BaMoO_4$-$V_0^{\times}$, despite its stiffness constants being greater than the pristine case. The Pugh's ratio [74] B/G is associated with the material ductility. Values of B/G greater or less than 1.75 define if the material is ductile or brittle, respectively. From Table 6.3, despite some differences among bulk and shear modulus calculated by Najafvandzadeh *at al.* [120] and Liu *at al.* [32], B/G is essentially the same for pristine $AMoO_4$, except for $PbMoO_4$. This indicates that Pugh's ratio is almost independent of the pseudopotential used. We have found that it is ductile for all pristine $AMoO_4$. Although Pugh's ratio is not the ideal method to define a materials as ductility [125], the introduction of oxygen vacancy does not change the ductility of $AMoO_4$. However, in some cases it decreases near the limit, except for $PbMoO_4$-$V_0^{\times}$, which becomes brittle.

Poisson ratio ν is also related to the type of bonds. Values of order $n = 0.25$ indicates ionic bonding materials and, for $n = 0.1$, covalent bonding materials [126]. For the pristine material, a major ionic behavior is found, which is in accordance with the literature. The introduction of a vacancy $V_O^{\times}$ decreases ν but maintains its ionic bonding character. Hardness is described as the capability of a material to resist deformation. The hardness is correlated to shear and bulk modulus in a polycrystalline material. The obtained result suggests a way to

Table 6.3 - Table containing experimental, empirical, and theoretical mechanical properties obtained in this work and others for comparison. The bulk (B_H), shear (G_H), and Young's modulus (E_H) are given in GPa and using the Hill formulation. The empirical bulk modulus ($B_{emp.}$) is calculated following Errandonea et al. [9]. It also presented Pugh's (B_H/G_H) and Poisson's ratio (ν_ν), as well as Vicker's hardness (H_ν).

Materials	$B_{emp.}$ (GPa)	$B_{exp.}$ (GPa)	B_H (GPa)	G_H (GPa)	E_H (GPa)	B_H/G_H	ν_H	H_ν
$BaMoO_4$[a]	55.3	56[e]	50.7	22.2	58.1	2.27	0.30	1.82
$BaMoO_4$[b]			62.8	26.4	69.6	2.37	0.31	1.94
$BaMoO_4$[c]			65.0	29.1	75.9	2.23	0.30	2.61
$BaMoO_4$-$V_0^\times$ [a]			57.4	31.8	80.6	1.80	0.26	4.58
$SrMoO_4$[a]	67.0	72[d], 71[f]	67.1	31.6	81.9	2.12	0.29	3.24
$SrMoO_4$[b]			72.2	35.4	91.44	2.03	0.29	4.02
$SrMoO_4$[c]			75.4	35.7	92.7	2.10	0.29	3.75
$SrMoO_4$-$V_0^\times$ [a]			55.8	29.5	75.2	1.89	0.27	3.87
$CaMoO_4$[a]	79.3	79[d], 82[g]	73.6	33.1	86.4	2.22	0.30	3.08
$CaMoO_4$[b]			82.0	38.3	99.4	2.14	0.29	3.93
$CaMoO_4$[c]			85.7	39.3	102.3	2.18	0.30	3.88
$CaMoO_4$-$V_0^\times$ [a]			55.9	26.7	75.2	2.09	0.29	2.75
$PbMoO_4$[a]	64.4	71[d], 64[h]	64.3	29.8	77.6	2.15	0.29	2.92
$PbMoO_4$[b]			74.3	27.8	74.3	2.67	0.33	1.45
$PbMoO_4$-$V_0^\times$ [a]			38.8	23.2	58.1	1.67	0.25	3.89

[a] This work.

[b] Ref. [120].

[c] Ref. [32].

[d] Ref. [119] (experiment).

[e] Ref. [121] (experiment).

[f] Ref. [122] (experiment).

[g] Ref. [123] (experiment).

[h] Ref. [87] (experiment).

increase the hardness in molybdates since the hardness given in Vicker's method has increased in all $AMoO_4$ with vacancy.

The Debye temperature is an important physical parameter that characterizes the vibrational properties of a material. It is related to the heat capacity of a material. This essential thermodynamic property measures the amount of heat required to cause a change in the temperature of an object. From the average sound velocity (Eq. 3.76), we calculated the Debye temperature, given in Table 6.4, for all molybdates, including those with oxygen vacancy, using Eq. 3.75. The Debye temperature increases inversely proportional to cation weight, ranging from 278 K in $BaMoO_4$ to 396 K in $CaMoO_4$. Compared with other theoretical results, their values are greater; however, our results are in accordance with those obtained experimentally

Table 6.4 - Table containing experimental, empirical, and theoretical mechanical properties obtained in this work, and others, for comparison. The longitudinal (v_l), transverse (v_t), and average sound velocity ($\bar{v}_m$) are given in (m/s), the Debye temperature (Θ_D) in (K), the minimum lattice thermal conductivity.

Materials	v_l (m/s)	v_t (m/s)	$\bar{v}_m$ (m/s)	Θ_D (K)	κ_{clarke} (Wm^{-1}K^{-1})	$\gamma_{grüneisen}$
BaMoO$_4$[a]	4112	2163	2419	278	0.63	1.82
BaMoO$_4$[b]	4429	2300	3055	358	0.69	
BaMoO$_4$[c]				397	0.72	
BaMoO$_4$[d]				295		
BaMoO$_4$-$V_0^{\times}$ [a]	4561	2574	2864	327	0.73	1.57
SrMoO$_4$[a]	4908	2639	2947	355	0.83	1.75
SrMoO$_4$[b]	5189	2827	3714	444	0.88	
SrMoO$_4$[c]				470	0.90	
SrMoO$_4$[e]				373		
SrMoO$_4$-$V_0^{\times}$ [a]	4577	2548	2837	339	0.79	1.63
CaMoO$_4$[a]	5339	2831	3163	396	0.97	1.80
CaMoO$_4$[b]	5533	2969	3914	499	1.05	
CaMoO$_4$[c]				538	1.07	
CaMoO$_4$[f]				448		
CaMoO$_4$-$V_0^{\times}$ [a]	4756	2569	2867	354	0.85	1.72
PbMoO$_4$[a]	3988	2134	2383	284	0.66	1.76
PbMoO$_4$[b]	4021	2010	2692	327	0.66	
PbMoO$_4$[g]	3980	2020				
PbMoO$_4$-$V_0^{\times}$ [a]	3220	1858	2063	246	0.56	1.50

[a] This work.
[b] Ref. [120].
[c] Ref. [32].
[d] Ref. [127] (experiment).
[e] Ref. [128] (experiment).
[f] Ref. [129] (experiment).
[g] Ref. [130] (experiment).

by Morishita *et al.* [127, 128]. Debye temperature is smaller in all cases with vacancy, except in BaMoO$_4$-$V_0^{\times}$. Although an accurate Debye temperature for PbMoO$_4$ is not given, we obtained good longitudinal and transverse sound velocity results compared to [130].

In Fig. 6.1 it is shown the heat capacity at constant volume C_V calculated via the Debye model for AMoO$_4$ and AMoO$_4$-$V_0^{\times}$, where the former is represented by solid lines and the later by dashed lines. Experimentally it was observed that C_p is smaller in SrMoO$_4$ [128] than in BaMoO$_4$ [127]. It agrees with our results and can be extended to the other molybdates. We see that the heat capacity of AMoO$_4$ with a vacancy is generally greater than that of pristine AMoO$_4$, except for BaMoO$_4$. Therefore, the AMoO$_4$ materials present better electronic mobility.

The minima in the thermal conductivity (κ_{clarke}) provided by the Clarke's theory (Eq.
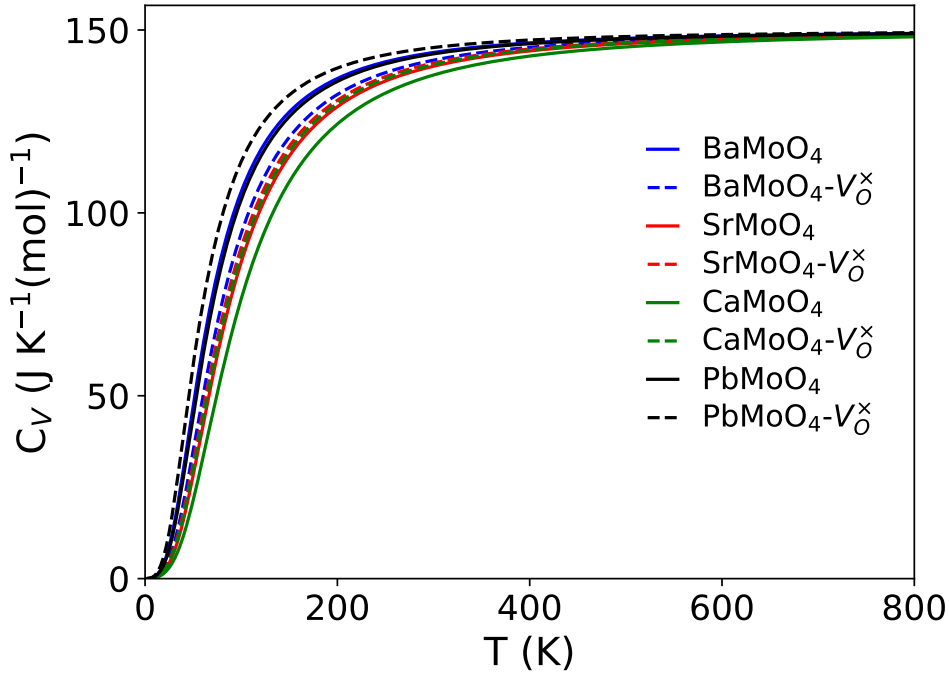
Figure 6.1 - Specific heat at volume constant for pristine molybdates in scheelite phase (solid lines) and its oxygen vacancy case (dashed lines).

3.87) is also presented in Table 6.4. These results indicate that $AMoO_4$ and $AMoO_4$-$V_0^{\times}$ more notably, can be classified as low thermal material, which is a preferable characteristic for the thermoelectric devices. The lattice thermal behavior as a function of the temperature depends on Grüneisen parameter (Eq. 3.89) and is given by Slack theory (Eq. 3.88). However, the vacancy creates defects in the lattice leading to phonon-scattering centers, which is not considered by Slack theory. Klemens theory accounts for point defects (Eq. 3.109), and the obtained lattice thermal conductivity in all pristine cases and its vacancy form is shown in Fig. 6.2.

6.2 Transport properties

Solids can transport heat, electricity, and light. In this section, we will focus mainly on the electrical properties, such as the electrical conductivity (σ), the Seebeck coefficient (S), and the coefficient κ (related to electronic thermal conductivity), which are driven by the Boltzmann equations defined in Chapter 3.10. In relaxation time approximation, these equations are presented in the BoltzWann module [131]. The code uses an alternative representation for the Bloch states, known as Wannier functions (WF), in which the WFs are constructed using the Wannier90 code [132].

There are few measurements of conductivity available for molybdates in the scheelite phase. The available data shows low conductivity [133, 134]. Therefore, due to its insulating character, we have only computed the thermoelectric (TE) properties for defective molybdates. According to Mahan [135], and Mahan and Sofo [136], they found that the best TE performance
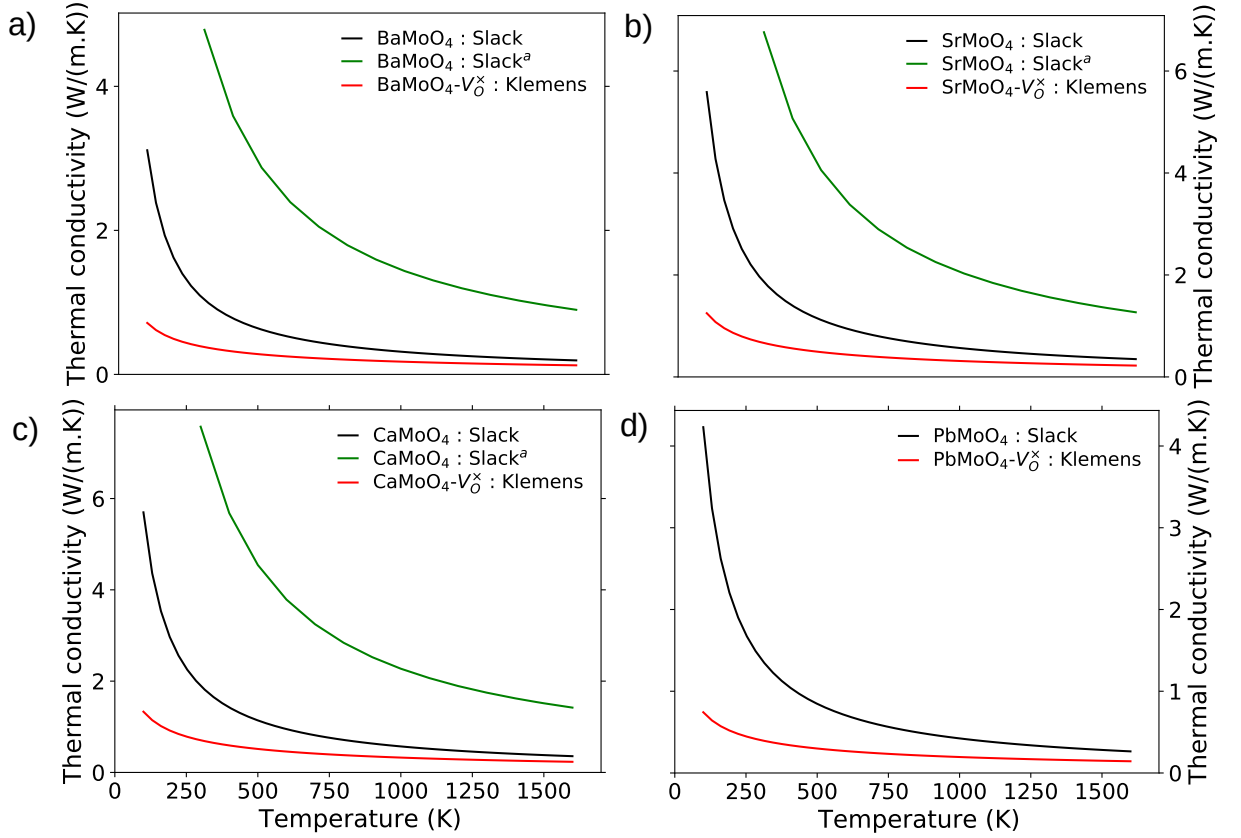
Figure 6.2 - Comparison of thermal lattice conductivity including the pristine material from this work given by the Slack theory (black lines), the pristine material calculated by ^{a}Ref. [32] (green lines), and oxygen vacancy materials from this work using the Klemens theory (red lines), for $BaMoO_4$, a), $SrMoO_4$, b), $CaMoO_4$, a), and $PbMoO_4$, d).

in semiconductor devices is in those materials whose band gap was around $10 K_B T$ for indirect-gap semiconductors, with T being the operating temperature.

The first step to calculate the TE properties is to compare the Wannier-interpolated band structure with the obtained via QE. From Fig. D.1, we see that the bands match precisely, indicating that wannierisation had been successfully achieved. The relaxation time (τ) was constant in all cases and is considered to be 1 fs.

Figs. 6.3 a) - d), display the chemical potential (μ) as a function of temperature (T) and carrier concentration (N) for $BaMoO_4$-$V_0^\times$, $SrMoO_4$-$V_0^\times$, $CaMoO_4$-$V_0^\times$, and $PbMoO_4$-$V_0^\times$, respectively. The chemical potential scale is not shifted by the Fermi energy, and the yellow area comprehends the band gap limits. By the side of each graph, the spin-polarized DOS is plotted for comparison. Considering lower carrier density, it is possible to observe that the chemical potential is above the middle of the band gap region, indicating an n-type extrinsic semiconducting behavior for all materials. We observe that for low carrier concentration, below 10^{17} cm^{-3} (excluding $CaMoO_4$-$V_0^\times$), the chemical potential is constant and temperature independent. The carrier lies in the extrinsic temperature region for these carrier quantities and temperatures. The electrons from these donor states are already in the conduction band, and intrinsic excitation

is insignificant, whose contribution becomes relevant with increasing thermal energy. As the carriers concentration increases, either more electrons or holes are excited, tuning the chemical potential towards the bottom of conduction bands for n-type carriers and towards upper valence bands considering p-type carriers. In this work, we have used the chemical potential for the n and p-type extrinsic carriers as those found in the bottom of conduction bands and the upper of valence bands, respectively. These values are summarized in Table 6.5. All TE properties as a function of chemical potential (μ) for all defective materials are given in Figs. D.2 - D.5.
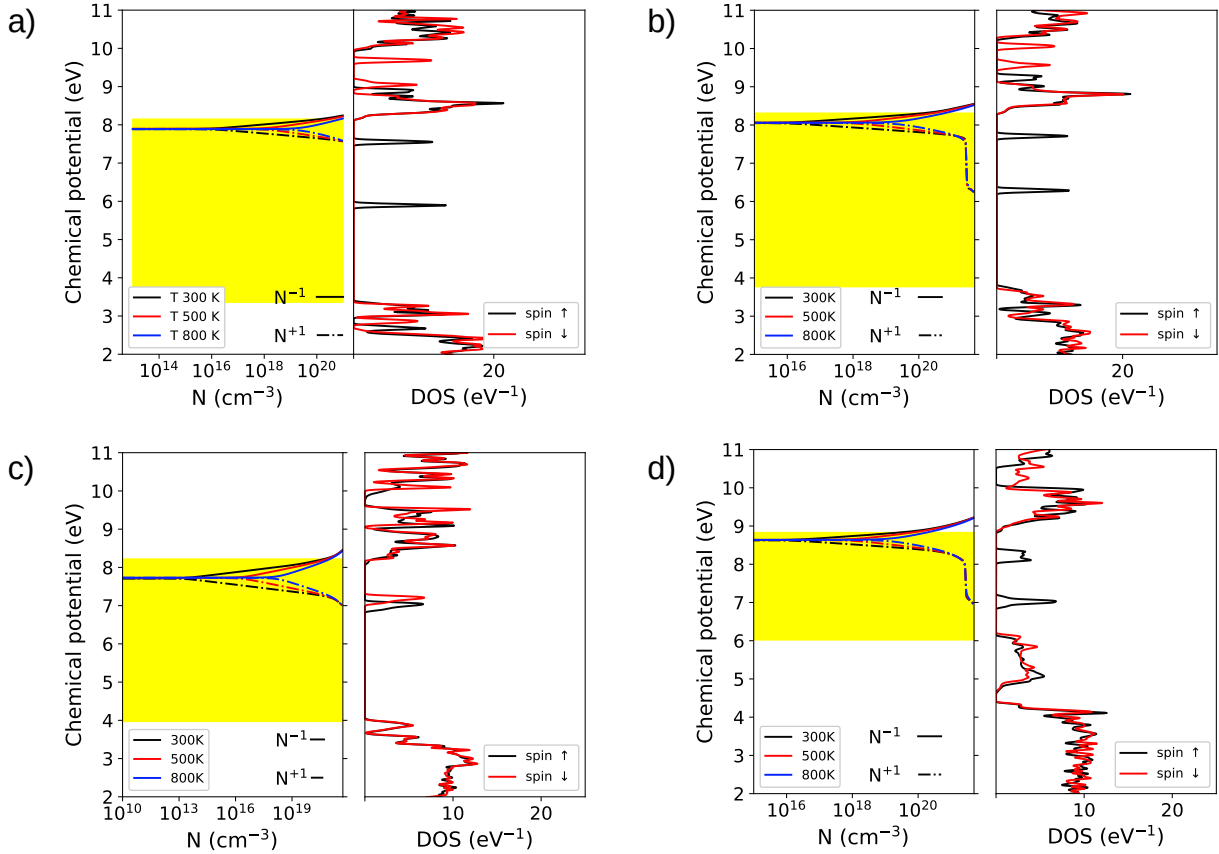
Figure 6.3 - Chemical potential (μ) for BaMoO$_4$-$V_0^\times$, a), SrMoO$_4$-$V_0^\times$, b), CaMoO$_4$-$V_0^\times$, c), and PbMoO$_4$-$V_0^\times$, d), as a function of temperature and the carrier concentration (N), being N^- the n-type carrier, and N^+, the p-type carrier. The bottom axes is in logarithm scale. The yellow area represent the band gap limits, and, by the side of each figure, the spin-polarized DOS is shown.

The temperature dependence of electrical conductivity (σ) in [xx] tensor component for all molybdates are shown in Fig. 6.4. In this figure, the dash-dotted line represents the p-type carriers, while the solid line represents the n-type carriers. We observe that electrons are the majority carriers since the number of electrons in the conduction bands exceeds the number of holes in the valence bands. The wider narrow bands within the forbidden region in CaMoO$_4$-$V_0^\times$ favor higher conductivity compared to others. For heavier lattice atoms, e.g., Ba and Pb, the p-type conduction drops as thermal energy rises. It is known that electrical conductivity is affected by carrier concentration and mobility through the relation, $\sigma = N|e|\mu$, where N = n (p) is the electron (hole) concentration, e is the electron charge, and μ is the mobility. In

Table 6.5, it can be viewed that only for BaMoO$_4$-$V_0^\times$, n-type impurity density is greater than

Table 6.5 - Summarized values of the bottom of conduction (top of valence) band chemical potential μ_e (μ_h) and its corresponding concentration N (cm^{-3}) obtained self-consistently for defective molybdates at 800 K.

Materials	$\mu_{\text{n-type}}$ (eV)	N_e (cm^{-3})	$\mu_{\text{p-type}}$ (eV)	N_h (cm^{-3})
BaMoO$_4$-$V_0^\times$	8.14	7.32×10^{21}	3.36	6.14×10^{21}
SrMoO$_4$-$V_0^\times$	8.30	5.78×10^{20}	3.77	5.79×10^{21}
CaMoO$_4$-$V_0^\times$	8.22	1.02×10^{21}	3.97	6.72×10^{21}
PbMoO$_4$-$V_0^\times$	8.84	4.34×10^{20}	6.02	7.04×10^{21}

p-type impurity, meaning that electron conductivity is greater than hole conductivity. On the other hand, it is known that carrier mobility diminishes as temperature and carrier concentration increase. Thus, even for the chosen hole density being greater than electron density in CaMoO$_4$-$V_0^\times$, in this material the hole mobility is much lower, leading to n-type conductivity being greater. For PbMoO$_4$-$V_0^\times$, it is observed that, even for greater hole concentration, the p-type conductivity is dominant in this temperature range. A detailed electrical conductivity as a function of temperature, including [yy] and [zz] tensor components, are given in Fig. D.6.
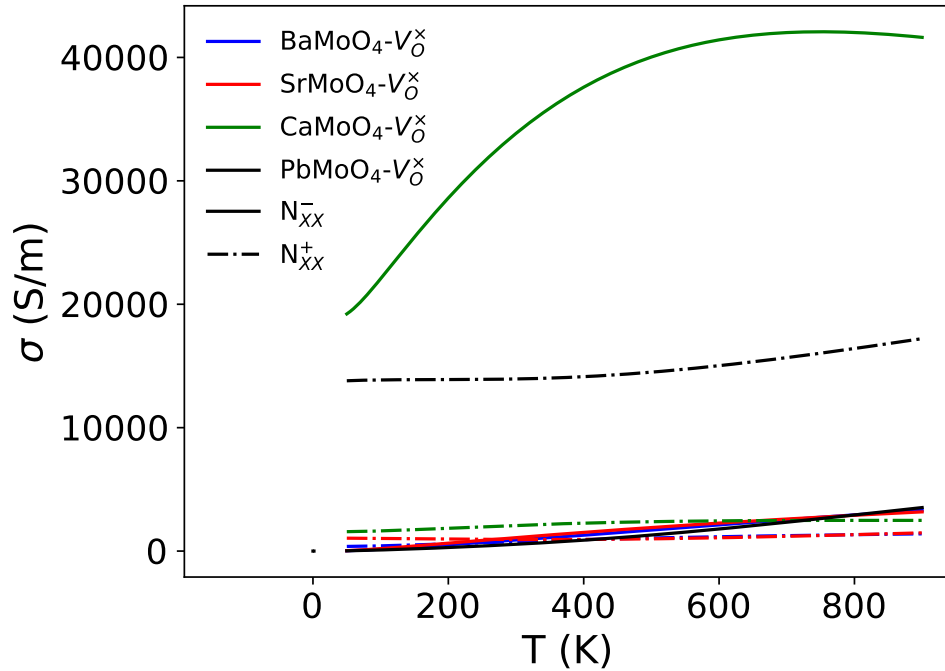
Figure 6.4 - The temperature dependence of electrical conductivity in [xx] tensor component for all defective molybdates. For each material, the chemical potentials used were given in Table 6.5. N^- represents the n-type carrier, and N^+, the p-type carrier.

In Fig. 6.5, we plotted the absolute Seebeck coefficient (S) as a function of temperature in [xx] tensor component. As the thermal energy increases, the Seebeck coefficient falls monotonically, unlike electrical conductivity, which increases. Seebeck coefficient as a function of temperature, including [yy] and [zz] tensor component, is plotted in Fig. D.7.
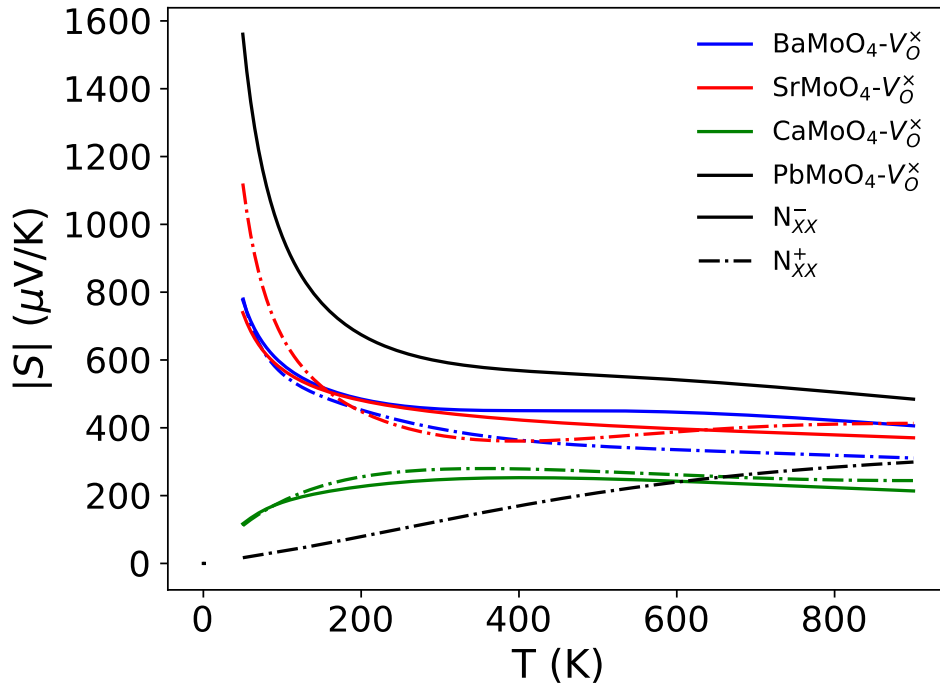
Figure 6.5 - The temperature dependence of absolute Seebeck coefficient in [xx] tensor component for all defective molybdates. For each material, the chemical potentials used were given in Table 6.5. N^- represents the n-type carrier, and N^+, the p-type carrier.

In Fig. 6.6, we plotted the electronic thermal conductivity (κ) as a function of temperature in [xx] tensor component. From the Wiedemann-Franz law, κ is proportional to σT, and
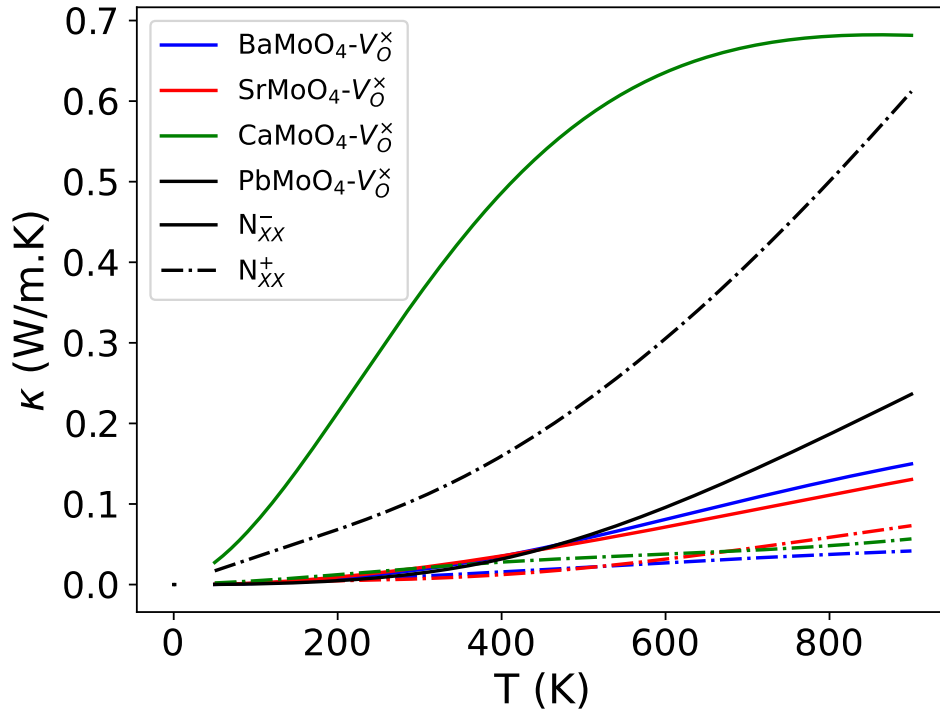
Figure 6.6 - The temperature dependence of electrical thermal conductivity in [xx] tensor component for all defective molybdates. For each material, the chemical potentials used were given in Table 6.5. N^- represents the n-type carrier, and N^+, the p-type carrier.

this behavior is seen for all molybdates, where the electronic thermal conductivity increases with temperature. It is possible to observe similar values either for lattice or electronic thermal conductivity, despite the later being approximately 8 times smaller. as result, the total thermal conductivity remains low, which benefits a thermal gradient between two edge of the materials. For detailed electronic lattice conductivity as a function of temperature, including [yy] and [zz] tensor component, see Fig. D.8.

In Fig. 6.7, we plotted the power factor (PF) as a function of temperature in [xx] tensor component. PF is a combination of σ and S^2, and this competition is generally inversely proportional to each other. However, as seen in Fig. 6.4, the conductivity for the n-type carrier in $CaMoO_4$-$V_0^\times$ increased significantly, leading to a high PF in mid temperature range. As the Seebeck coefficient decreases, the PF of this material starts decreasing. For other molybdates, the conductivity increases with an increase in temperature, whereas the Seebeck remains practically constant. This results in an increase in the PF for higher temperatures in $BaMoO_4$-$V_0^\times$, $SrMoO_4$-$V_0^\times$, and $PbMoO_4$-$V_0^\times$ for n-type carrier. For detailed PF as a function of temperature, including [yy] and [zz] tensor component, see Fig. D.9.
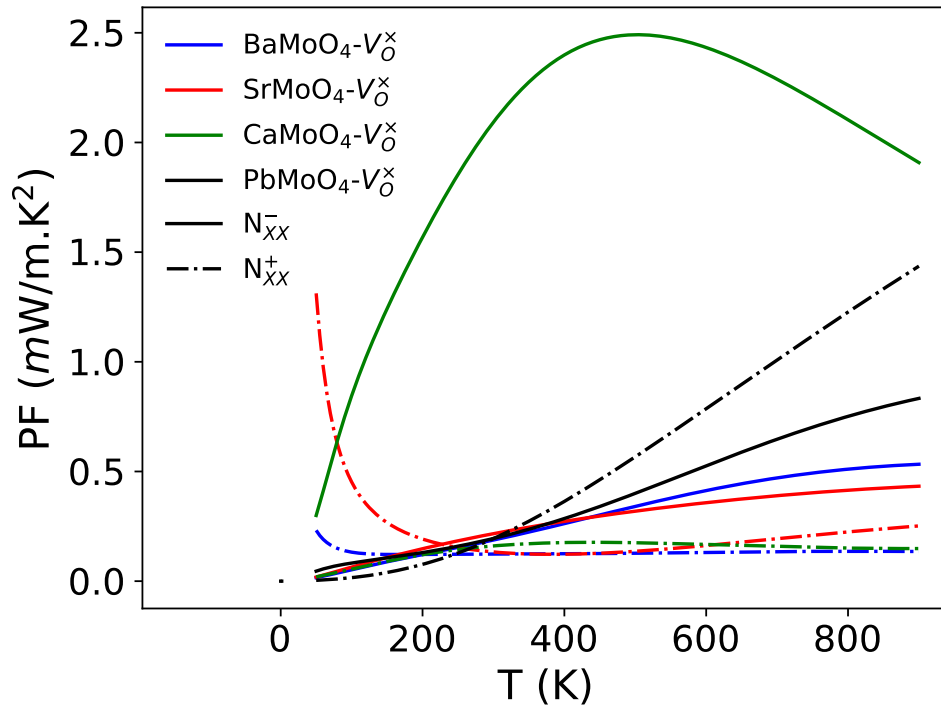
Figure 6.7 - The temperature dependence of Power factor (PF) in [xx] tensor component for all defective molybdates. For each material, the chemical potentials used were given in Table 6.5. N^- represents the n-type carrier, and N^+, the p-type carrier.

The dimensionless figure of merit, ZT, gives the conversion efficiency of TE materials. As seen in Section 3.10, ZT depends on the TE properties. Below (Fig. 6.8), the ZT values for all defective molybdates are exhibited. Accordingly to Mahan and Sofo [137], the best TE efficiency is found in materials with a sharp singularity in the density of states very near to the

chemical potential, that is, a density of state that tends to a delta function. This work shows that the oxygen vacancy produced a narrow band within the gap. For the materials whose difference in energy between these narrow bands and the conduction band was smaller, the value of ZT is greater, achieving up to ZT>1.65 in CaMoO$_4$-$V_0^\times$ and PbMoO$_4$-$V_0^\times$ at high temperatures. However, in CaMoO$_4$-$V_0^\times$ where the energy difference between the bottom of conduction and the top of the narrow band being the greater, the conductivity is also the greater, providing a higher ZT even for lower temperatures. Thus, this work provide a promising experimental method for enhancing the TE efficient in scheelite materials.
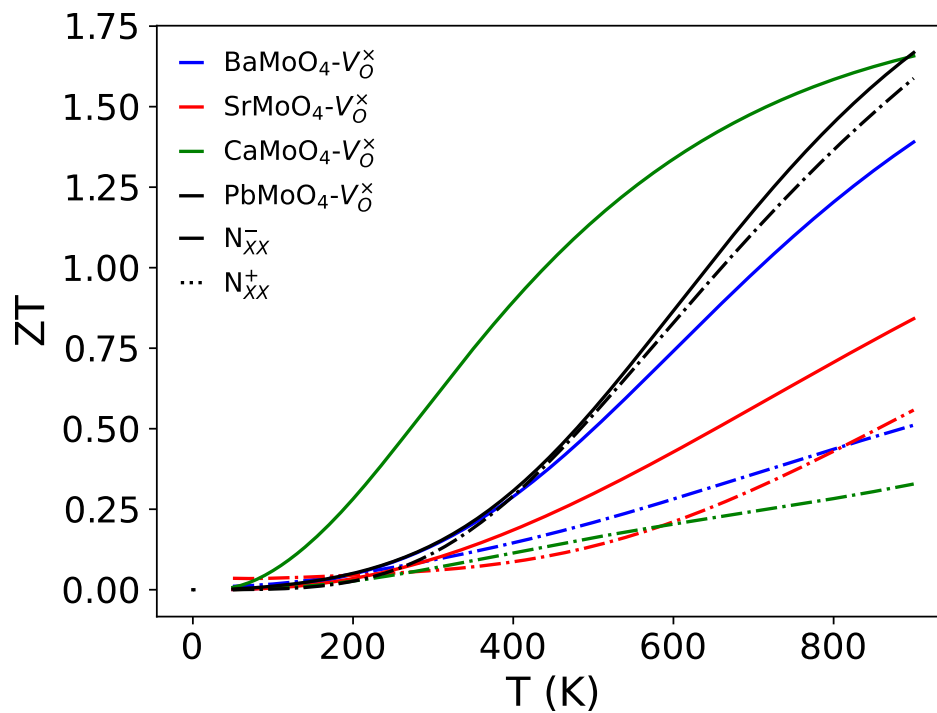
Figure 6.8 - The temperature dependence of figure of merit (ZT) in [xx] tensor component for all defective molybdates. For low temperatures, p-type carrier (N^+) provided better ZT values. For each material, the chemical potentials used were given in Table 6.5.

CONCLUSION

In this work, we have chosen the calcium, strontium, barium, and lead molybdate in the scheelite phase, aiming to deeply understand all kinds of changes promoted in these materials due to the introduction of one oxygen vacancy since this is a relevant topic for boosting materials properties, and in the recent years has become an attractive research field. In order to perform this study, we used an *ab initio* density-functional calculation implemented by the Quantum-Espresso package.

In the first part of this thesis, we compared the structural modification between the defective and pristine materials. We found that in $BaMoO_4$-$V_O^\times$ and $SrMoO_4$-$V_O^\times$, the cell parameters forming the conventional cell changed less than in $CaMoO_4$-$V_O^\times$ and $PbMoO_4$-$V_O^\times$, although in all cases the point group was reduced from C_{4h} to C_1, the lowest possible. Also, the length along the c axes shrank, but no noteworthy change in density was detected. Furthermore, the enthalpy formation energy indicates the existence of defective molybdates, and the energy required to remove one oxygen is similar for all molybdates, being easiest in $PbMoO_4$.

The second part was composed of electronic and optical studies. The calculations performed showed that observed ferromagnetism exists as a result of oxygen vacancy defects in $BaMoO_4$-$V_O^\times$, $SrMoO_4$-$V_O^\times$, and $PbMoO_4$-$V_O^\times$, which induce unpaired electrons around the oxygen vacancy trapped by the t_2'' and e' states of the Mo coupled to the vacancy in $BaMoO_4$-$V_O^\times$ and $SrMoO_4$-$V_O^\times$, and trapped by the t_2 and e states in $PbMoO_4$-$V_O^\times$. Due to more significant crystal field splitting, a small total magnetization of $0.15\mu_B$ was achieved for $CaMoO_4$-$V_O^\times$, in contrast with $2\mu_B$ calculated in the others. Concerning optical properties, the vacancy creates narrow states within the forbidden band, facilitating the electronic transition to conduction bands. Moreover, the absorption peak was observed in vacancy cases in infrared and visible light regions. In contrast, in pristine, the absorption peak has been seen only in the ultra-violet region. The indirect transition allied with a small gap can benefit photocatalysis, despite the small peaks in the absorption spectrum, and $PbMoO_4$ is not environmentally friendly.

In the last part, we calculated the mechanical, thermal, and transport properties of pristine and vacancy molybdates. Regarding elastic constants, the stiffness coefficients agree well when compared to available experimental data. The bulk modulus obtained for defective materials is lower than for pristine, generally. On the other hand, hardness has been increased in all cases, and we believe this is attributed to shorter bond lengths among the $A-O$ distances

when the vacancy is introduced. Also, oxygen vacancy diminishes the acoustic wave velocity, which benefits the acousto-optic effect. Lattice thermal conductivity is highly dependent on the Grüneisen parameter and Debye temperature. Considering the thermoelectric properties, they are given using the relaxation time approximation, except for the Seebeck coefficient. Thus, these properties should be carefully studied. The high ZT value obtained is addressed to narrow bands created within the gap due to oxygen vacancy. Consequently, this technique can potentially benefit the application of refrigerators, air conditioning, and other devices which depends on heating or cooling due to higher thermoelectric energy conversion.

In summary, introducing oxygen vacancy in the proportion 1/16 can induce magnetism; benefit photocatalysis; increases hardness; benefits the acousto-optic effect; lowers thermal conductivity; raise electronic conductivity; raise Seebeck coefficients at low temperatures; and boost thermoelectric efficiency in these materials.

Further perspectives include studying other oxygen vacancy proportions; surface vacancy; the influence of relaxation time in molybdates thermoelectric properties; dopping; Hubbard U+V; and external pressure.

BIBLIOGRAPHY

[1] Wyllamanney da S. Pereira, Júlio C. Sczancoski, and Elson Longo. Tailoring the photoluminescence of $BaMoO_4$ and $BaWO_4$ hierarchical architectures via precipitation induced by a fast precursor injection. *Materials Letters*, 293:129681, 2021.

[2] Daniel Errandonea and Francisco Javier Manjón. Pressure effects on the structural and electronic properties of ABX_4 scintillating crystals. *Progress in Materials Science*, 53(4):711 – 773, 2008.

[3] C. Tablero. Optical absorption and applications of the ABO_4 (A = Ca, Pb and B = Mo, W) semiconductors. *Chemical Physics Letters*, 635:190 – 195, 2015.

[4] M. Isik, N.M. Gasanly, N.H. Darvishov, and V.E. Bagiev. Growth and characterization of $PbMo_{0.75}W_{0.25}O_4$ single crystal: A promising material for optical applications. *Materials Chemistry and Physics*, 296:127280, 2023.

[5] J.C. Sczancoski, L.S. Cavalcante, N.L. Marana, R.O. da Silva, R.L. Tranquilin, M.R. Joya, P.S. Pizani, J.A. Varela, J.R. Sambrano, M. Siu Li, E. Longo, and J. Andrés. Electronic structure and optical properties of $BaMoO_4$ powders. *Current Applied Physics*, 10(2):614 – 624, 2010.

[6] Xiaofeng Guo, Qiren Zhang, Tingyu Liu, Min Song, Jigang Yin, Haiyan Zhang, and Xi'en Wang. First-principles study on electronic structures of $BaMoO_4$ crystals containing F and F^+ color centers. *Nuclear Instruments and Methods in Physics Research Section B: Beam Interactions with Materials and Atoms*, 267(7):1093 – 1096, 2009.

[7] I. C. Nogueira, L. S. Cavalcante, P. F. S. Pereira, M. M. de Jesus, J. M. Rivas Mercury, N. C. Batista, M. Siu Li, and E. Longo. Rietveld refinement, morphology and optical properties of $(Ba_{1-x}Sr_x)MoO_4$. *Journal of Applied Crystallography*, 46(5):1434–1446, Oct 2013.

[8] Ryan M. Kissinger, Saehwa Chong, Brian J. Riley, and Jarrod V. Crum. Synthesis and crystal structure of a mixed alkaline-earth powellite, $Ca_{0.84}Sr_{0.16}MoO_4$. *Acta Crystallographica Section E*, 76(2):121–124, Feb 2020.

[9] D. Errandonea, J. Pellicer-Porres, F. J. Manjón, A. Segura, Ch. Ferrer-Roca, R. S. Kumar, O. Tschauner, P. Rodríguez-Hernández, J. López-Solano, S. Radescu, A. Mujica, A. Muñoz, and G. Aquilanti. High-pressure structural study of the scheelite tungstates $CaWO_4$ and $SrWO_4$. *Phys. Rev. B*, 72:174106, Nov 2005.

[10] B. Binish, M. Durairaj, T.C. Sabari Girisun, and K. Mani Rahulan. Engineering the nonlinear optical properties of barium molybdate by doping Sn_4^+ ions for optical limiting device applications. *Ceramics International*, 2023.

[11] Ana Paula de Azevedo Marques, Nancy Kuniko Umisedo, Jessica Araujo Costa, Elizabeth Mateus Yoshimura, Emico Okuno, and Roseli Künzel. The role of capping agents on the trapping levels structure and luminescent emission of $SrMoO_4$ phosphors. *Journal of Luminescence*, 257:119662, 2023.

[12] L. Pattavina, S. Nagorny, S. Nisi, L. Pagnanini, G. Pessina, S. Pirro, C. Rusconi, K. Schäffner, V. N. Shlegel, and V. N. Zhdankov. Production and characterisation of a $PbMoO_4$ cryogenic detector from archaeological Pb. *The European Physical Journal A*, 56(2):38, Feb 2020.

[13] En-Cai Xiao, Jianzhu Li, Jing Wang, Chao Xing, Mei Guo, Hengyang Qiao, Qing Wang, Ze-Ming Qi, Gang Dou, and Feng Shi. Phonon characteristics and dielectric properties of $BaMoO_4$ ceramic. *Journal of Materiomics*, 4(4):383 – 389, 2018.

[14] Geun-Kyu Choi, Jeong-Ryeol Kim, Sung Hun Yoon, and Kug Sun Hong. Microwave dielectric properties of scheelite ($A = Ca, Sr, Ba$) and wolframite ($A = Mg, Zn, Mn$) $AMoO_4$ compounds. *Journal of the European Ceramic Society*, 27(8):3063–3067, 2007. Papers Presented at the Fourth International Conference on Microwave Materials and their Applications - MMA2006, Oulu, Finland.

[15] Marta Kowalkińska, Paweł Głuchowski, Tomasz Swebocki, Tadeusz Ossowski, Adam Ostrowski, Waldemar Bednarski, Jakub Karczewski, and Anna Zielińska-Jurek. Scheelite-type wide-bandgap ABO_4 compounds ($A = Ca, Sr,$ and Ba; B = Mo and W) as potential photocatalysts for water treatment. *The Journal of Physical Chemistry C*, 125(46):25497–25513, 2021.

[16] Schindra Kumar Ray and Jin Hur. Surface modifications, perspectives, and challenges of scheelite metal molybdate photocatalysts for removal of organic pollutants in wastewater. *Ceramics International*, 46(13):20608–20622, 2020.

[17] H. Pecinatto, Cícero Mota, and H.O. Frota. Determination of the mechanical, thermal, electronic and optoelectronics properties of $BaMoO_4$ with oxygen vacancy by ab-initio calculations. *Materials Today Communications*, 34:105074, 2023.

[18] Gizem Yanalak, Abdurrahman Ozen, Adem Sarılmaz, Ali Keles, Emre Aslan, Faruk Ozel, and Imren Hatay Patir. Scheelite-type $BaMoO_4$ and $BaWO_4$ based dye sensitized photocatalytic hydrogen evolution by water splitting. *Journal of Physics and Chemistry of Solids*, 168:110821, 2022.

[19] Anderson A.G. Santiago, Elida M. Macedo, Fernanda K.F. Oliveira, Ricardo L. Tranquilin, Marcio D. Teodoro, Elson Longo, Fabiana V. Motta, and Mauricio R.D. Bomio. Enhanced photocatalytic activity of $CaMoO_4/g - C_3N_4$ composites obtained via sonochemistry synthesis. *Materials Research Bulletin*, 146:111621, 2022.

[20] Mengzhu Jiang, Zhifen Chen, Yaohui Wu, Jinhua Luo, Aihua Zhang, Xiaoyong Chen, Yelin Zeng, Guangjun Wang, Yonghong Wang, and Yunlin Zhao. Novel $PbMoO_4$ loaded n-biochar composites with enhanced adsorption-photocatalytic removal of tetracycline. *Optical Materials*, 137:113540, 2023.

[21] Francisco Enilton Alves Nogueira, Tallison Oliveira Abreu, Vitor Carvalho Martins, Roterdan Fernandes Abreu, Felipe Felix do Carmo, João Paulo Costa do Nascimento, Anupama Ghosh, Antonio Jefferson Mangueira Sales, Marcelo Antonio Santos da Silva, Ronaldo Santos da Silva, and Antonio Sérgio Bezerra Sombra. Evaluation of the dielectric properties of $CaMoO_4\breve{}TiO_2$ composites for microwave applications under temperature variation. *Journal of Electronic Materials*, Feb 2023.

[22] Renan P. Moreira, Leonardo H.C. Francisco, Israel F. Costa, Helliomar P. Barbosa, Ercules E.S. Teotonio, Maria C.F.C. Felinto, Oscar L. Malta, and Hermi F. Brito. Luminescence properties of $BaMO_4 : Eu_3^+$ (M: Mo or W) phosphors derived from coprecipitation reaction. *Journal of Alloys and Compounds*, 937:168408, 2023.

[23] Prashant Dixit, Vaibhav Chauhan, S.B. Rai, and Praveen C. Pandey. Realization of neutral white light emission in $CaMoO_4 : 4Dy_3^+$ phosphor via Sm_3^+ co-doping. *Journal of Alloys and Compounds*, 897:162820, 2022.

[24] Arpita Vyas, C.P. Joshi, and S.V. Moharil. Nir emitting phosphors based on $PbMoO_4$ for modification of solar spectrum. *Journal of Luminescence*, 196:259–263, 2018.

[25] Ahmed Afif, Juliana Zaini, Seikh Mohammad Habibur Rahman, Sten Eriksson, Md Aminul Islam, and Abul Kalam Azad. Scheelite type $Sr_{1-x}Ba_xWO_4$ (x= 0.1, 0.2, 0.3) for possible application in solid oxide fuel cell electrolytes. *Scientific Reports*, 9(1):1–10, 2019.

[26] Jihai Cheng and Jianbo He. Electrical properties of scheelite structure ceramic electrolytes for solid oxide fuel cells. *Materials Letters*, 209:525–527, 2017.

[27] Yun Yuan, Yuhong Huang, Fei Ma, Zongquan Zhang, and Xiumei Wei. Effects of oxygen vacancy on the mechanical, electronic and optical properties of monoclinic BiVO$_4$. *Journal of Materials Science*, 52(14):8546–8555, Jul 2017.

[28] M. Muralidharan, V. Anbarasu, A. Elaya Perumal, and K. Sivakumar. Enhanced ferromagnetism in Cr doped SrMoO$_4$ scheelite structured compounds. *Journal of Materials Science: Materials in Electronics*, 27(3):2545–2556, Mar 2016.

[29] M. Muralidharan and K. Sivaji. Vacancy induced ferromagnetism in SrWO$_4$ and SrMoO$_4$ nano structured compounds. *AIP Conference Proceedings*, 2265(1):030584, 2020.

[30] Donglin Guo, Qi Yang, Hao Hua, and Chenguo Hu. Room temperature ferromagnetism in shuttle-like BaMoO$_4$ microcrystals. *The Journal of Physical Chemistry C*, 118(25):13826–13832, Jun 2014.

[31] Eliane Bsaibess, Fabian Delorme, Isabelle Monot-Laffez, and Fabien Giovannelli. Ultra-low thermal conductivity in scheelite and a-deficient scheelite ceramics. *Scripta Materialia*, 201:113950, 2021.

[32] Yuchen Liu, Dechang Jia, Yu Zhou, Yanchun Zhou, Juanli Zhao, Qian Li, and Bin Liu. Discovery of ABO$_4$ scheelites with the extra low thermal conductivity through high-throughput calculations. *Journal of Materiomics*, 6(4):702–711, 2020.

[33] Michael R. Winter and David R. Clarke. Oxide materials with low thermal conductivity. *Journal of the American Ceramic Society*, 90(2):533–540, 2007.

[34] Sydney F A Kettle. *Symmetry and structure: Readable group theory for chemists*. Wiley-Blackwell, Hoboken, NJ, 3 edition, 2007.

[35] Peter Atkins and Julio De Paula. *Atkins' physical chemistry*. Oxford University Press, London, England, 9 edition, 2010.

[36] David J Willock. *Molecular Symmetry*. Wiley-Blackwell, Hoboken, NJ, USA, 2009.

[37] Kieran C Molloy. *Group theory for chemists: Fundamental theory and applications*. Woodhead Publishing, Cambridge, England, 2 edition, 2010.

[38] Rakshit Ameta and Suresh C Ameta. *Chemical applications of symmetry and group theory*. Apple Academic Press, Oakville, MO, USA, 2016.

[39] NIST Standard Reference Database. Coblentz no.10116. `https://webbook.nist.gov/cgi/cbook.cgi?ID=C7732185&Units=SI&Type=IR-SPEC&Index=1#IR-SPEC`. Accessed: 2022-10-27.

[40] John R. Platt. 1966 nobel laureate in chemistry: Robert s. mulliken. *Science*, 154(3750):745–747, 1966.

[41] The nobel prize in chemistry 1966. `https://www.nobelprize.org/prizes/chemistry/1966/mulliken/facts/`. Accessed: 2022-11-23.

[42] Robert S. Mulliken. Spectroscopy, molecular orbitals, and chemical bonding. *Science*, 157(3784):13–24, 1967.

[43] Peter Atkins, Tina Overton, Jonathan Rourke, Mark Weller, and Fraser Armstrong. *Shriver and Atkins' inorganic chemistry*. Oxford University Press, London, England, 5 edition, 2009.

[44] James E. House. *Inorganic Chemistry*. Academic Press, San Diego, CA, 2007.

[45] Richard C Powell. *Symmetry, group theory, and the physical properties of crystals*. Springer, New York, NY, 2010 edition, 2010.

[46] Chris J Jones. *d- and f-Block Chemistry*. Royal Society of Chemistry, Cambridge, England, 2001.

[47] Leslie E Orgel. *Introduction to transition metal chemistry: Ligand field theory*. Methuen young books, London, England, 2 edition, 1966.

[48] Guillermo Gonzalez-Morago. *Cluster chemistry: Introduction to the chemistry of transition metal and main group element molecular clusters*. Springer, Berlin, Germany, 1993 edition, 1993.

[49] P. Hohenberg and W. Kohn. Inhomogeneous electron gas. *Phys. Rev.*, 136:B864–B871, Nov 1964.

[50] Giuseppe Grosso and Giuseppe Pastori Parravicini. *Solid State Physics*. Academic Press, San Diego, CA, 2 edition, 2013.

[51] W. Kohn and L. J. Sham. Self-consistent equations including exchange and correlation effects. *Phys. Rev.*, 140:A1133–A1138, Nov 1965.

[52] Feliciano Giustino. *Materials modelling using density functional theory: Properties and predictions*. Oxford University Press, London, England, 2014.

[53] Eberhard Engel and Reiner M Dreizler. *Density functional theory: An advanced course*. Springer, Berlin, Germany, 2011 edition, 2011.

[54] J Kubler, K H Hock, J Sticht, and A R Williams. Density functional theory of non-collinear magnetism. *Journal of Physics F: Metal Physics*, 18(3):469, mar 1988.

[55] J. P. Perdew and Alex Zunger. Self-interaction correction to density-functional approximations for many-electron systems. *Phys. Rev. B*, 23:5048–5079, May 1981.

[56] D. M. Ceperley and B. J. Alder. Ground state of the electron gas by a stochastic method. *Phys. Rev. Lett.*, 45:566–569, Aug 1980.

[57] David C. Langreth and M. J. Mehl. Beyond the local-density approximation in calculations of ground-state electronic properties. *Phys. Rev. B*, 28:1809–1834, Aug 1983.

[58] A. D. Becke. Density-functional exchange-energy approximation with correct asymptotic behavior. *Phys. Rev. A*, 38:3098–3100, Sep 1988.

[59] John P. Perdew, Kieron Burke, and Matthias Ernzerhof. Generalized gradient approximation made simple. *Phys. Rev. Lett.*, 77:3865–3868, Oct 1996.

[60] D. R. Hamann, M. Schlüter, and C. Chiang. Norm-conserving pseudopotentials. *Phys. Rev. Lett.*, 43:1494–1497, Nov 1979.

[61] P. E. Blöchl. Projector augmented-wave method. *Phys. Rev. B*, 50:17953–17979, Dec 1994.

[62] R. P. Feynman. Forces in molecules. *Phys. Rev.*, 56:340–343, Aug 1939.

[63] Jorge Nocedal and Stephen Wright. *Numerical Optimization*. Springer, New York, NY, 2 edition, 2006.

[64] Yihuang Xiong, Quinn T. Campbell, Julian Fanghanel, Catherine K. Badding, Huaiyu Wang, Nicole E. Kirchner-Hall, Monica J. Theibault, Iurii Timrov, Jared S. Mondschein, Kriti Seth, Rowan R. Katzbaer, Andrés Molina Villarino, Betül Pamuk, Megan E. Penrod, Mohammed M. Khan, Tiffany Rivera, Nathan C. Smith, Xavier Quintana, Paul Orbe, Craig J. Fennie, Senorpe Asem-Hiablie, James L. Young, Todd G. Deutsch, Matteo Cococcioni, Venkatraman Gopalan, Héctor D. Abruña, Raymond E. Schaak, and Ismaila Dabo. Optimizing accuracy and efficacy in data-driven materials discovery for the solar production of hydrogen. *Energy Environ. Sci.*, 14:2335–2348, 2021.

[65] Matteo Cococcioni and Stefano de Gironcoli. Linear response approach to the calculation of the effective interaction parameters in the lda + u method. *Phys. Rev. B*, 71:035105, Jan 2005.

[66] Iurii Timrov, Nicola Marzari, and Matteo Cococcioni. Hp – a code for the calculation of hubbard parameters using density-functional perturbation theory. *Computer Physics Communications*, 279:108455, 2022.

[67] Iurii Timrov, Nicola Marzari, and Matteo Cococcioni. Hubbard parameters from density-functional perturbation theory. *Phys. Rev. B*, 98:085127, Aug 2018.

[68] Andrea Benassi. *PWscf's epsilon.x user's manual*, 2014.

[69] Mark Fox. *Optical properties of solids*. Oxford University Press, London, England, 2 edition, 2010.

[70] For information about the thermo_pw software.

[71] R Hill. The elastic behaviour of a crystalline aggregate. *Proceedings of the Physical Society. Section A*, 65(5):349–354, may 1952.

[72] Woldemar Voigt. *Lehrbuch der kristallphysik:(mit ausschluss der kristalloptik)*, volume 34. BG Teubner, 1910.

[73] András Reuß. Berechnung der fließgrenze von mischkristallen auf grund der plastizitätsbedingung für einkristalle. *ZAMM-Journal of Applied Mathematics and Mechanics/Zeitschrift für Angewandte Mathematik und Mechanik*, 9(1):49–58, 1929.

[74] S.F. Pugh. Xcii. relations between the elastic moduli and the plastic properties of polycrystalline pure metals. *The London, Edinburgh, and Dublin Philosophical Magazine and Journal of Science*, 45(367):823–843, 1954.

[75] Xing-Qiu Chen, Haiyang Niu, Dianzhong Li, and Yiyi Li. Modeling hardness of polycrystalline materials and bulk metallic glasses. *Intermetallics*, 19(9):1275–1281, 2011.

[76] Orson L. Anderson. A simplified method for calculating the debye temperature from elastic constants. *Journal of Physics and Chemistry of Solids*, 24(7):909–917, 1963.

[77] Gerald D Mahan. *Condensed matter in a nutshell*. Princeton University Press, Princeton, NJ, 2010.

[78] David R. Clarke and Simon R. Phillpot. Thermal barrier coating materials. *Materials Today*, 8(6):22–29, 2005.

[79] David R. Clarke. Materials selection guidelines for low thermal conductivity thermal barrier coatings. *Surface and Coatings Technology*, 163-164:67–74, 2003. Proceedings of the 29th International conference on Metallurgical Coatings and Thin Films.

[80] G.A. Slack. Nonmetallic crystals with high thermal conductivity. *Journal of Physics and Chemistry of Solids*, 34(2):321–335, 1973.

[81] V. N. Belomestnykh. The acoustical grüneisen constants of solids. *Technical Physics Letters*, 30(2):91–93, Feb 2004.

[82] B. D. Sanditov, Sh. B. Tsydypov, and D. S. Sanditov. Relation between the grüneisen constant and poisson's ratio of vitreous systems. *Acoustical Physics*, 53(5):594–597, Sep 2007.

[83] Donald T. Morelli and Glen A. Slack. *High Lattice Thermal Conductivity Solids*, pages 37–68. Springer New York, New York, NY, 2006.

[84] P. G. Klemens. Thermal resistance due to point defects at high temperatures. *Phys. Rev.*, 119:507–509, Jul 1960.

[85] J.C. Sczancoski, L.S. Cavalcante, N.L. Marana, R.O. da Silva, R.L. Tranquilin, M.R. Joya, P.S. Pizani, J.A. Varela, J.R. Sambrano, M. Siu Li, E. Longo, and J. Andrés. Electronic structure and optical properties of $BaMoO_4$ powders. *Current Applied Physics*, 10(2):614 – 624, 2010.

[86] S.N. Achary, S.J. Patwe, A. Vishwanath, Sourabh Wajhal, P.S.R. Krishna, and A.K. Tyagi. Evolution of crystal structure of $PbMoO_4$ between 5 and 300 k: A low temperature powder neutron diffraction study. *Materials Chemistry and Physics*, 260:124111, 2021.

[87] Robert M. Hazen, Larry W. Finger, and Joseph W.E. Mariathasan. High-pressure crystal chemistry of scheelite-type tungstates and molybdates. *Journal of Physics and Chemistry of Solids*, 46(2):253 – 263, 1985.

[88] C Lugli, L Medici, and D Saccardo. Natural wulfenite: structural refinement by single-crystal x-ray diffraction. *Neues Jahrbuch fur Mineralogie*, 6:281–288, 1999.

[89] Paolo Giannozzi, Stefano Baroni, Nicola Bonini, Matteo Calandra, Roberto Car, Carlo Cavazzoni, Davide Ceresoli, Guido L Chiarotti, Matteo Cococcioni, Ismaila Dabo, Andrea Dal Corso, Stefano de Gironcoli, Stefano Fabris, Guido Fratesi, Ralph Gebauer, Uwe Gerstmann, Christos Gougoussis, Anton Kokalj, Michele Lazzeri, Layla Martin-Samos, Nicola Marzari, Francesco Mauri, Riccardo Mazzarello, Stefano Paolini, Alfredo Pasquarello, Lorenzo Paulatto, Carlo Sbraccia, Sandro Scandolo, Gabriele Sclauzero, Ari P Seitsonen, Alexander Smogunov, Paolo Umari, and Renata M Wentzcovitch. QUANTUM ESPRESSO: a modular and open-source software project for quantum simulations of materials. *Journal of Physics: Condensed Matter*, 21(39):395502, sep 2009.

[90] P Giannozzi, O Andreussi, T Brumme, O Bunau, M Buongiorno Nardelli, M Calandra, R Car, C Cavazzoni, D Ceresoli, M Cococcioni, N Colonna, I Carnimeo, A Dal Corso, S de Gironcoli, P Delugas, R A DiStasio, A Ferretti, A Floris, G Fratesi, G Fugallo, R Gebauer, U Gerstmann, F Giustino, T Gorni, J Jia, M Kawamura, H-Y Ko, A Kokalj, E Küçükbenli, M Lazzeri, M Marsili, N Marzari, F Mauri, N L Nguyen, H-V Nguyen, A Otero de-la Roza, L Paulatto, S Poncé, D Rocca, R Sabatini, B Santra, M Schlipf, A P Seitsonen, A Smogunov, I Timrov, T Thonhauser, P Umari, N Vast, X Wu, and S Baroni. Advanced capabilities for materials modelling with quantum ESPRESSO. *Journal of Physics: Condensed Matter*, 29(46):465901, oct 2017.

[91] Andrea Dal Corso. Pseudopotentials periodic table: From H to Pu. *Computational Materials Science*, 95:337–350, 2014.

[92] F.A. Kröger and H.J. Vink. Relations between the concentrations of imperfections in crystalline solids. volume 3 of *Solid State Physics*, pages 307–435. Academic Press, 1956.

[93] Kevin J. May and Alexie M. Kolpak. Improved description of perovskite oxide crystal structure and electronic properties using self-consistent hubbard u corrections from acbn0. *Phys. Rev. B*, 101:165117, Apr 2020.

[94] Okan K. Orhan and David D. O'Regan. First-principles hubbard u and hund's j corrected approximate density functional theory predicts an accurate fundamental gap in rutile and anatase TiO_2. *Phys. Rev. B*, 101:245137, Jun 2020.

[95] Hendrik J. Monkhorst and James D. Pack. Special points for brillouin-zone integrations. *Phys. Rev. B*, 13:5188–5192, Jun 1976.

[96] Antoine A. Emery and Chris Wolverton. High-throughput dft calculations of formation energy, stability and oxygen vacancy formation energy of ABO_3 perovskites. *Scientific Data*, 4(1):170153, Oct 2017.

[97] Ya-Nan Zhu, Gan-Hong Zheng, Zhen-Xiang Dai, Jing-Jing Mu, and Zi-Fen Yao. Monodisperse $SrMoO_4$ nanocrystals: Synthesis, luminescence and photocatalysis. *Journal of Materials Science & Technology*, 33(8):834–842, 2017.

[98] Sharin Maria Thomas, S. Balamurugan, S.A. Ashika, and T.K. Sana Fathima. Microstructural, thermal, and optical properties of nanostructured $CaMoO_4$ materials screened under different processes. *Results in Chemistry*, page 100823, 2023.

[99] M. Isik, N.M. Gasanly, N.H. Darvishov, and V.E. Bagiev. Structural and temperature-tuned band gap energy characteristics of $PbMoO_4$ single crystals. *Optical Materials*, 126:112210, 2022.

[100] S. P. S. Porto and J. F. Scott. Raman spectra of $CaWO_4$, $SrWO_4$, $CaMoO_4$, and $CaMoO_4$. *Phys. Rev.*, 157:716–719, May 1967.

[101] T.T Basiev, A.A Sobol, Yu.K Voronko, and P.G Zverev. Spontaneous raman spectroscopy of tungstate and molybdate crystals for raman lasers. *Optical Materials*, 15(3):205–216, 2000.

[102] Nidhi Khobragade, Ela Sinha, S.K. Rout, and Manoranjan Kar. Structural, optical and microwave dielectric properties of $Sr_{1-x}Ca_xWO_4$ ceramics prepared by the solid state reaction route. *Ceramics International*, 39(8):9627–9635, 2013.

[103] En-Cai Xiao, Qi Ren, Zhikai Cao, Gang Dou, Ze-Ming Qi, and Feng Shi. Phonon characteristics and intrinsic properties of phase-pure $CaMoO_4$ microwave dielectric ceramic. *Journal of Materials Science: Materials in Electronics*, 31(7):5686–5691, Apr 2020.

[104] R. A. P. Ribeiro, E. Longo, J. Andrés, and S. R. de Lazaro. A dft investigation of the role of oxygen vacancies on the structural, electronic and magnetic properties of $ATiO_3$ (A = Mn, Fe, Ni) multiferroic materials. *Phys. Chem. Chem. Phys.*, 20:28382–28392, 2018.

[105] A. L. Companion and M. A. Komarynsky. Crystal field splitting diagrams. *Journal of Chemical Education*, 41(5):257, May 1964.

[106] Yonas B. Abraham, N. A. W. Holzwarth, R. T. Williams, G. Eric Matthews, and Alan R. Tackett. Electronic structure of oxygen-related defects in $PbWO_4$ and $CaMoO_4$ crystals. *Phys. Rev. B*, 64:245109, Dec 2001.

[107] Ze Wang, Tingyu Liu, Huanhuan Liu, and Zijiang Yang. First-principles calculations study of small polarons around oxygen vacancies in $SrMoO_4$. *Journal of Electronic Materials*, Jan 2023.

[108] Ali Gholami and Mahnaz Maddahfar. Synthesis and characterization of barium molybdate nanostructures with the aid of amino acids and investigation of its photocatalytic degradation of methyl orange. *Journal of Materials Science: Materials in Electronics*, 27(7):6773–6778, 2016.

[109] Schindra Kumar Ray, Dipesh Dhakal, and Soo Wohn Lee. Insight into sulfamethoxazole degradation, mechanism, and pathways by $AgBr - BaMoO_4$ composite photocatalyst. *Journal of Photochemistry and Photobiology A: Chemistry*, 364:686–695, 2018.

[110] Jorge Oliva, Ernesto Valadez-Renteria, Yuwaraj K Kshetri, Armando Encinas, Soo Wohn Lee, and Vicente Rodriguez-Gonzalez. A sustainable composite of rice-paper/bamoo4 nanoparticles for the photocatalytic elimination of the recalcitrant 2, 6-dichlorobenzamide (bam) pesticide in drinking water and its mechanisms of degradation. *Environmental Science and Pollution Research*, pages 1–15, 2022.

[111] W. L. Bond. Measurement of the refractive indices of several crystals. *Journal of Applied Physics*, 36(5):1674–1677, 1965.

[112] Jean G. Berny, Jacques P. Bourgoin, and Bernard Ayrault. Dispersion des indices de refraction du molybdate de plomb ($PbMoO_4$) et de la paratellurite (TeO_2). *Optics Communications*, 6(4):383–387, 1972.

[113] Yufei Xue, Dong Tian, Chunhua Zeng, Yunchang Fu, and Kongzhai Li. Effect of fe doping concentration on photocatalytic performance of CeO_2 from dft insight into analysis. *AIP Advances*, 9(12):125341, 2019.

[114] Yufei Xue, Dong Tian, Dexin Zhang, Chunhua Zeng, Yunchang Fu, Kongzhai Li, Hua Wang, and Yafang Tian. The mechanism of photocatalyst and the effects of co-doping CeO_2 on refractive index and reflectivity from dft calculation. *Computational Materials Science*, 158:197–208, 2019.

[115] Dong Tian, Kongzhai Li, Yonggang Wei, Xing Zhu, Chunhua Zeng, Xianming Cheng, Yane Zheng, and Hua Wang. Dft insights into oxygen vacancy formation and CH_4 activation over CeO_2 surfaces modified by transition metals (Fe, Co and Ni). *Physical Chemistry Chemical Physics*, 20(17):11912–11929, 2018.

[116] Miso Lee, Yong Youn, Kanghoon Yim, and Seungwu Han. High-throughput ab initio calculations on dielectric constant and band gap of non-oxide dielectrics. *Scientific Reports*, 8(1):14794, Oct 2018.

[117] Eung Soo Kim, Byung Sam Chun, Robert Freer, and Robert J. Cernik. Effects of packing fraction and bond valence on microwave dielectric properties of $A_2^+B_6^+O_4$ (A_2^+: Ca, Pb, Ba; B_6^+: Mo, W) ceramics. *Journal of the European Ceramic Society*, 30(7):1731–1736, 2010.

[118] Félix Mouhat and François-Xavier Coudert. Necessary and sufficient elastic stability conditions in various crystal systems. *Phys. Rev. B*, 90:224104, Dec 2014.

[119] J M Farley, G A Saunders, and D Y Chung. Elastic properties of scheelite structure molybdates and tungstates. *Journal of Physics C: Solid State Physics*, 8(6):780, mar 1975.

[120] N. Najafvandzadeh, S. López-Moreno, D. Errandonea, P. Pavone, and C. Draxl. First-principles study of elastic and thermal properties of scheelite-type molybdates and tungstates. *Materials Today Communications*, 24:101089, 2020.

[121] Vinod Panchal, Nandini Garg, and Surinder M Sharma. Raman and x-ray diffraction investigations on $BaMoO_4$ under high pressures. *Journal of Physics: Condensed Matter*, 18(16):3917, apr 2006.

[122] Daniel Errandonea, Ravhi S. Kumar, Xinghua Ma, and Chaoyang Tu. High-pressure x-ray diffraction study of $SrMoO_4$ and pressure-induced structural changes. *Journal of Solid State Chemistry*, 181(2):355–364, 2008.

[123] V. Panchal, N. Garg, H. K. Poswal, D. Errandonea, P. Rodríguez-Hernández, A. Muñoz, and E. Cavalli. High-pressure behavior of $CaMoO_4$. *Phys. Rev. Mater.*, 1:043605, Sep 2017.

[124] Xingcheng Wang, Guoxiang Zhang, Qi Sun, Zihao Fei, and Yuanyu Wang. New insight into effects of oxygen vacancies on crystal structure and electrical properties of barium titanate dielectric ceramic. *Journal of Solid State Chemistry*, 320:123859, 2023.

[125] R.P. Thompson and W.J. Clegg. Predicting whether a material is ductile or brittle. *Current Opinion in Solid State and Materials Science*, 22(3):100–108, 2018.

[126] J Haines, JM Léger, and G Bocquillon. Synthesis and design of superhard materials. *Annual Review of Materials Research*, 31(1):1–23, 2001.

[127] Masao Morishita, Motohiro Fukushima, and Hiroki Houshiyama. Third law entropy of barium molybdate. *MATERIALS TRANSACTIONS*, 57(1):46–51, 2016.

[128] Masao Morishita and Hiroki Houshiyama. The third law entropy of strontium molybdates. *MATERIALS TRANSACTIONS*, 56(4):545–549, 2015.

[129] A.E. Musikhin, V.N. Naumov, M.A. Bespyatov, and V.N. Shlegel. Heat capacity and thermodynamic functions of camoo4 at low temperatures. *Journal of Alloys and Compounds*, 655:165–171, 2016.

[130] D. A. Pinnow, L. G. Van Uitert, A. W. Warner, and W. A. Bonner. Lead molybdate: A melt-grown crystal with a high figure of merit for acousto-optic device applications. *Applied Physics Letters*, 15(3):83–86, 1969.

[131] Giovanni Pizzi, Dmitri Volja, Boris Kozinsky, Marco Fornari, and Nicola Marzari. Boltzwann: A code for the evaluation of thermoelectric and electronic transport properties with a maximally-localized wannier functions basis. *Computer Physics Communications*, 185(1):422–429, 2014.

[132] Giovanni Pizzi, Valerio Vitale, Ryotaro Arita, Stefan Blügel, Frank Freimuth, Guillaume Géranton, Marco Gibertini, Dominik Gresch, Charles Johnson, Takashi Koretsune, Julen Ibañez-Azpiroz, Hyungjun Lee, Jae-Mo Lihm, Daniel Marchand, Antimo Marrazzo, Yuriy Mokrousov, Jamal I Mustafa, Yoshiro Nohara, Yusuke Nomura, Lorenzo Paulatto, Samuel Poncé, Thomas Ponweiser, Junfeng Qiao, Florian Thöle, Stepan S Tsirkin, Małgorzata Wierzbowska, Nicola Marzari, David Vanderbilt, Ivo Souza, Arash A Mostofi, and Jonathan R Yates. Wannier90 as a community code: new features and applications. *Journal of Physics: Condensed Matter*, 32(16):165902, jan 2020.

[133] M. Böhm, O. Erb, and A. Scharmann. Electrical conduction in $PbMoO_4$ crystals. *physica status solidi (a)*, 84(1):291–299, 1984.

[134] S. K. Arora and G. S. Trivikrama Rao. Electrical conductivity of $BaMoO_4$ single crystals. *Crystal Research and Technology*, 17(10):1303–1305, 1982.

[135] G. D. Mahan. Figure of merit for thermoelectrics. *Journal of Applied Physics*, 65(4):1578–1583, 1989.

[136] J. O. Sofo and G. D. Mahan. Optimum band gap of a thermoelectric material. *Phys. Rev. B*, 49:4565–4570, Feb 1994.

[137] G D Mahan and J O Sofo. The best thermoelectric. *Proceedings of the National Academy of Sciences*, 93(15):7436–7439, 1996.

[138] George M. Hale and Marvin R. Querry. Optical constants of water in the 200-nm to 200-μm wavelength region. *Appl. Opt.*, 12(3):555–563, Mar 1973.

MOLECULAR SYMMETRY APPENDIX

A.1 Molecular symmetry

The image below, taken from Ref. [34], shows the systematic approach to classifying the point group of a molecule using the Schönflies notation.
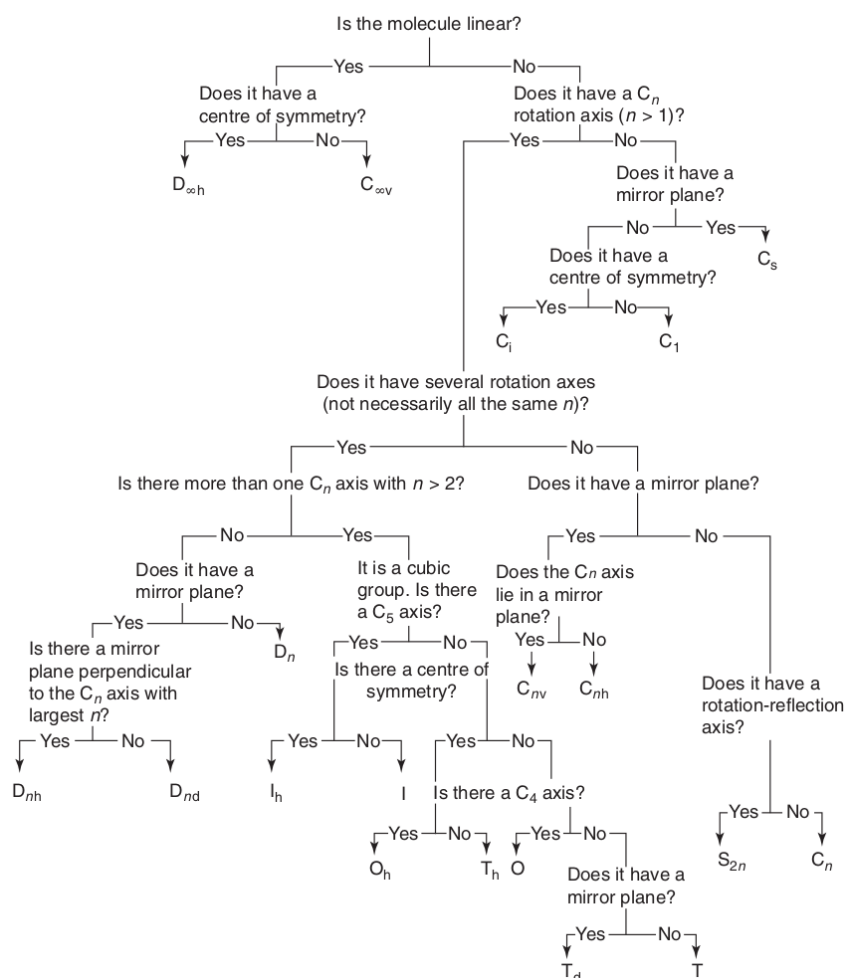
Figure A.1 - Scheme for determining the point group of a molecule.

A.2   Group theory

Table A.1 - B_1 irreducible representation for C_{2v} point group.

C_{2v}	E	$C_2(z)$	$\sigma_v(xz)$	$\sigma_v(yz)$	linear function
B_1	+1	-1	+1	-1	x
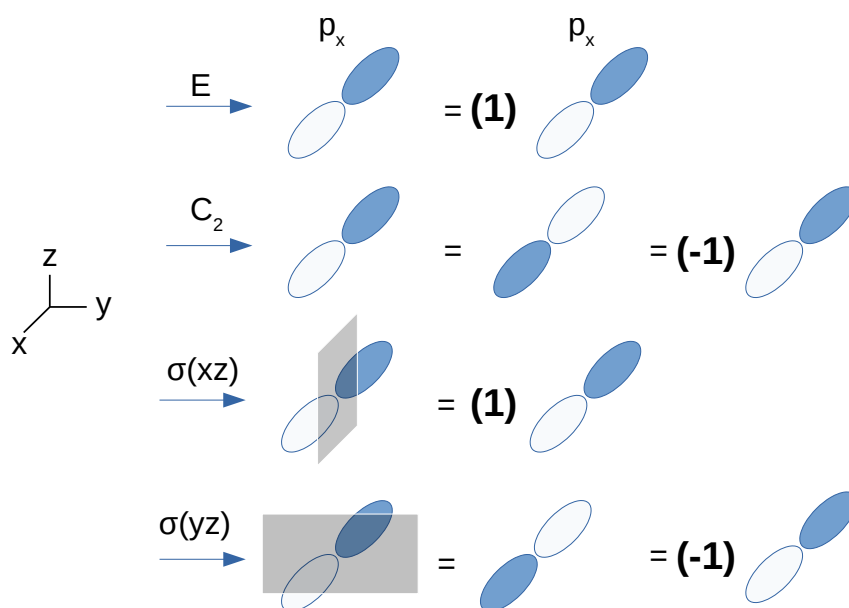
Figure A.2 - The scheme for obtaining the characters in B_1 symmetry that is associated with the linear function p_x. The numbers in parenthesis are the characters in respective symmetry operations.

Table A.2 - A_1 irreducible representation for C_{2v} point group.

C_{2v}	E	$C_2(z)$	$\sigma_v(xz)$	$\sigma_v(yz)$	linear function
A_1	+1	+1	+1	+1	z
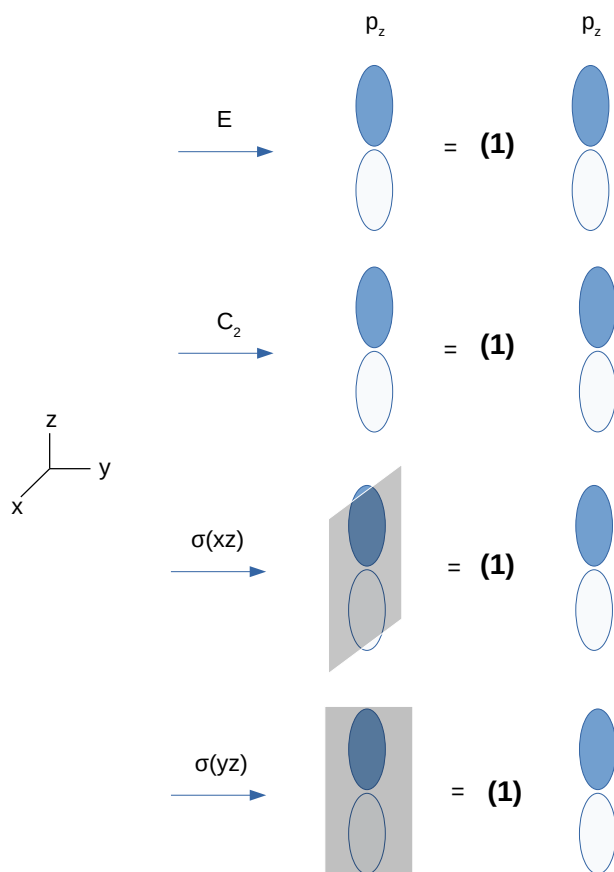
Figure A.3 - The scheme for obtaining the characters in A_1 symmetry that is associated with the linear function p_z. The numbers in parenthesis are the characters in respective symmetry operations.

A.3   Vibrational modes
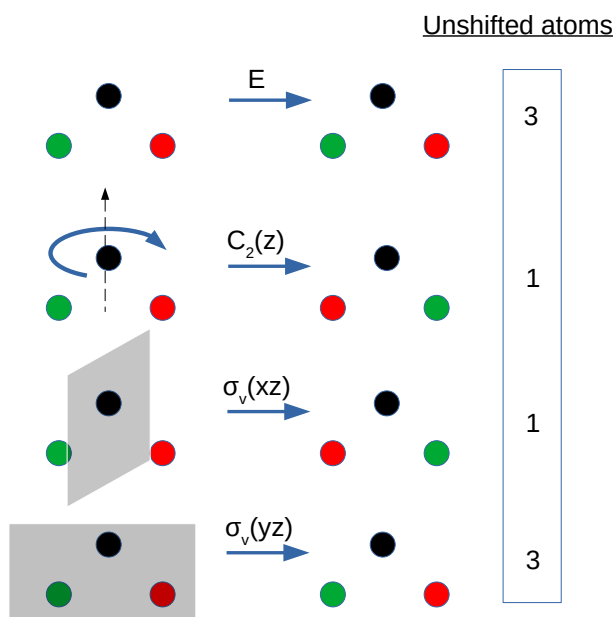
Figure A.4 - Unshifted atoms in C_{2v} point group.

Table A.3 - C_{2v} character table.

C_{2v}	E	$C_2(z)$	$\sigma_v(xz)$	$\sigma_v(yz)$
A_1	+1	+1	+1	+1
A_2	+1	+1	-1	-1
B_1	+1	-1	+1	-1
B_2	+1	-1	-1	+1

Table A.4 - Γ_{3N} characters.

C_{2v}	E	$C_2(z)$	$\sigma_v(xz)$	$\sigma_v(yz)$
Γ_{3N}	9	-1	+1	3

$$a_i = \frac{1}{h}\sum (n_R \chi_{(R)} \chi_{(IR)}), \tag{A.1}$$

$$
\begin{aligned}
A_1 &= \frac{1}{4}[(1.1.9)+(1.1.\text{-}1)+(1.1.1)+(1.1.3)] = 3 \\
A_2 &= \frac{1}{4}[(1.1.9)+(1.1.\text{-}1)+(1.\text{-}1.1)+(1.\text{-}1.3)] = 1 \\
B_1 &= \frac{1}{4}[(1.1.9)+(1.\text{-}1.\text{-}1)+(1.1.1)+(1.\text{-}1.3)] = 2 \\
B_2 &= \frac{1}{4}[(1.1.9)+(1.\text{-}1.\text{-}1)+(1.\text{-}1.1)+(1.1.3)] = 3
\end{aligned}
\tag{A.2}
$$

$$\Gamma_{3N} = 3A_1 + A_2 + 2B_1 + 3B_2 \tag{A.3}$$

$$
\begin{aligned}
\Gamma_{3N} &= \Gamma_T + \Gamma_R + \Gamma_{\text{vib}} \\
\Gamma_{\text{vib}} &= \Gamma_{3N} - \Gamma_T - \Gamma_R \\
\Gamma_{\text{vib}} &= 3A_1 + A_2 + 2B_1 + 3B_2 - A_1 - B_1 - B_2 - A_2 - B_1 - B_2 \\
\Gamma_{\text{vib}} &= 2A_1 + B_2.
\end{aligned}
\tag{A.4}
$$

A.4 Electric dipole selection rule

Table A.5 - Final state of a_1 symmetry.

A_1	1	1	1	1
A_1	1	1	1	1
A_1	1	1	1	1
$A_1 \otimes A_1 \otimes A_1$	1	1	1	1

Table A.6 - Final state of a_1 symmetry.

A_1	1	1	1	1
A_1	1	1	1	1
B_1	1	-1	1	-1
$A_1 \otimes A_1 \otimes B_1$	1	-1	1	-1

$$A_1 = \frac{1}{4}\left[(1.1.1) + (1.1.(-1)) + (1.1.1) + (1.1.(-1))\right] = 0.$$

Therefore, not allowed.

Table A.7 - Final state of a_1 symmetry.

A_1	1	1	1	1
A_1	1	1	1	1
B_2	1	-1	-1	1
$A_1 \otimes A_1 \otimes B_2$	1	-1	-1	1

Table A.8 - Final state of a_1 symmetry.

A_1	1	1	1	1
B_1	1	-1	1	-1
A_1	1	1	1	1
$A_1 \otimes B_1 \otimes A_1$	1	-1	1	-1

Table A.9 - Final state of a_1 symmetry.

A_1	1	1	1	1
B_1	1	-1	1	-1
B_2	1	-1	-1	1
$A_1 \otimes B_1 \otimes B_2$	1	1	-1	-1

$$A_1 = \frac{1}{4}\left[(1.1.1) + (1.1.1) + (1.1.(-1)) + (1.1.(-1))\right] = 0.$$

Therefore, not allowed.

Table A.10 - Final state of a_1 symmetry.

A_1	1	1	1	1
B_2	1	-1	-1	1
A_1	1	1	1	1
$A_1 \otimes B_2 \otimes A_1$	1	-1	-1	1

Table A.11 - Final state of a_1 symmetry.

A_1	1	1	1	1
B_2	1	-1	-1	1
B_2	1	-1	-1	1
$A_1 \otimes B_2 \otimes B_2$	1	1	1	1

Table A.12 - Final state of a_1 symmetry.

A_1	1	1	1	1
B_2	1	-1	-1	1
B_1	1	-1	1	-1
$A_1 \otimes B_2 \otimes B_1$	1	1	-1	-1

The Refractive index of water within the range of 200 nm and 200 μm is measured by 1.33 [138]. DFT calculations have found a value of 1.30, corroborating the accurate description of the water molecule calculated in this example. However, it required the assumption of LO-TO splitting in those calculations. Below, it shows the index of refraction behavior from one water molecule without considering LO-TO splitting. Once again, it has been viewed the character of the selection rule in the distinct maximum values for each incident polarization.
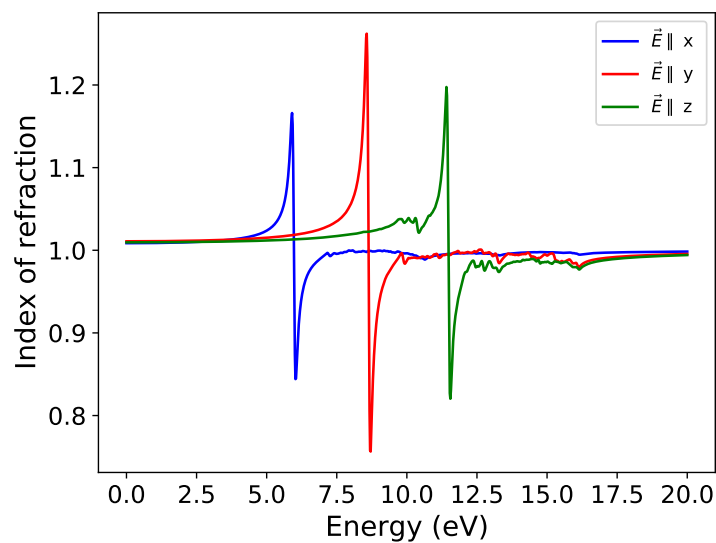
Figure A.5 - The index of refraction of water was calculated through the DFT technique.

MOLIBDATES DESCRIPTION AND COMPUTATIONAL DETAILS APPENDIX

B.1   Computational details
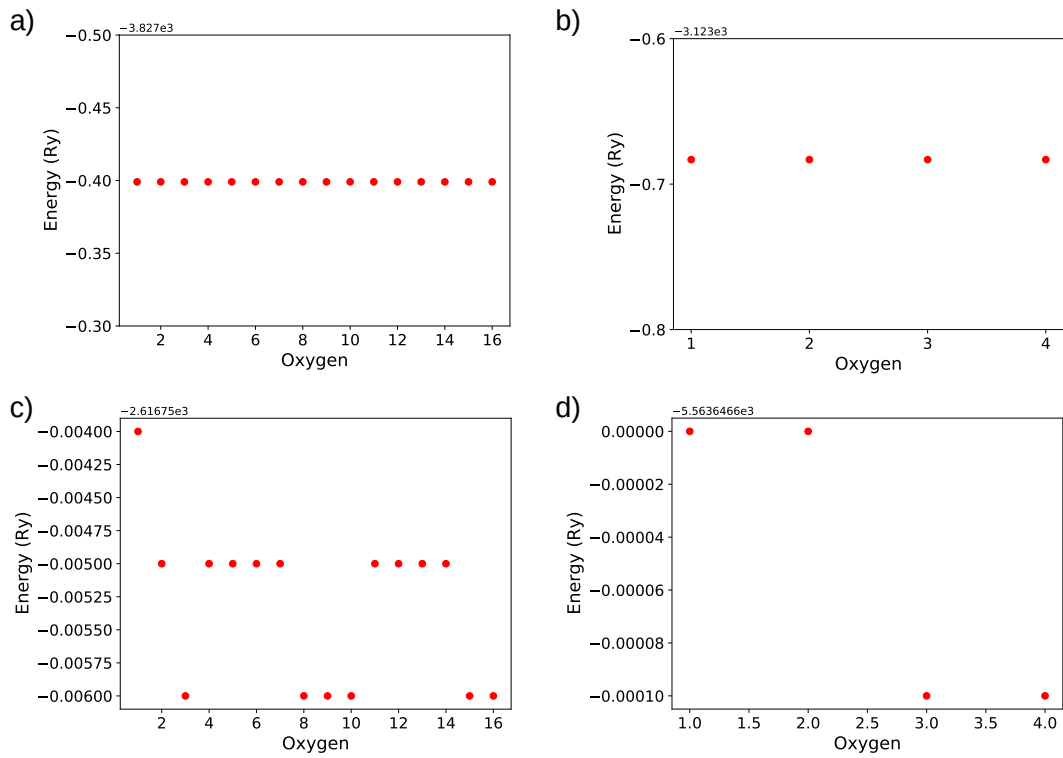
Figure B.1 - Ground state energy of the molybdates varying the position of the oxygen to be removed. From a)-d) we have BaMoO$_4$-$V_O^\times$, SrMoO$_4$-$V_O^\times$, CaMoO$_4$-$V_O^\times$ and PbMoO$_4$-$V_O^\times$, respectively. The produced data confirms that there is not much difference related to the choice of oxygen.
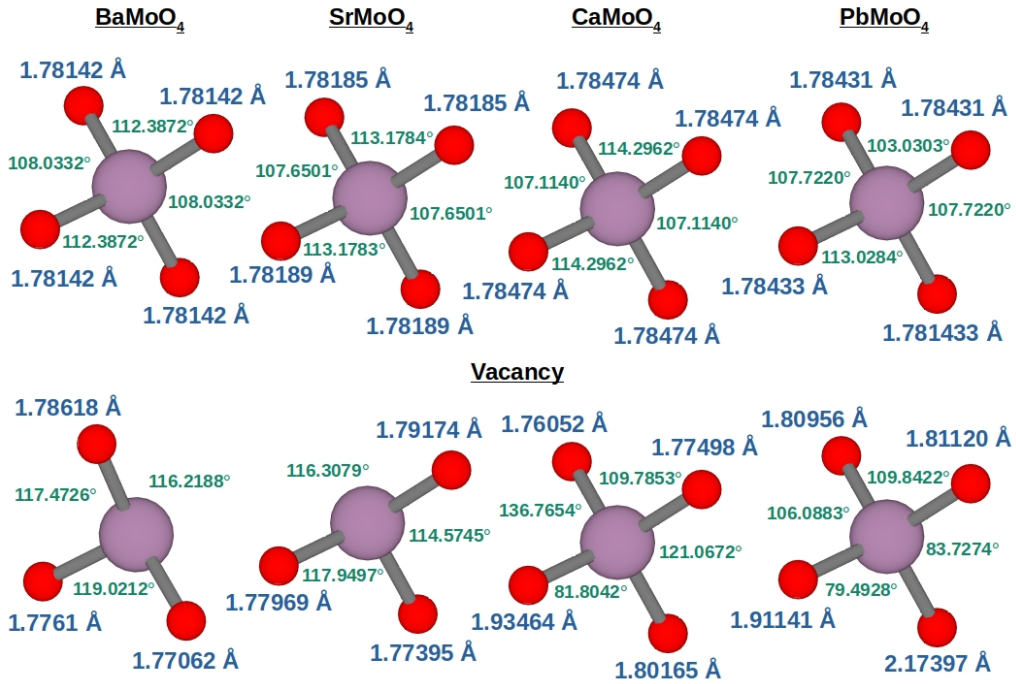
Figure B.2 - All molybdates [MoO$_4$] cluster bond length and angles.

Table B.1 - Lattice parameter 'A' convergence test.

Material	Lattice parameter (Å)	Volume (Å^3)	Tot magnetization (μ_B)
BaMoO$_4 - V_0^\times$	5.45	354.404	-0.12
	5.50	364.248	0.12
	5.55	374.273	-0.12
	5.60	384.479	2.00
	5.65	394.870	2.00
	5.70	405.447	2.00
SrMoO$_4 - V_0^\times$	4.90	266.232	0.07
	4.95	274.465	1.59
	5.00	282.866	2.00
	5.40	356.331	2.00
CaMoO$_4 - V_0^\times$	5.20	317.881	0.14
	5.25	327.139	0.15
	5.55	376.134	1.99
	5.60	386.486	1.99
PbMoO$_4 - V_0^\times$	4.75	239.433	0.00
	5.00	279.263	1.99
	5.45	361.654	2.00
	5.80	435.901	2.00
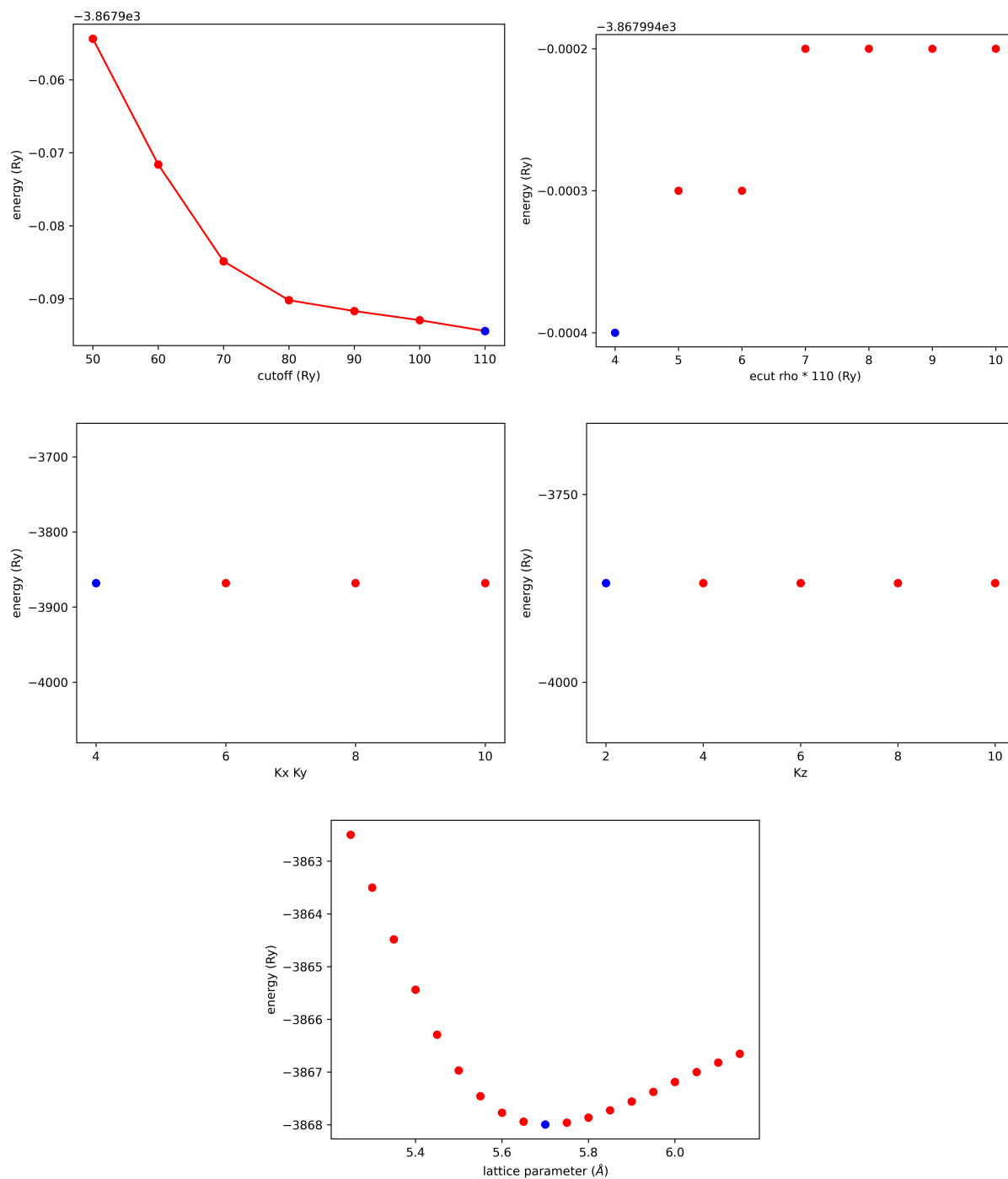
Figure B.3 - BaMoO$_4$ inputs optimization.
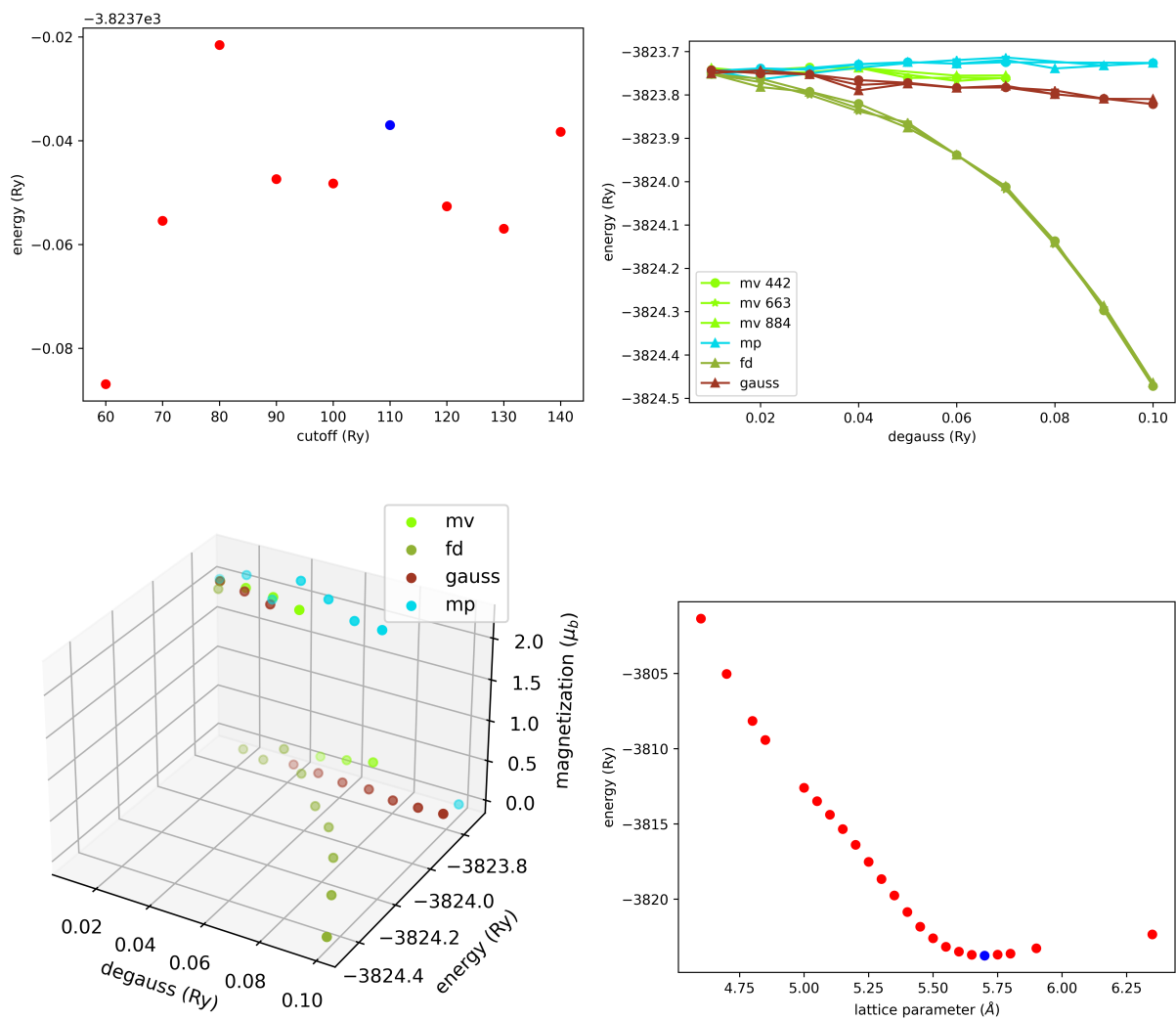
Figure B.4 - BaMoO$_4$ vacancy inputs optimization.
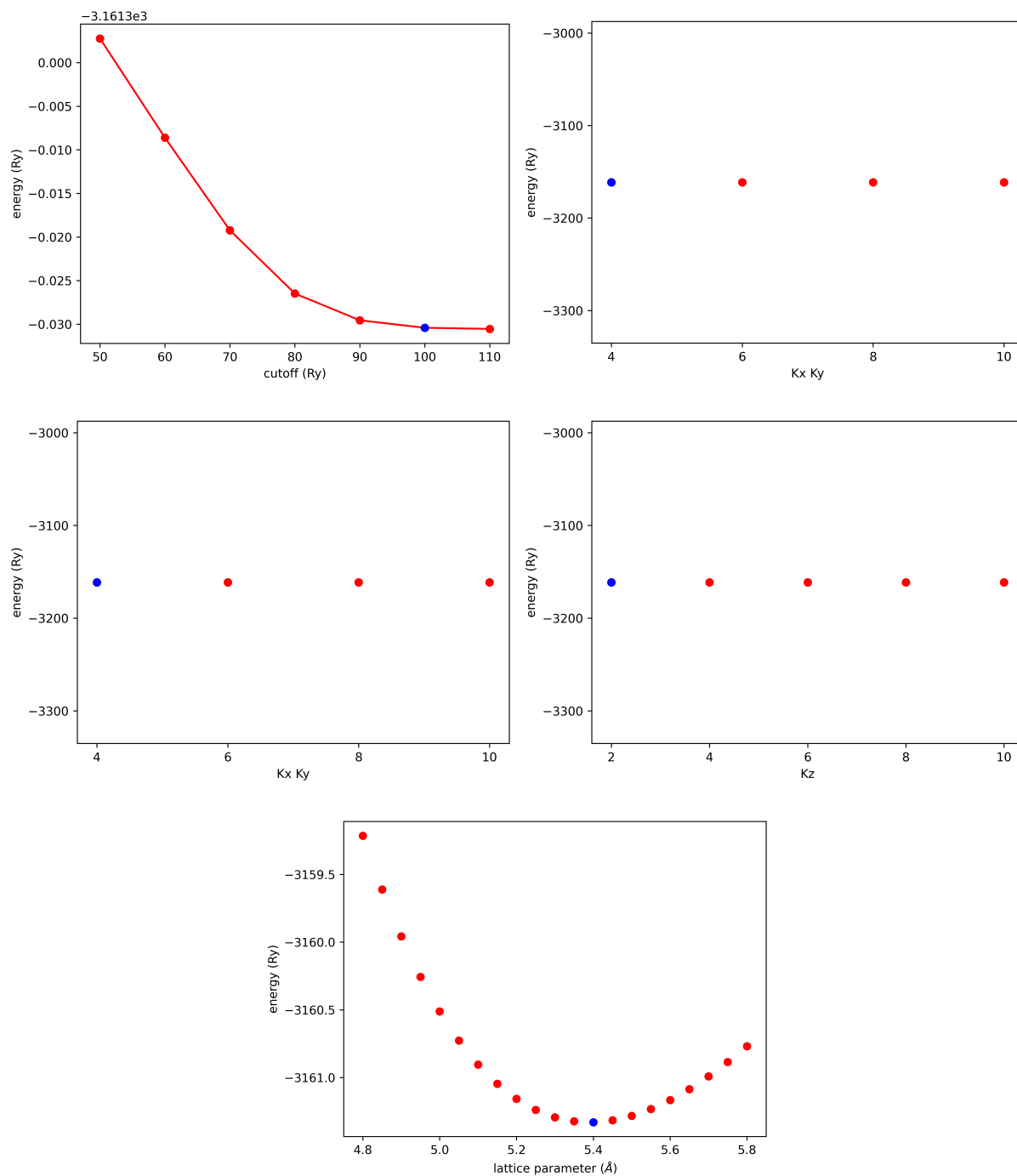
Figure B.5 - SrMoO$_4$ inputs optimization.
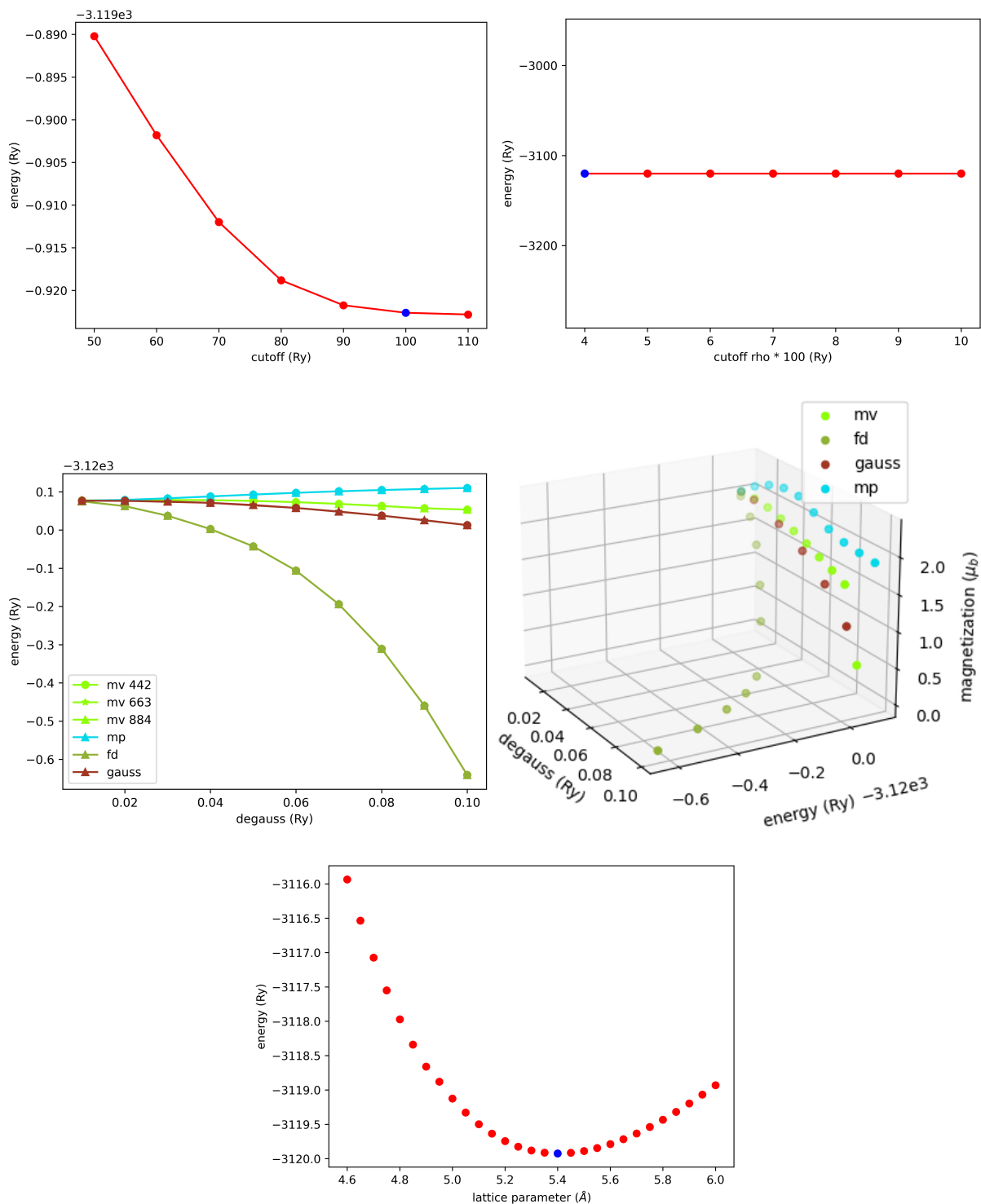
Figure B.6 - SrMoO$_4$ vacancy inputs optimization.
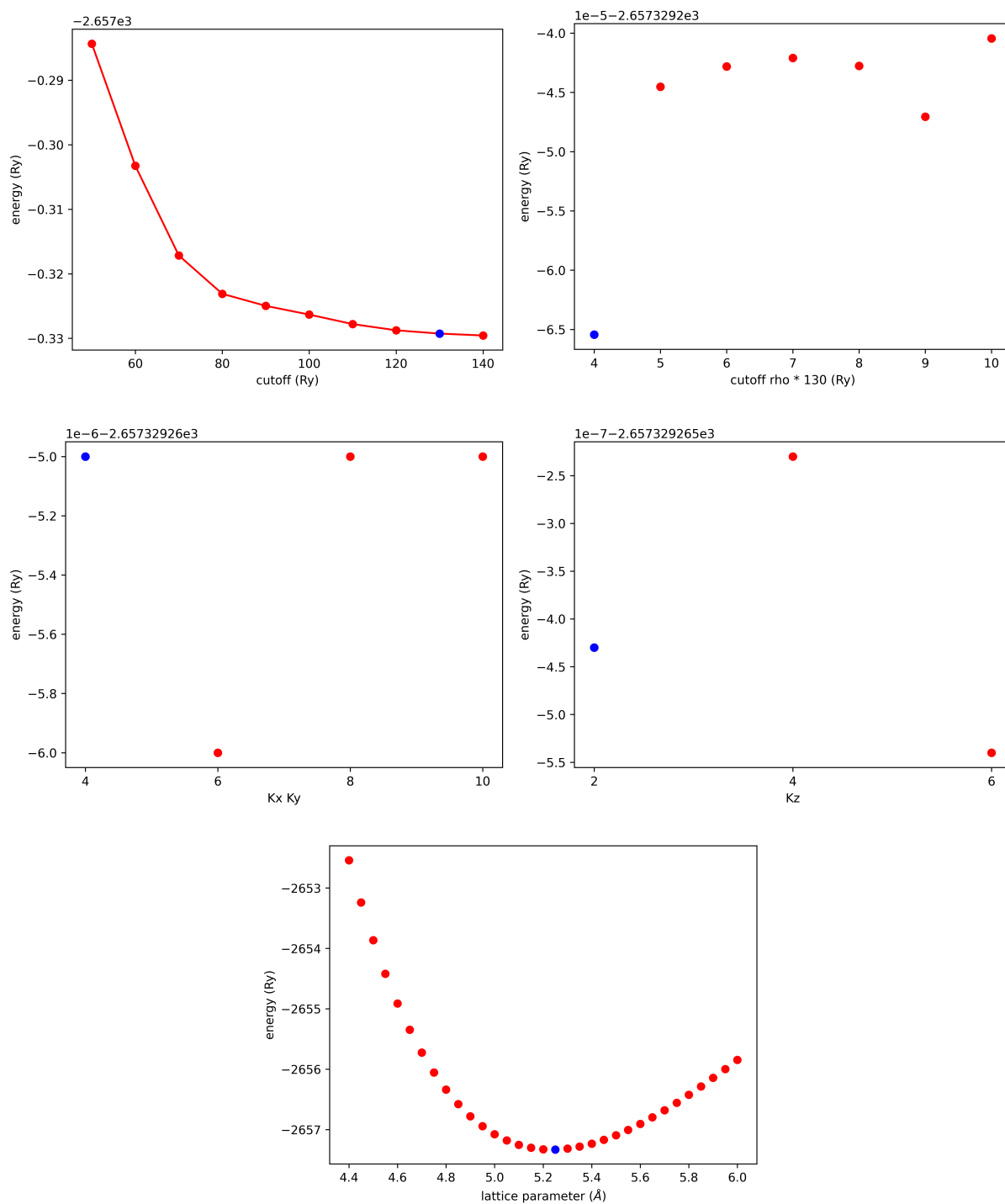
Figure B.7 - CaMoO$_4$ inputs optimization.
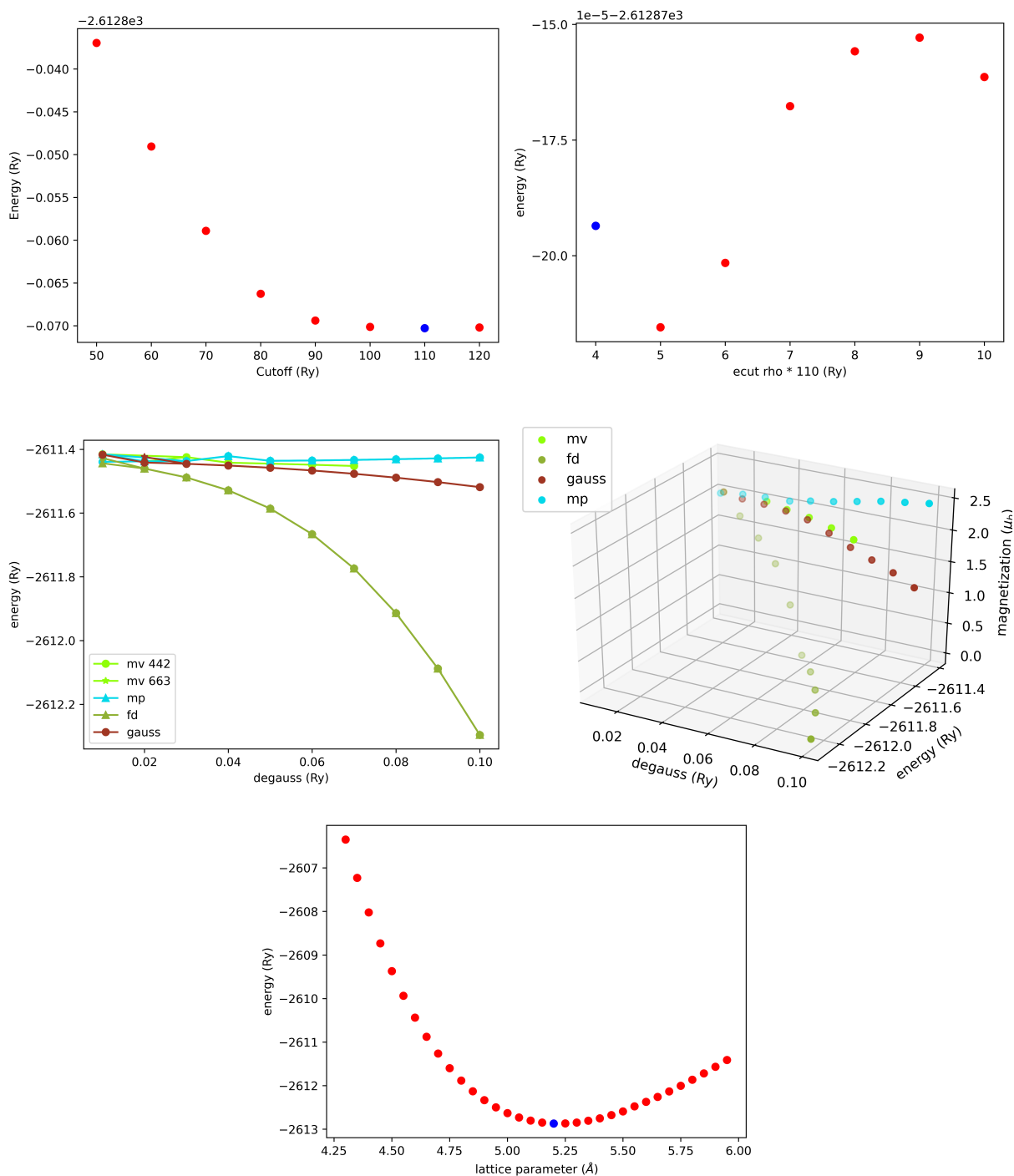
Figure B.8 - CaMoO$_4$ vacancy inputs optimization.
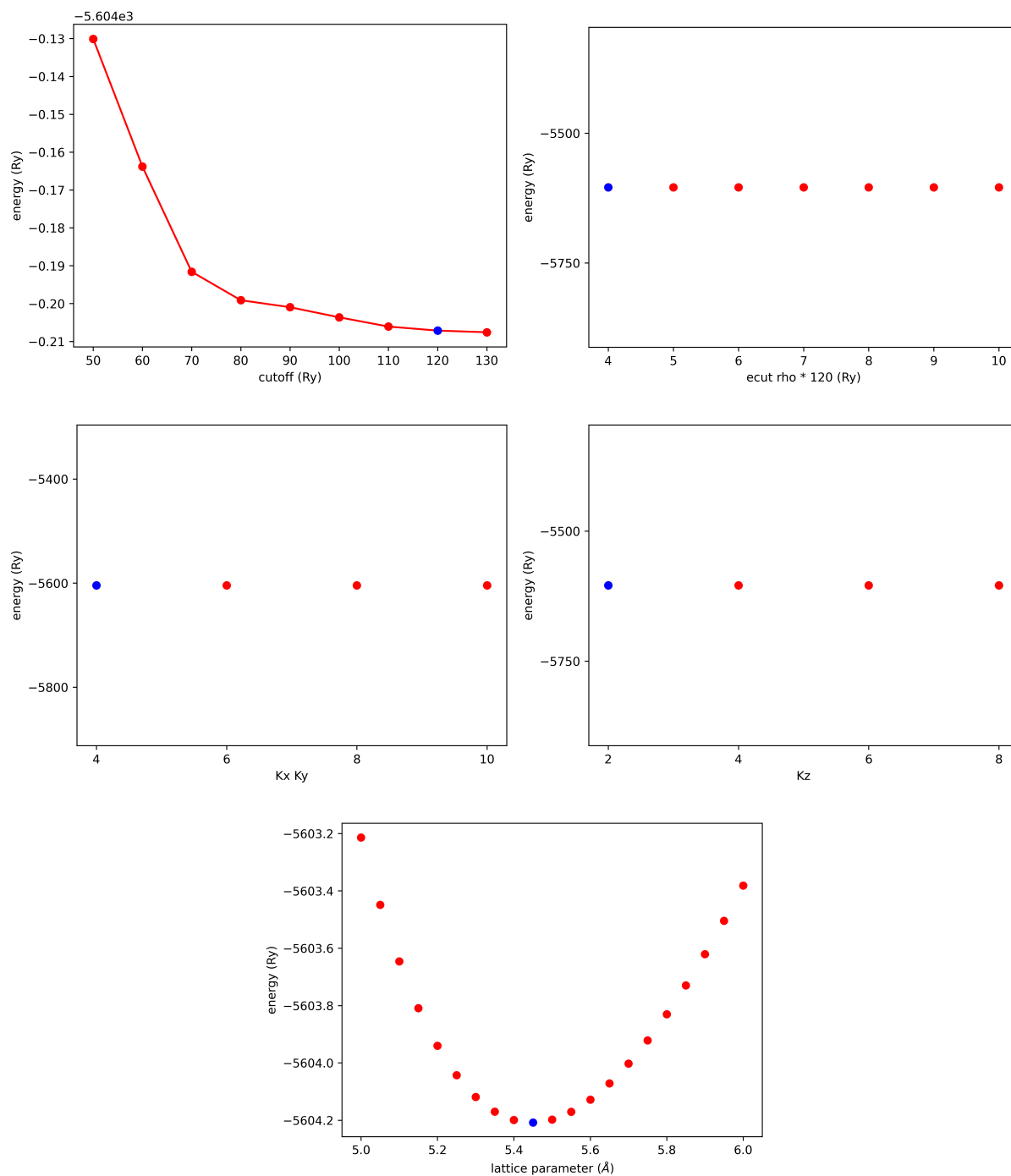
Figure B.9 - PbMoO$_4$ inputs optimization.
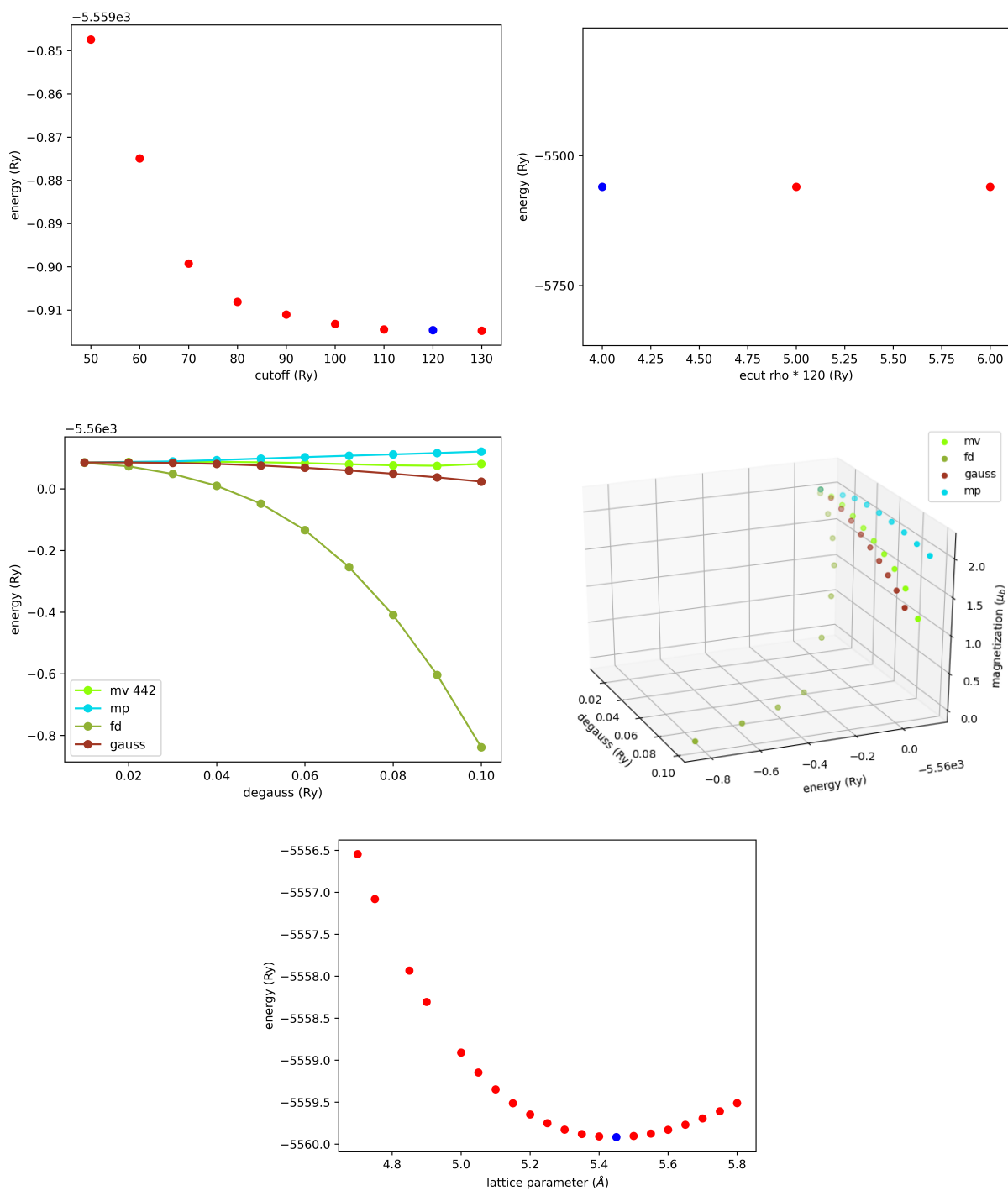
Figure B.10 - PbMoO$_4$ vacancy inputs optimization.

ELECTRONIC AND OPTICAL PROPERTIES OF MOLYBDATES APPENDIX

C.1 Electronic
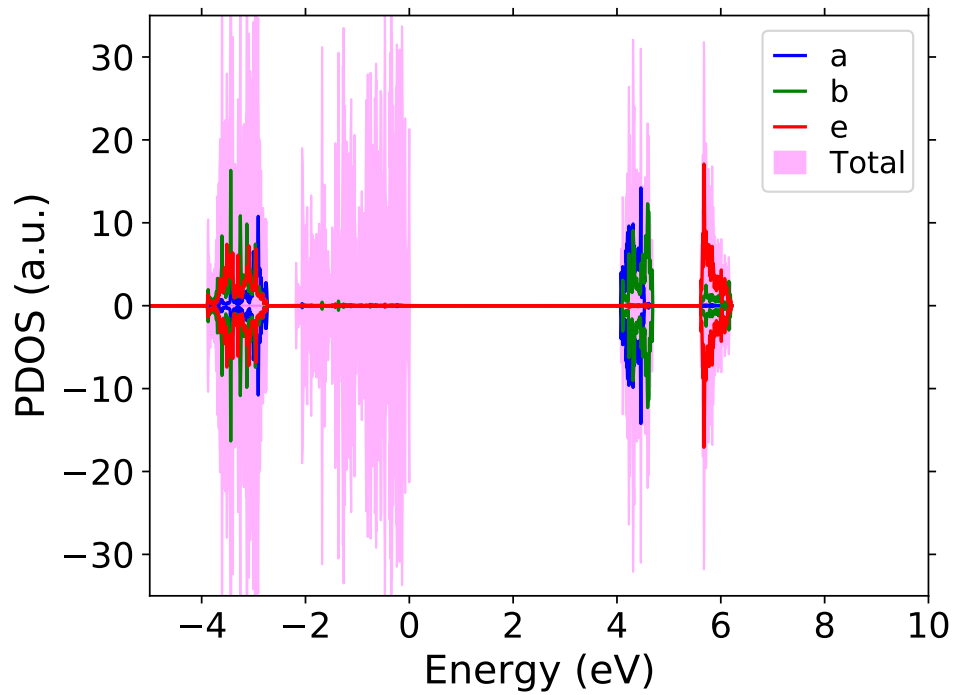
Figure C.1 - PDOS of $BaMoO_4$ in terms of its crystal field with symmetry S_4.
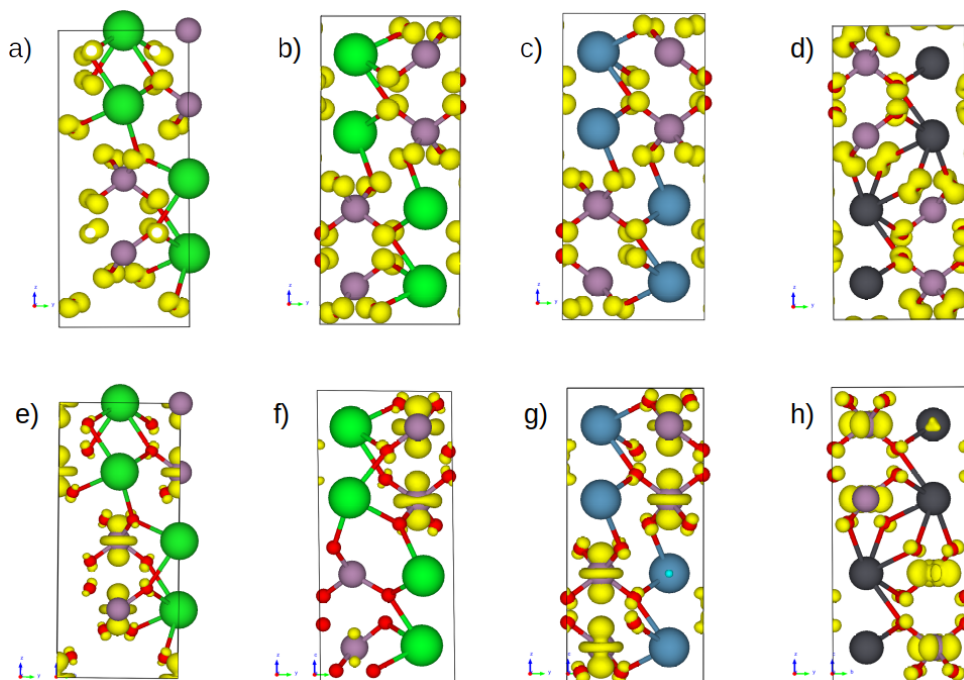
Figure C.2 - Orbtials from $BaMoO_4$, $SrMoO_4$, $CaMoO_4$, and $PbMoO_4$ are shown in first, second, third and fourth column, respectively. In rows from a) to d), we see the valence bands; from e) to h), the conduction bands.
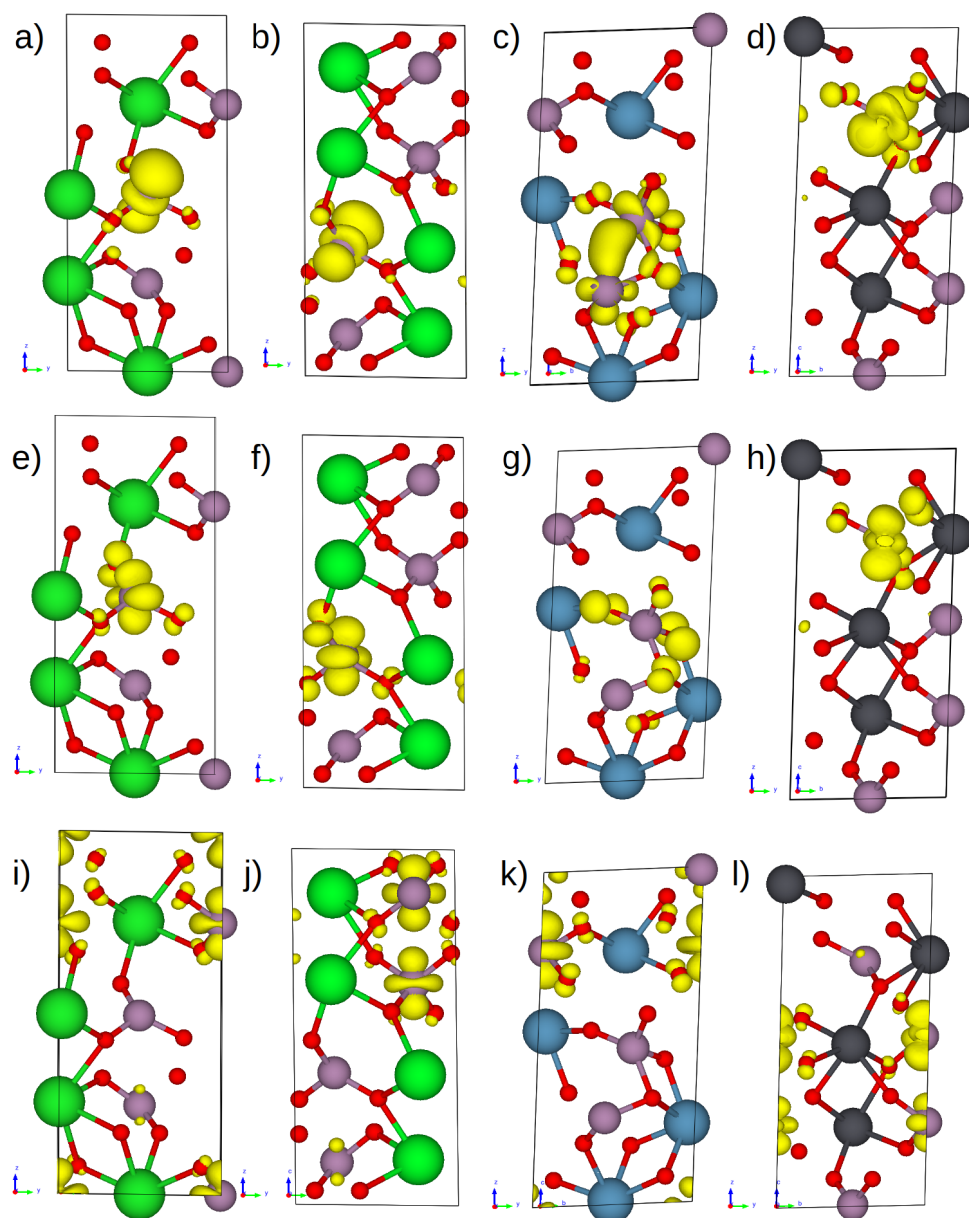
Figure C.3 - Orbtials from $BaMoO_4$-$V_0^{\times}$, $SrMoO_4$-$V_0^{\times}$, $CaMoO_4$-$V_0^{\times}$, and $PbMoO_4$-$V_0^{\times}$ are shown in first, second, third and fourth column, respectively. In rows from a) to d), we see the valence bands; from e) to h), the bands below the valence; and from i) to l), the conduction bands.

C.2   Optics

Table C.1 - Simplified T_d character table. LF stands for linear functions and QF for quadratic functions.

T_d	E	$8C_3$	$3C_2$	$6S_4$	$6\sigma_d$	LF	QF
A_1	1	1	1	1	1	-	$x^2 + y^2 + z^2$
A_2	1	1	1	1	-1	-	-
E	2	-1	2	0	0	-	$x^- y^2, z^2$
T_1	3	0	-1	1	-1	R_x, R_y, R_z	-
T_2	3	0	-1	-1	1	$(x, y.z)$	(xz, yz, xy)

Table C.2 - Simplified S_4 character table. LF stands for linear functions and QF for quadratic functions.

S_4	E	$2S_4$	C_2	LF	QF
A	1	1	1	R_z	z^2
B	1	-1	1	z	$x^2 - y^2, xy$
E	2	0	-2	(x, y)	(xz, yz)
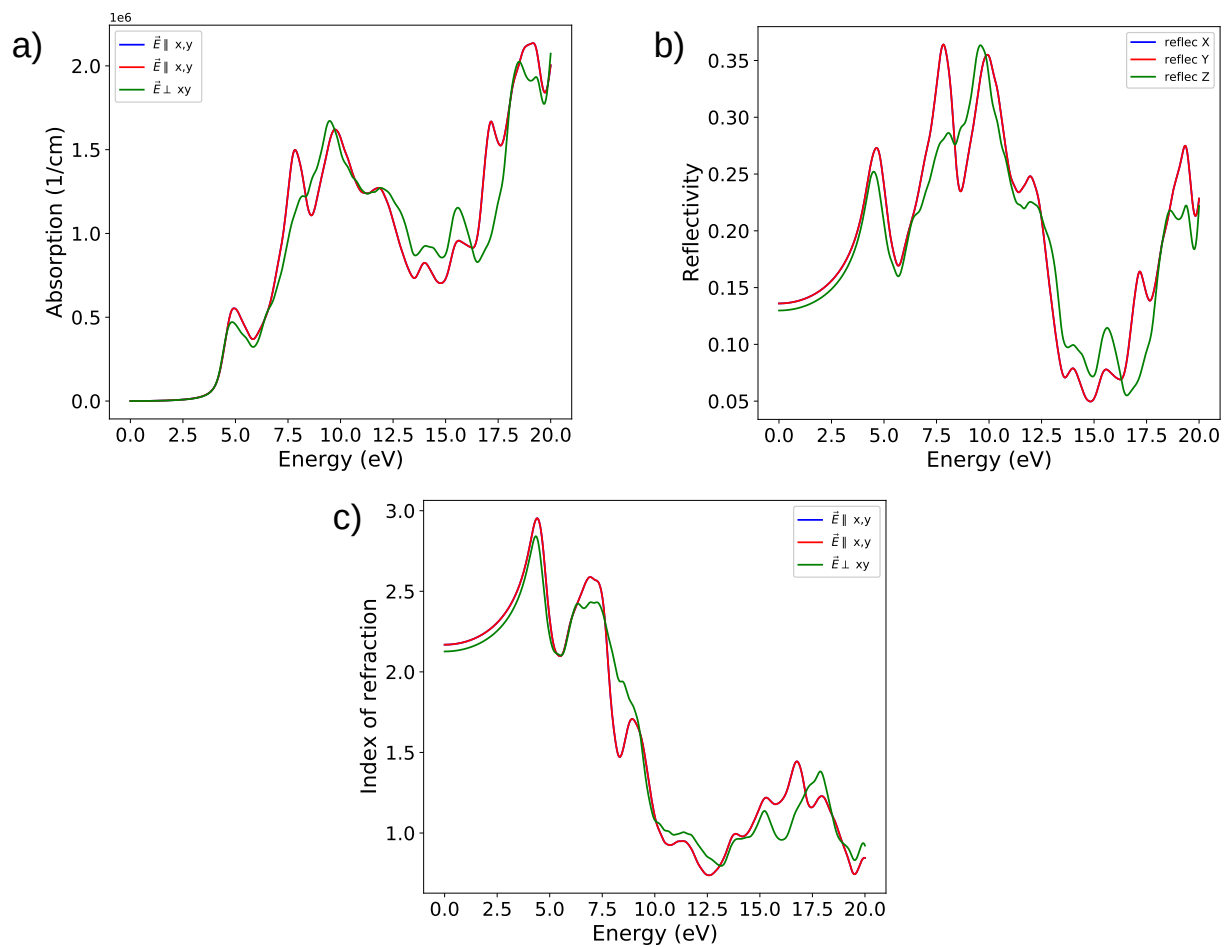
Figure C.4 - Absorption, a), reflectivity, b), and index of refraction spectra for BaMoO$_4$.
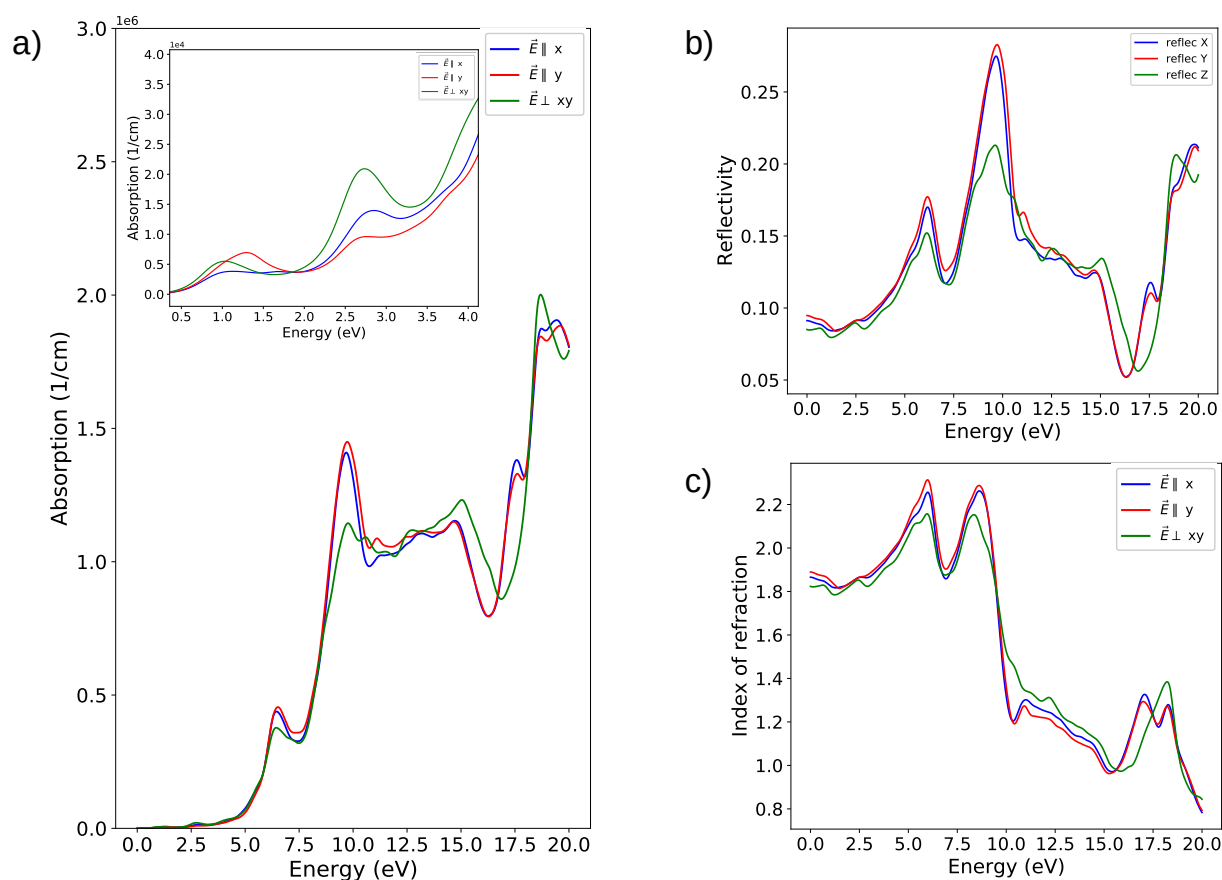
Figure C.5 - Absorption, a), reflectivity, b), and index of refraction spectra for BaMoO$_4$-$V_0^{\times}$.
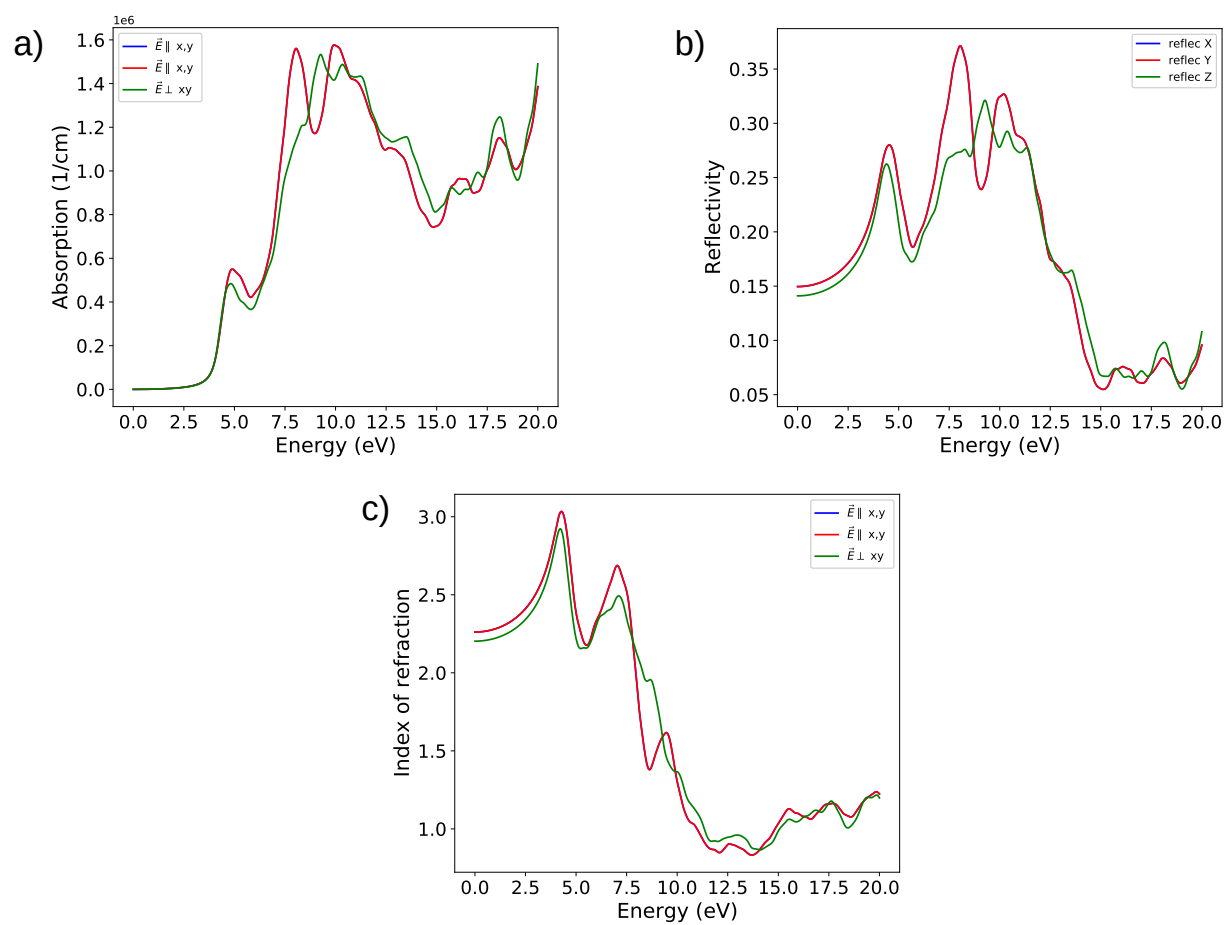
Figure C.6 - Absorption, a), reflectivity, b), and index of refraction spectra for $SrMoO_4$.
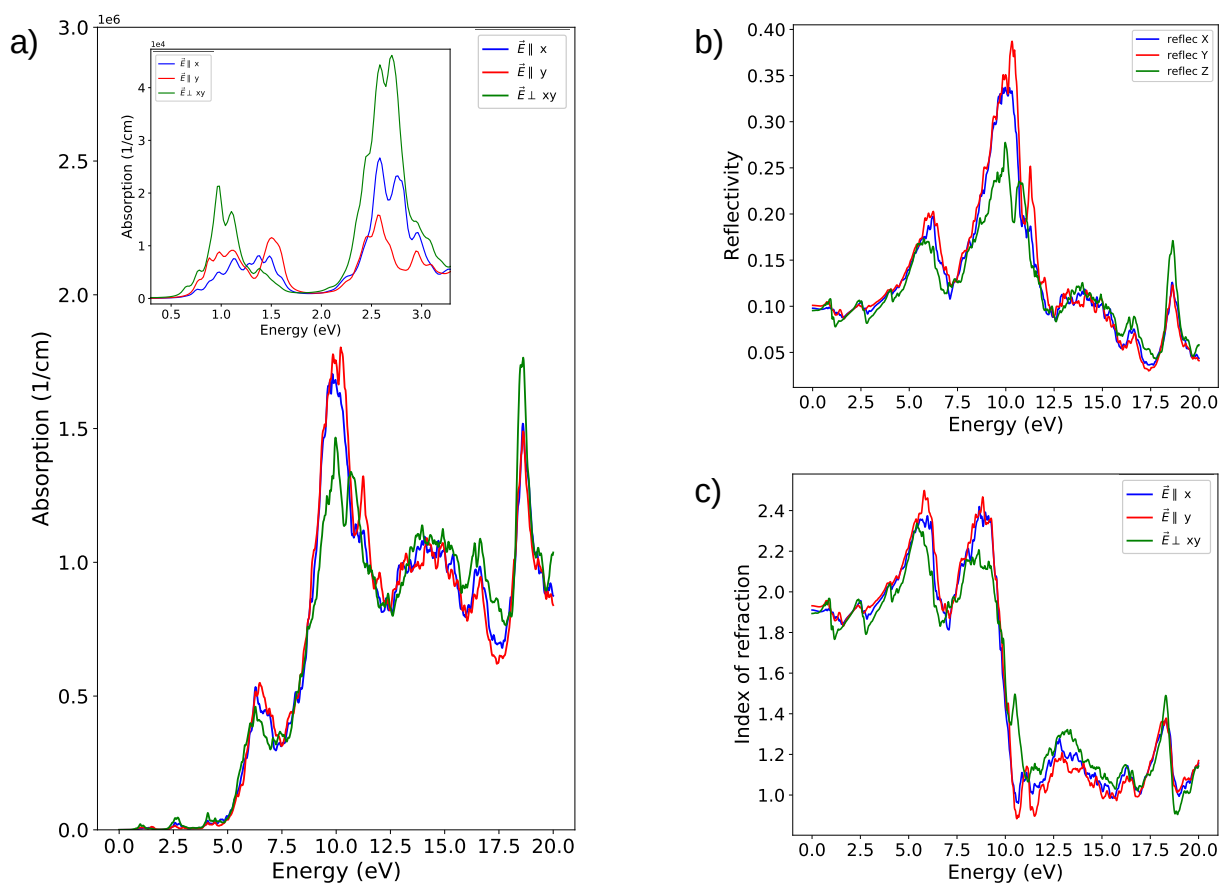
Figure C.7 - Absorption, a), reflectivity, b), and index of refraction spectra for SrMoO$_4$-$V_0^\times$.
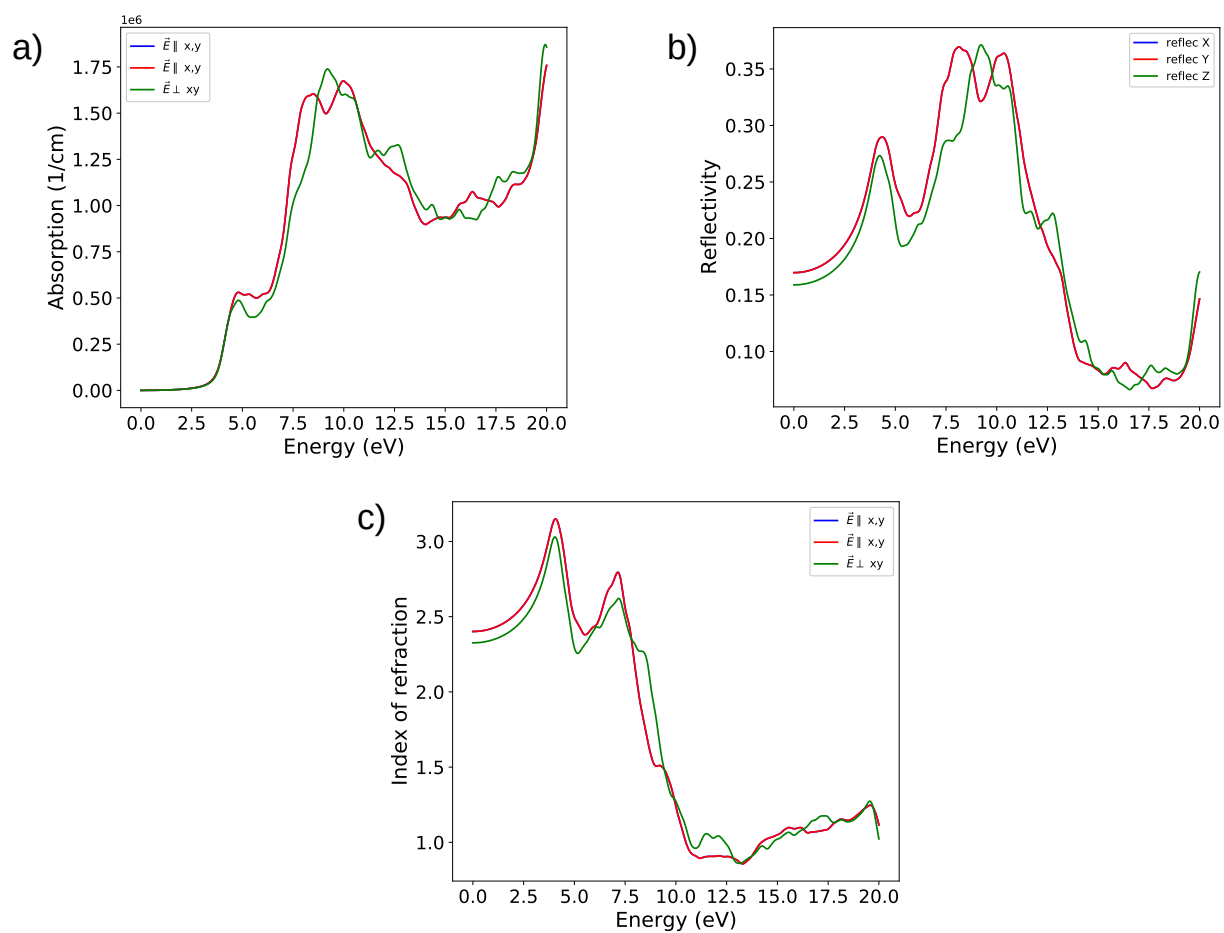
Figure C.8 - Absorption, a), reflectivity, b), and index of refraction spectra for CaMoO$_4$.
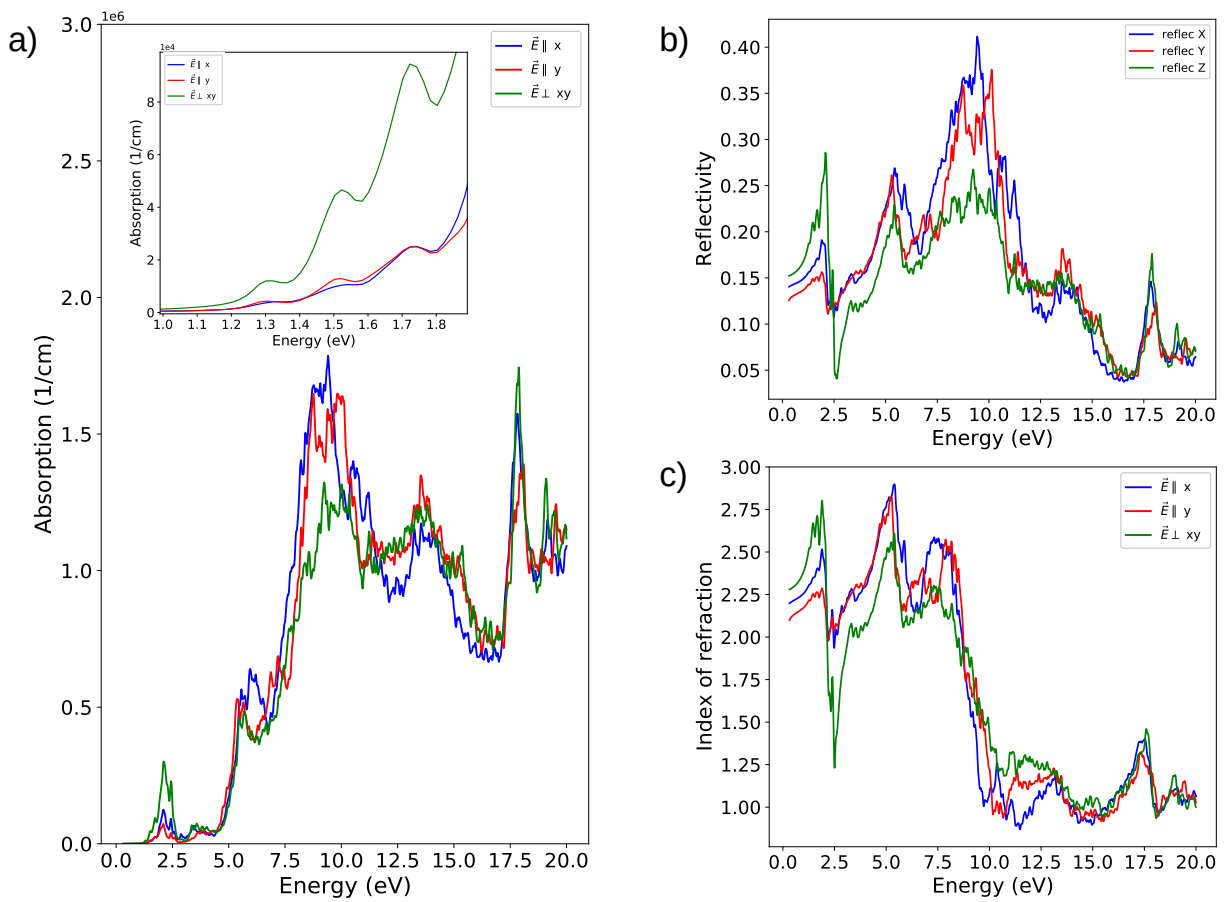
Figure C.9 - Absorption, a), reflectivity, b), and index of refraction spectra for $CaMoO_4$-$V_0^\times$.
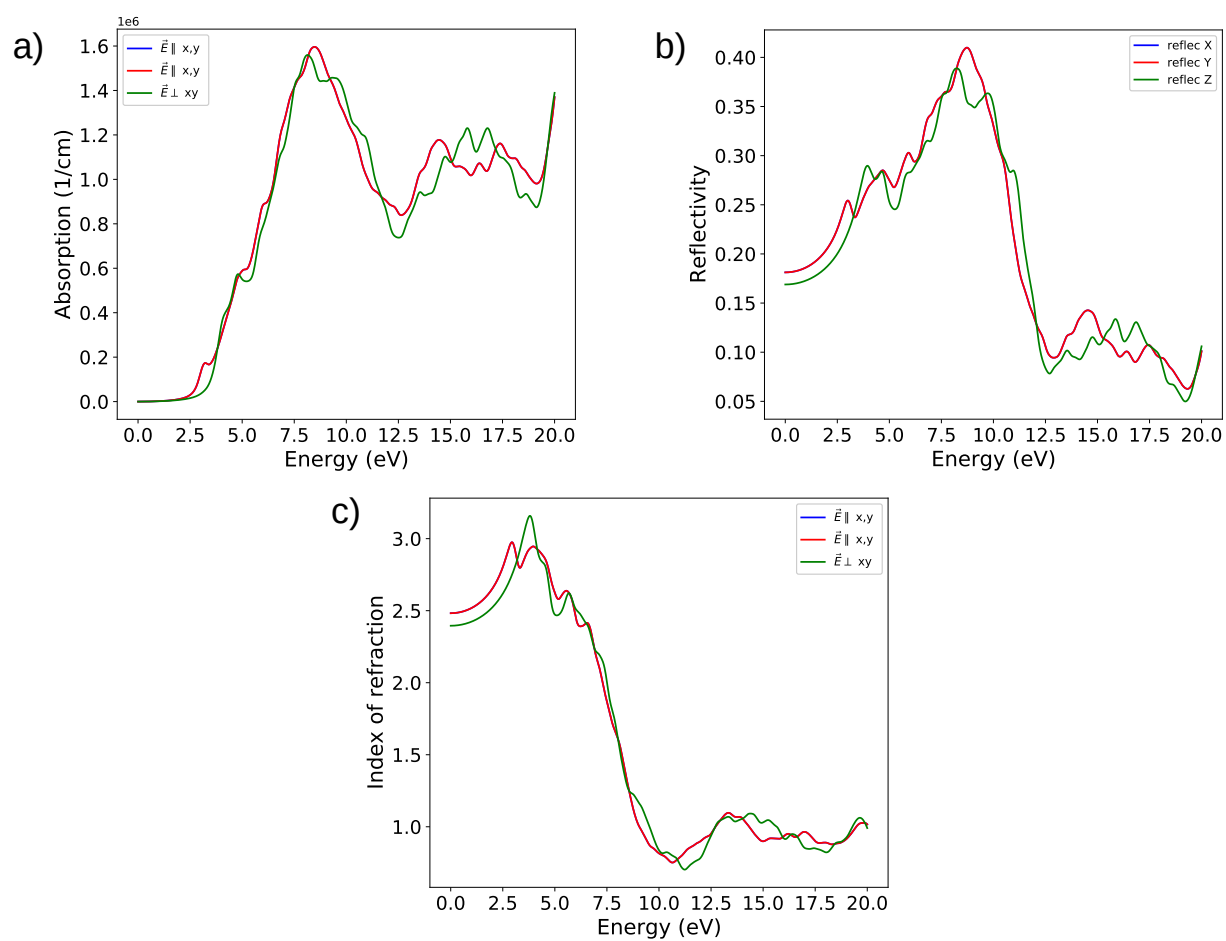
Figure C.10 - Absorption, a), reflectivity, b), and index of refraction spectra for PbMoO$_4$.
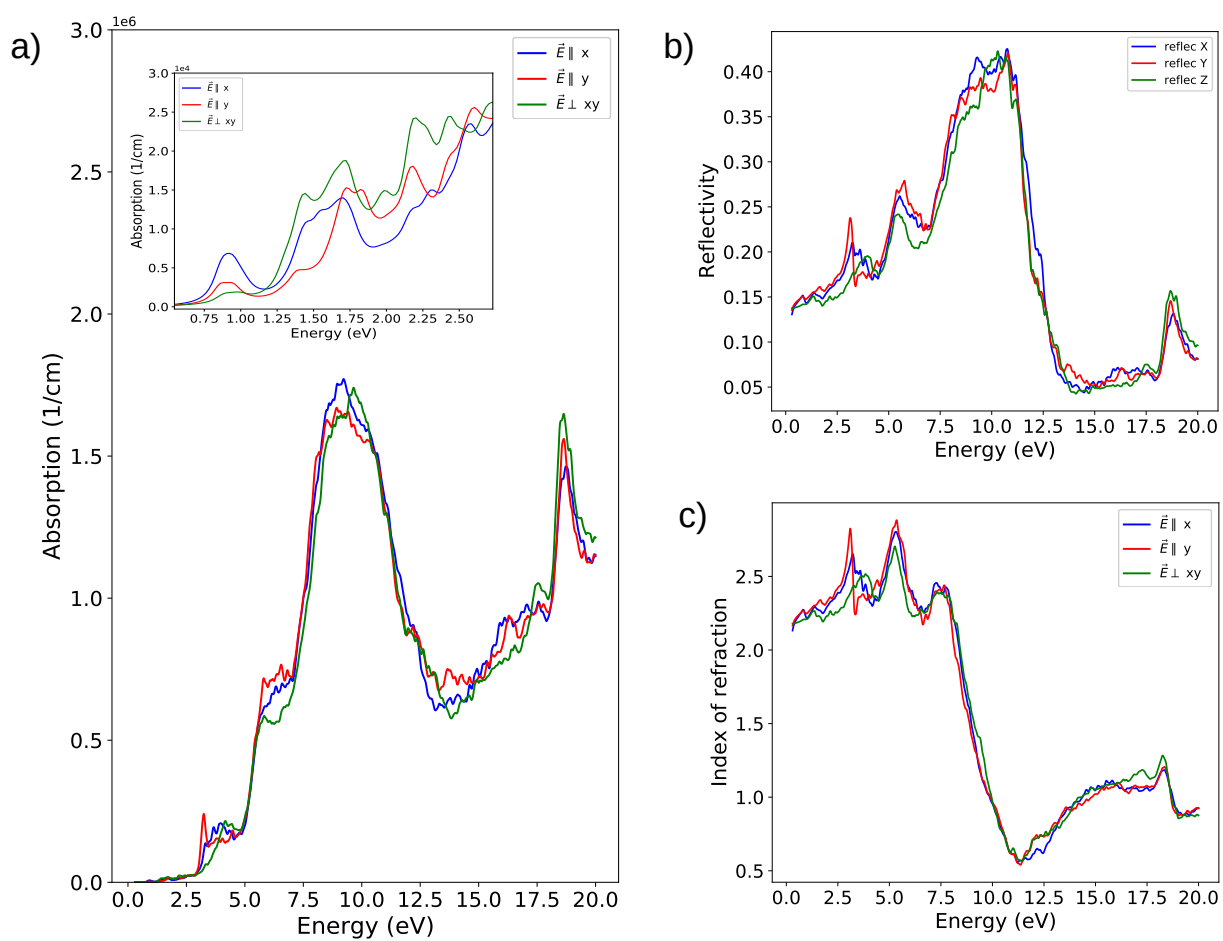
Figure C.11 - Absorption, a), reflectivity, b), and index of refraction spectra for PbMoO$_4$-$V_0^{\times}$.

ELASTIC PROPERTIES APPENDIX
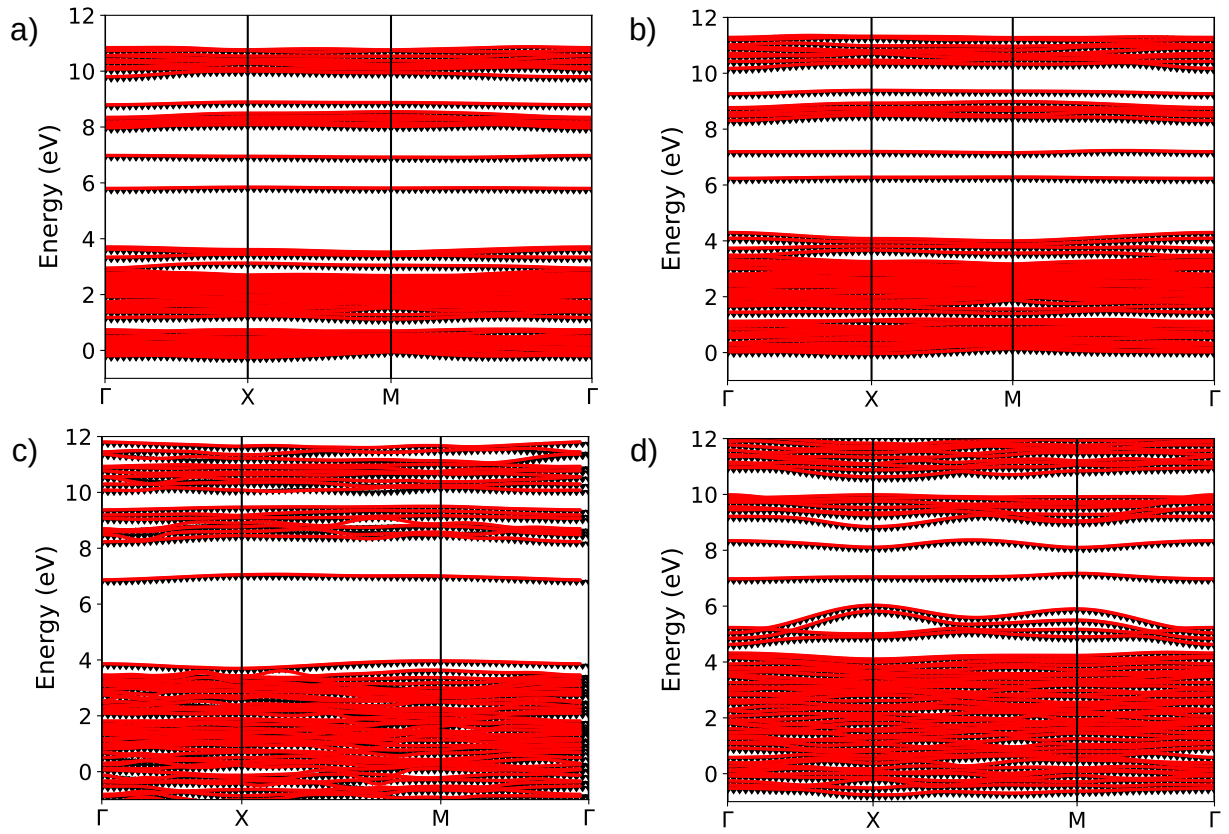
Figure D.1 - Comparison of the band spectrum obtained via Quantum-Espresso (solid lines) and obtained via wannierisation (red marker), for $BaMoO_4$-$V_0^\times$, a), $SrMoO_4$-$V_0^\times$, b), $CaMoO_4$-$V_0^\times$, c), and $PbMoO_4$-$V_0^\times$, d).
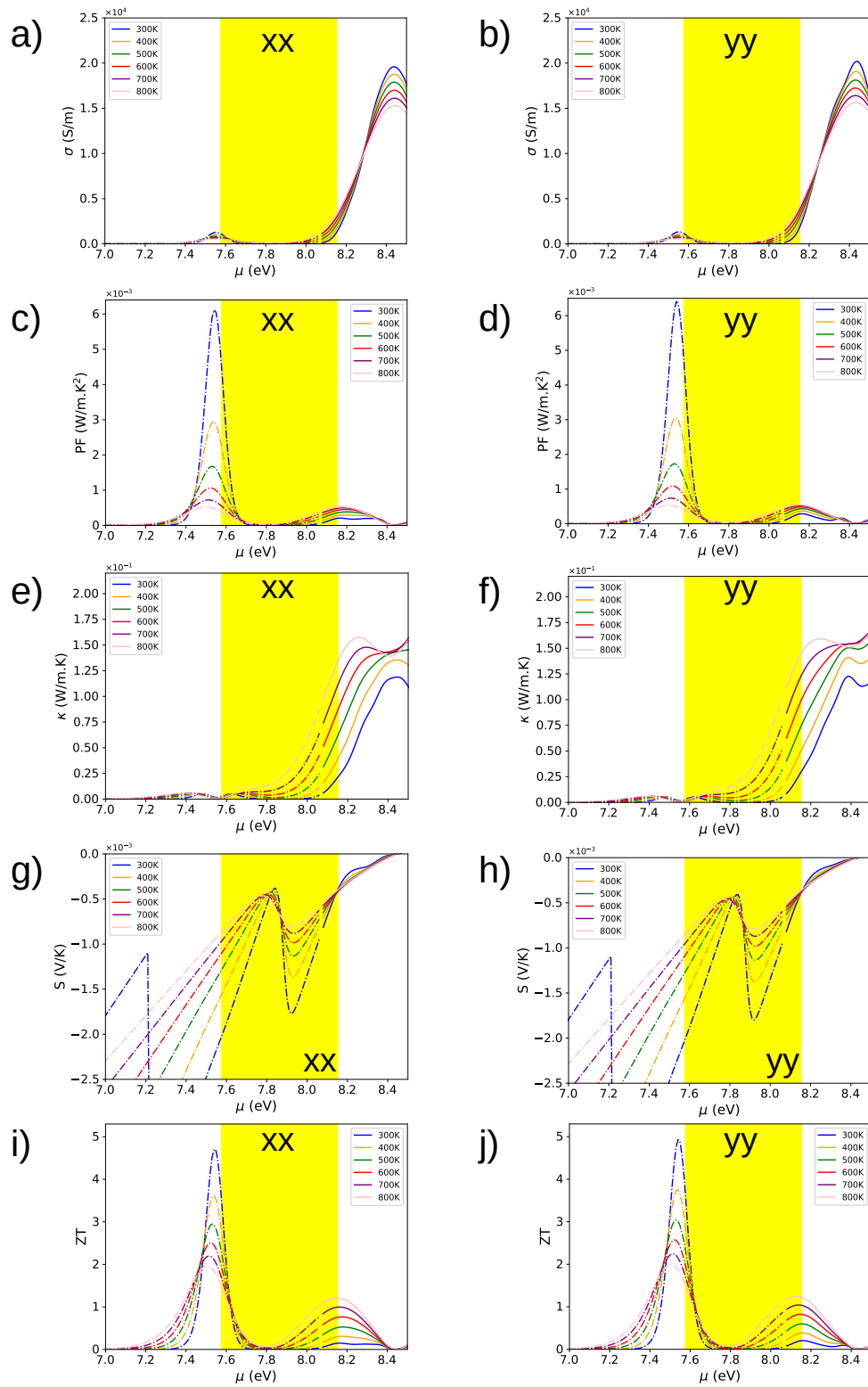
Figure D.2 - Thermoelectric properties for BaMoO$_4$-$V_0^\times$ in [xx] and [yy] tensor component as function of chemical potential (*mu*). Solid lines represents the n-type carrier, and dashed lines, the p-type carrier.
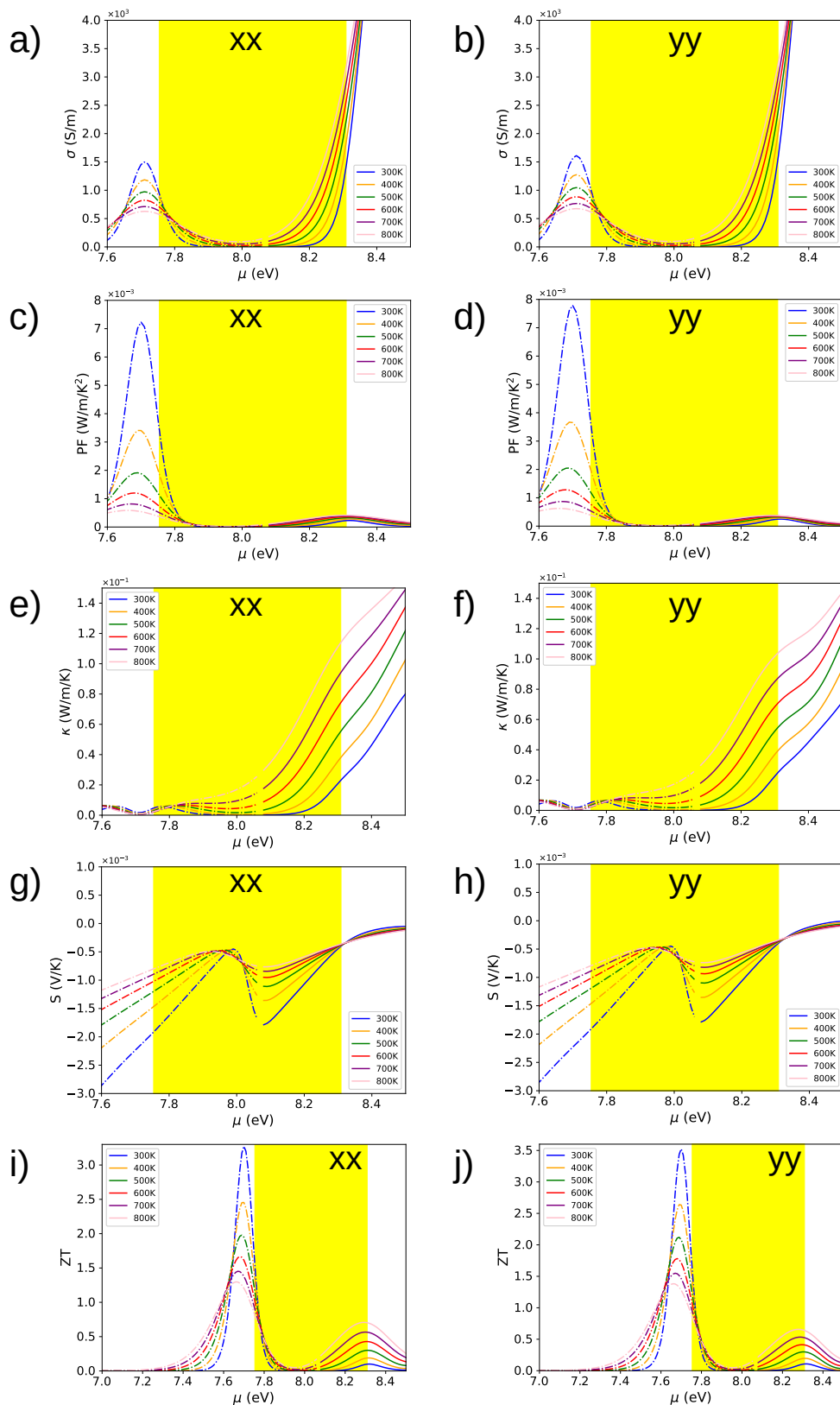
Figure D.3 - Thermoelectric properties for SrMoO$_4$-$V_0^\times$ in [xx] and [yy] tensor component as function of chemical potential (*mu*). Solid lines represents the n-type carrier, and dashed lines, the p-type carrier.
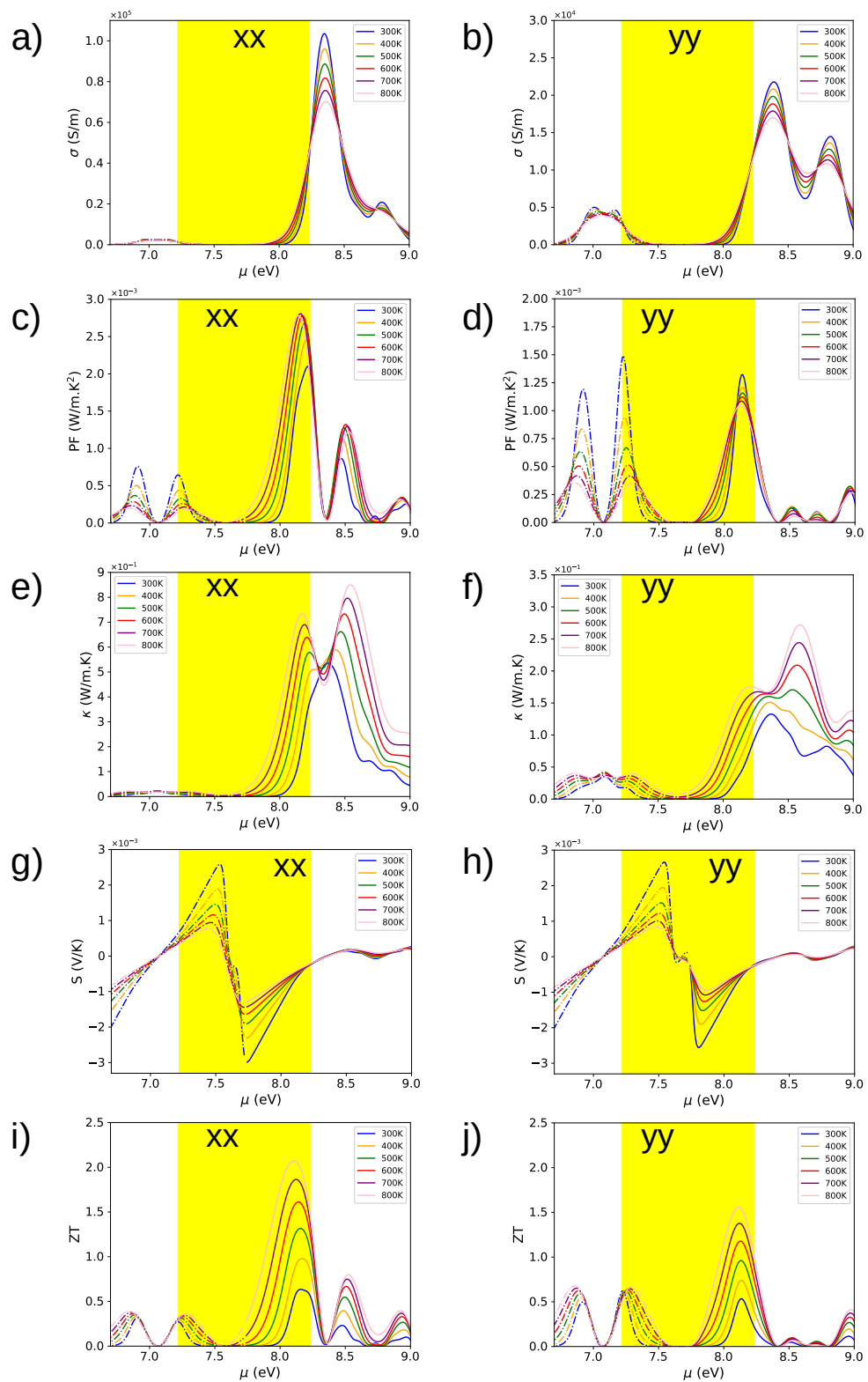
Figure D.4 - Thermoelectric properties for CaMoO$_4$-$V_0^\times$ in [xx] and [yy] tensor component as function of chemical potential (*mu*). Solid lines represents the n-type carrier, and dashed lines, the p-type carrier.
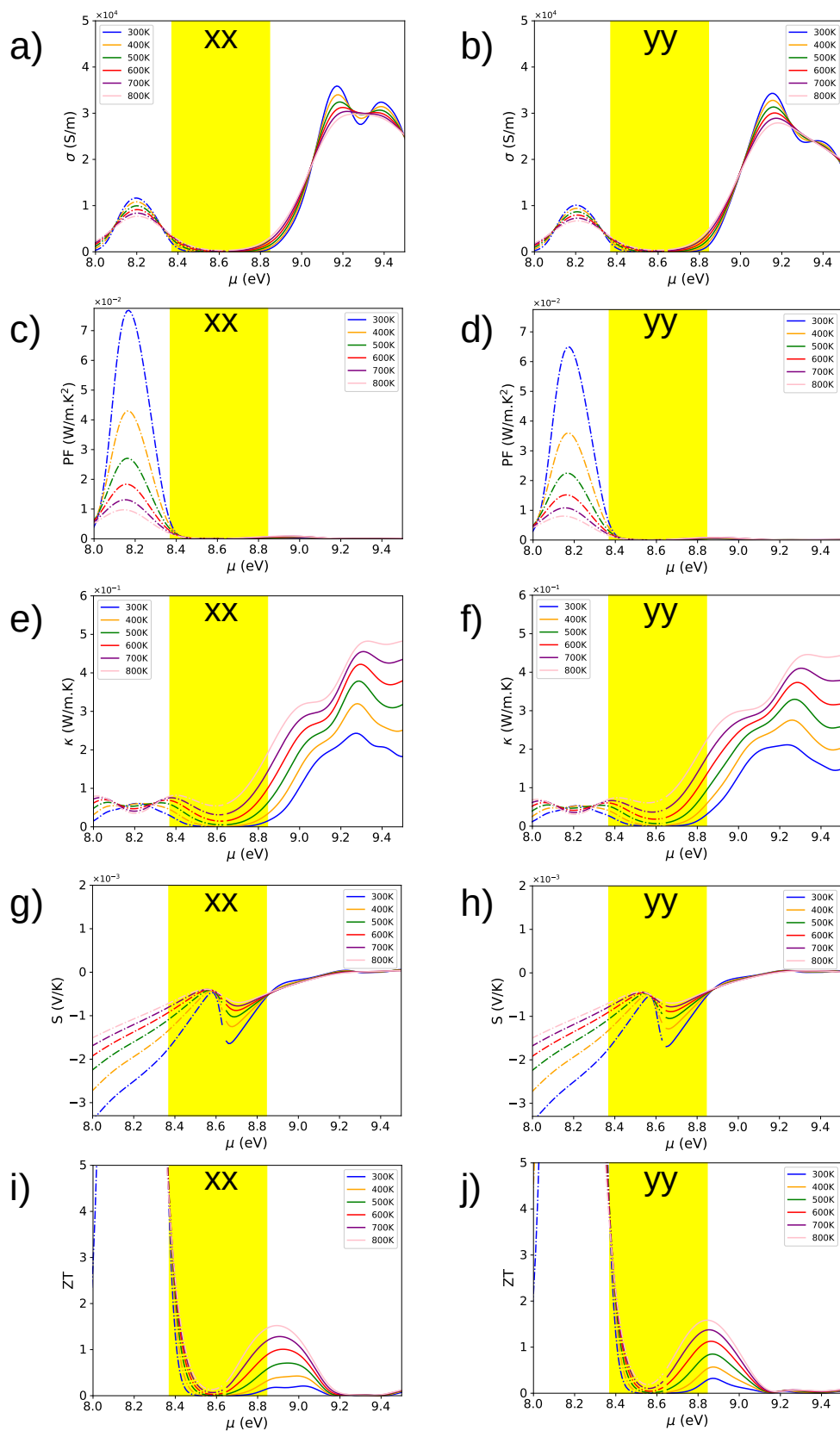
Figure D.5 - Thermoelectric properties for PbMoO$_4$-$V_0^{\times}$ in [xx] and [yy] tensor component as function of chemical potential (*mu*). Solid lines represents the n-type carrier, and dashed lines, the p-type carrier.
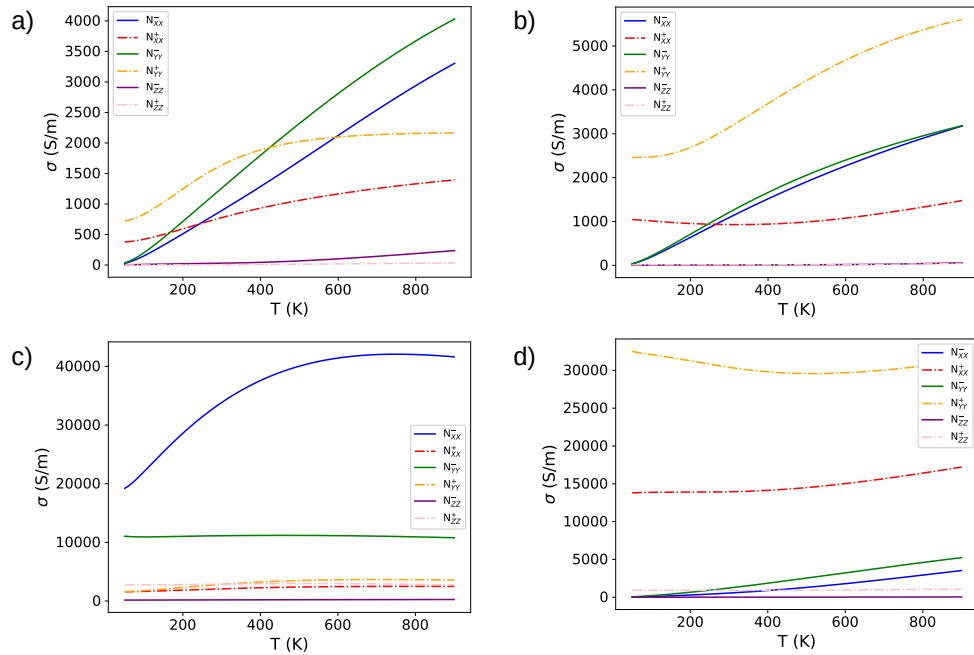
Figure D.6 - The temperature dependence of electrical conductivity in [xx] and [yy] tensor component for BaMoO$_4$-$V_0^\times$, a), SrMoO$_4$-$V_0^\times$, b), CaMoO$_4$-$V_0^\times$, c), and PbMoO$_4$-$V_0^\times$, d). For each material, the chemical potentials used were given in Table 6.5. N^- represents the n-type carrier, and N^+, the p-type carrier.
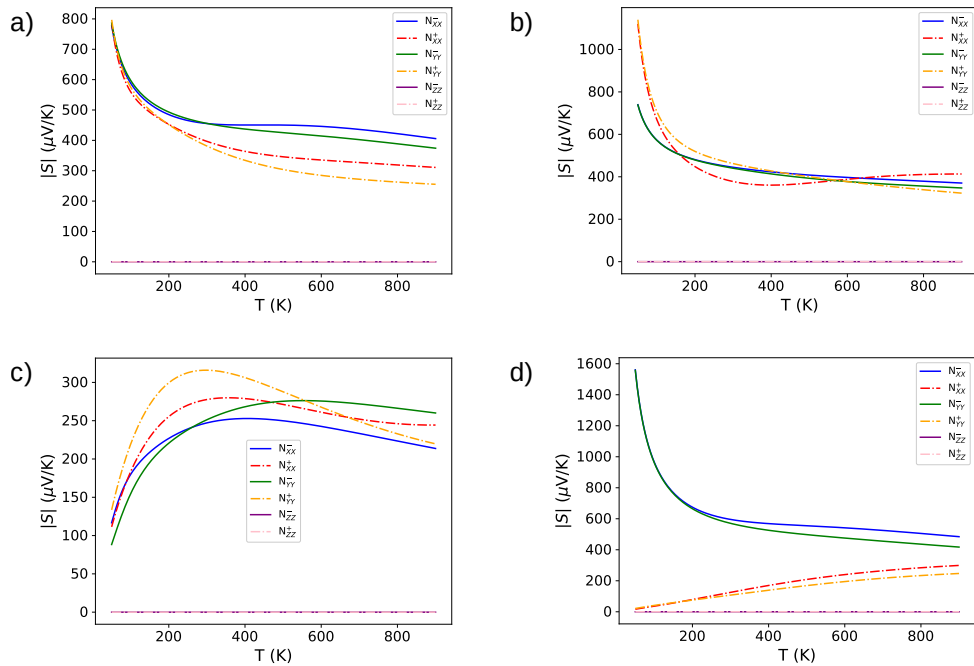
Figure D.7 - The temperature dependence of absolute Seebeck coefficient in [xx] and [yy] tensor component for BaMoO$_4$-$V_0^\times$, a), SrMoO$_4$-$V_0^\times$, b), CaMoO$_4$-$V_0^\times$, c), and PbMoO$_4$-$V_0^\times$, d). For each material, the chemical potentials used were given in Table 6.5. N^- represents the n-type carrier, and N^+, the p-type carrier..
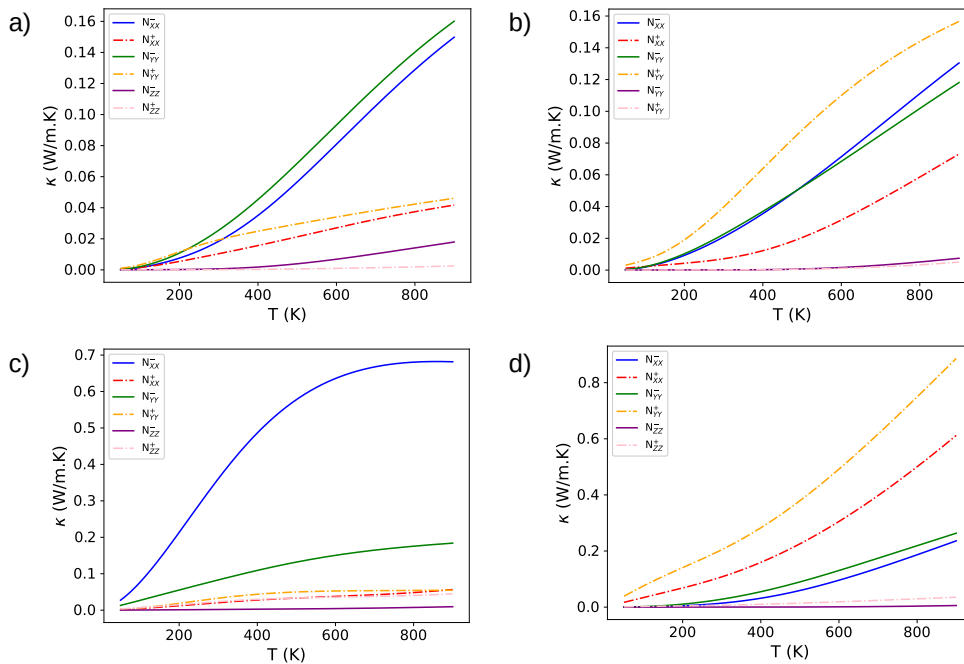
Figure D.8 - The temperature dependence of electrical thermal conductivity in [xx] and [yy] tensor component for $BaMoO_4$-$V_0^\times$, a), $SrMoO_4$-$V_0^\times$, b), $CaMoO_4$-$V_0^\times$, c), and $PbMoO_4$-$V_0^\times$, d). For each material, the chemical potentials used were given in Table 6.5. N^- represents the n-type carrier, and N^+, the p-type carrier.
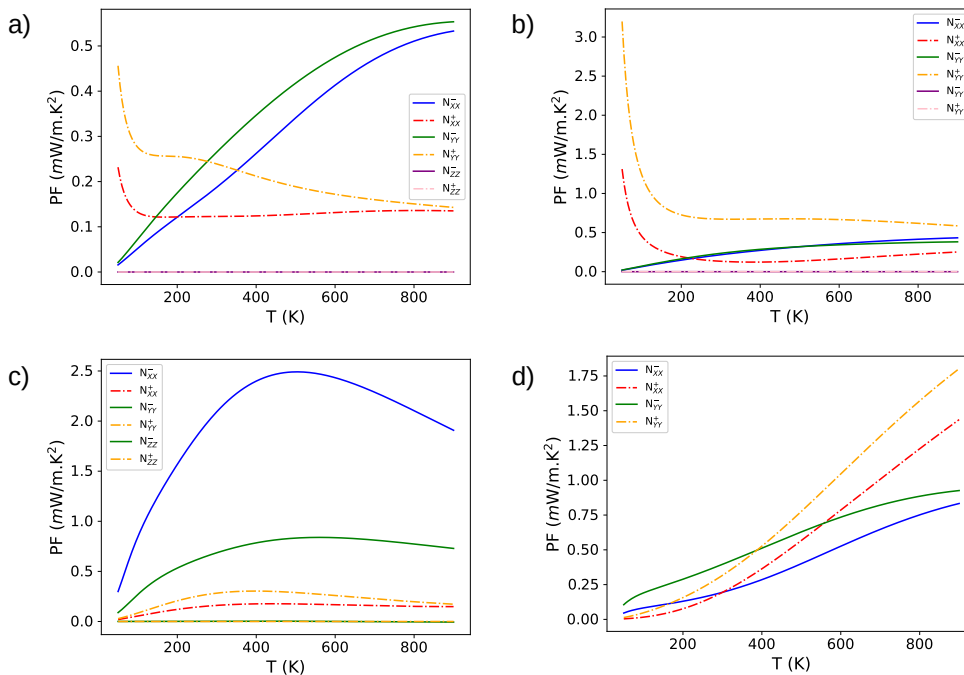
Figure D.9 - The temperature dependence of power factor (PF) in [xx] and [yy] tensor component for $BaMoO_4$-$V_0^\times$, a), $SrMoO_4$-$V_0^\times$, b), $CaMoO_4$-$V_0^\times$, c), and $PbMoO_4$-$V_0^\times$, d). For each material, the chemical potentials used were given in Table 6.5. N^- represents the n-type carrier, and N^+, the p-type carrier.
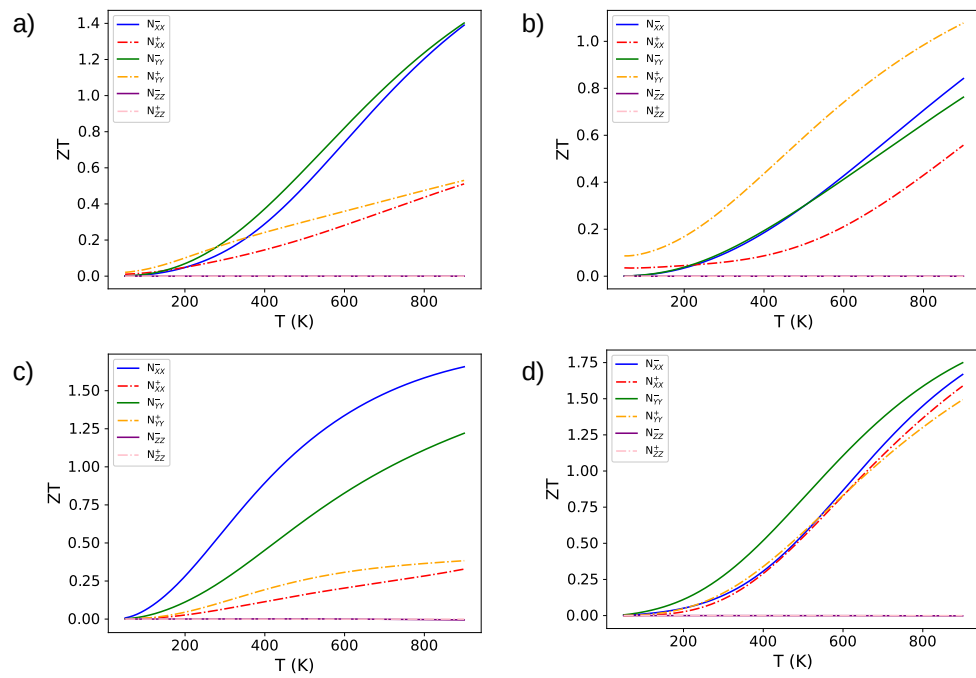
Figure D.10 - The temperature dependence of figure of merit (ZT) in [xx] and [yy] tensor component for BaMoO$_4$-$V_0^{\times}$, a), SrMoO$_4$-$V_0^{\times}$, b), CaMoO$_4$-$V_0^{\times}$, c), and PbMoO$_4$-$V_0^{\times}$, d). For each material, the chemical potentials used were given in Table 6.5. N^- represents the n-type carrier, and N^+, the p-type carrier.

NORM-CONSERVING PSEUDOPOTENTIAL COMPARISON

E.1   SrMoO4 norm-conserving

In this subsection, we will see the results of $SrMoO_4$ pristine when a pseudopotential of norm-converving type is used to perform the scf calculation. Changing a pseudopotential may lead to different results. Therefore, it is adequate to compare both pseudopotentials. The usage of norm-conserving is required in epsilon.x program.

In Fig. E.1, we see the band spectrum of SrMoOr with a direct gap of 3.71 eV (highlighted in yellow) at Γ in k-path $\Gamma - X - M - \Gamma$.
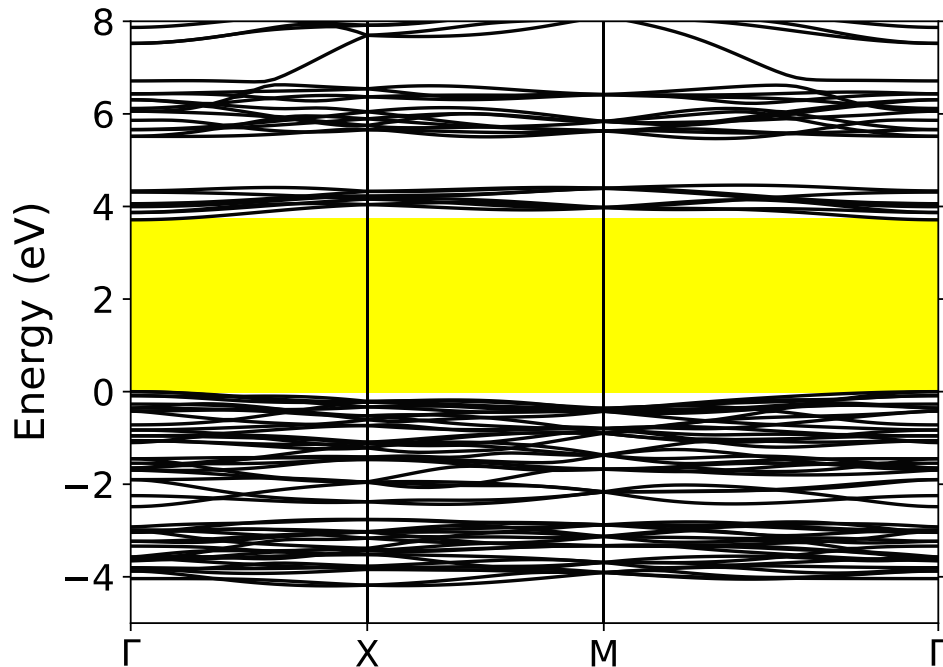
Figure E.1 - $SrMoO_4$ bands obtained by usage of normpseudopotential.

The next graph used to compare the pseudopotential is the projected density of states (PDOS), seen in Fig. E.2.
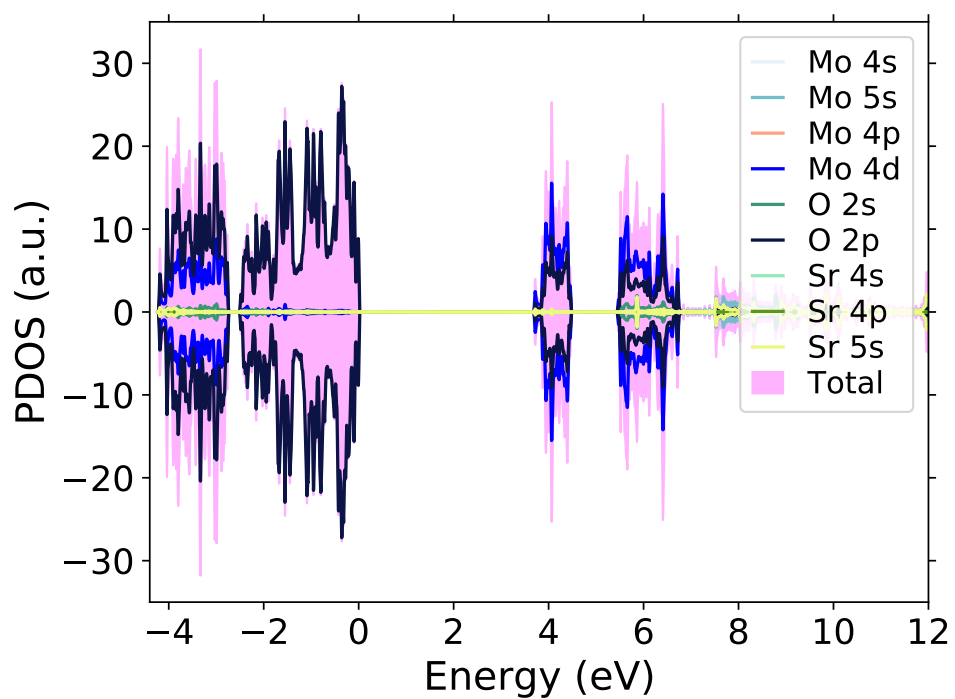
Figure E.2 - SrMoO$_4$ pdos obtained by usage of norm pseudopotential.